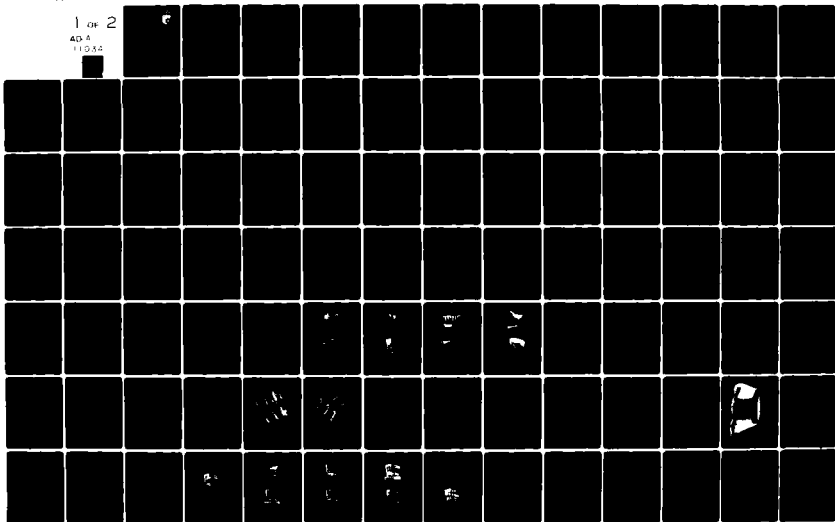


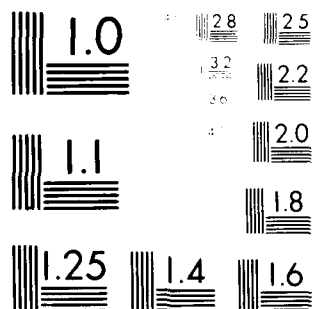
AD-A110 341

UNITED TECHNOLOGIES RESEARCH CENTER EAST HARTFORD CT F/6 20/4
RESEARCH ON TURBINE ROTOR-STATOR AERODYNAMIC INTERACTION AND RO--ETC(U)
NOV 81 R P DRING, H D JOSLYN, L W HARDIN F33615-80-C-2008
UNCLASSIFIED UTRC/R81-915048 AFWAL-TR-81-2114 NL

1 OF 2

AD-A
110341





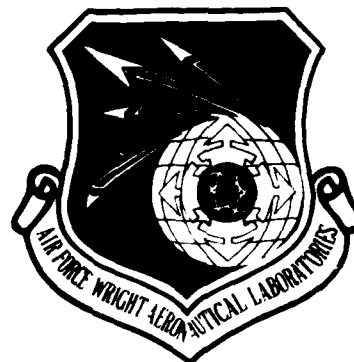
MICROCOPY RESOLUTION TEST CHART
NATIONAL BUREAU OF STANDARDS-1963-A

AD A110341

LEVEL II

10

AFWAL-TR-81-2114



RESEARCH ON TURBINE ROTOR-STATOR
AERODYNAMIC INTERACTION AND
ROTOR NEGATIVE INCIDENCE STALL

United Technologies Research Center
Silver Lane
East Hartford, CT 06108

November 1981
Final Technical Report for period March 1979-November 1981

Approved for public release; distribution unlimited

AERO PROPULSION LABORATORY
AIR FORCE WRIGHT AERONAUTICAL LABORATORIES
AIR FORCE SYSTEMS COMMAND
WRIGHT-PATTERSON AIR FORCE BASE, OHIO 45433

DTIC FILE COPY

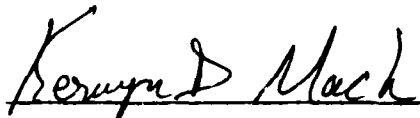
DTIC
ELECTE
S FEB 2 1982 D
D

NOTICE

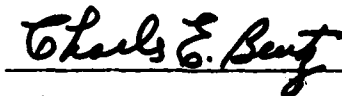
When Government drawings, specifications, or other data are used for any purpose other than in connection with a definitely related Government procurement operation, the United States Government thereby incurs no responsibility nor any obligation whatsoever; and the fact that the government may have formulated, furnished, or in any way supplied the said drawings, specifications, or other data, is not to be regarded by implication or otherwise as in any manner licensing the holder or any other person or corporation, or conveying any rights or permission to manufacture, use or sell any patented invention that may in any way be related thereto.

This report has been reviewed by the Office of Public Affairs (ASD/PA) and is releasable to the National Technical Information Service (NTIS). At NTIS, it will be available to the general public, including foreign nations.

This technical report has been reviewed and is approved for publication.

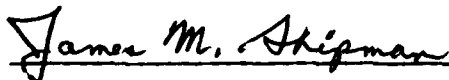


KERVYN D. MACH
Project Engineer
Turbine Engine Division
Aero Propulsion Laboratory



CHARLES E. BENTZ
Manager, Hot Section Technology Area
Turbine Engine Division
Aero Propulsion Laboratory

FOR THE COMMANDER



JAMES M. SHIPMAN, Maj, USAF
Deputy Director
Turbine Engine Division
Aero Propulsion Laboratory

"If yor address has changed, if you wish to be removed from our mailing list, or if the addressee is no longer employed by your organization, please notify AFWAL/POTC, W-PAFB, OH 45433 to help us maintain a current mailing list."

Copies of this report should not be returned unless return is required by security considerations, contractual obligations, or notice on a specific document.

UNCLASSIFIED

SECURITY CLASSIFICATION OF THIS PAGE (When Data Entered)

REPORT DOCUMENTATION PAGE		READ INSTRUCTIONS BEFORE COMPLETING FORM
1. REPORT NUMBER AFWAL-TR-81-2114	2. GOVT ACCESSION NO. AD-A110 341	3. RECIPIENT'S CATALOG NUMBER
4. TITLE (and Subtitle) RESEARCH ON TURBINE ROTOR-STATOR AERODYNAMIC INTERACTION AND ROTOR NEGATIVE INCIDENCE STALL	5. TYPE OF REPORT & PERIOD COVERED Final March 1979 - November 1981	6. PERFORMING ORG. REPORT NUMBER R81-915048
7. AUTHOR(s) R. P. Dring L. W. Hardin H. D. Joslyn J. H. Wagner	8. CONTRACT OR GRANT NUMBER(s) F33615-80-C-2008	
9. PERFORMING ORGANIZATION NAME AND ADDRESS United Technologies Research Center Silver Lane East Hartford, Connecticut 06108	10. PROGRAM ELEMENT, PROJECT, TASK AREA & WORK UNIT NUMBERS P.E. 62203F Project 3066, Task 06, Work Unit 42	
11. CONTROLLING OFFICE NAME AND ADDRESS Aero Propulsion Laboratory (AFWAL/POTC) Air Force Wright Aeronautical Laboratories Wright-Patterson AFB, OH 45433	12. REPORT DATE November 1981	13. NUMBER OF PAGES 107
14. MONITORING AGENCY NAME & ADDRESS (if different from Controlling Office)	15. SECURITY CLASS. (of this report)	
	15a. DECLASSIFICATION, DOWNGRADING SCHEDULE	
16. DISTRIBUTION STATEMENT (of this Report) Approval for public release; distribution unlimited		
17. DISTRIBUTION STATEMENT (of the abstract entered in Block 20, if different from Report)		
18. SUPPLEMENTARY NOTES		
19. KEY WORDS (Continue on reverse side if necessary and identify by block number) Turbine Aerodynamics Turbine Heat Transfer Unsteady Flow		
20. ABSTRACT (Continue on reverse side if necessary and identify by block number) The aerodynamic interaction between the rotors and stators of a large scale axial turbine stage have been studied experimentally. The data included measurements of the time averaged and instantaneous surface pressures and surface thin film gage output on both the rotor and stator at midspan. The data also included measurement of the stator suction and pressure surface time averaged heat transfer at midspan. The data was acquired with rotor-		

(Continued)

DD FORM 1 JAN 73 1473

EDITION OF 1 NOV 65 IS OBSOLETE
S/N 0102-LF-014-6601

UNCLASSIFIED

SECURITY CLASSIFICATION OF THIS PAGE (When Data Entered)

UNCLASSIFIED

SECURITY CLASSIFICATION OF THIS PAGE (When Data Entered)

Abstract (Cont'd)

stator axial gaps of 15% and 65% of axial chord. The upstream potential flow influence of the rotor on the stator was seen as well as the downstream potential flow and wake influences of the stator on the rotor. It was also seen that at the 15% axial gap, the stator heat transfer coefficient was typically 25% higher than that at the 65% gap.

The second phase of the program was an investigation of the nature of the full-span steady flow over the rotor with incidence varying up to negative incidence stall. Fullspan pressure distributions and surface flow visualization were acquired over the entire range of incidence. The data indicated separation-free flow and large radial flows on the pressure surface in the vicinity of design incidence. It was demonstrated that the radial flow on the pressure surface was due to the relative eddy. At large negative incidence, pressure surface stall occurred which penetrated to 60% chord at midspan. These separated flows were analyzed by applying potential flow theory to simulate the measured pressure distributions.

S/N 0102-LF-014-6601

UNCLASSIFIED

SECURITY CLASSIFICATION OF THIS PAGE (When Data Entered)

PREFACE

This report describes a contractual effort performed by the United Technologies Research Center for the Components Branch (POTC) of the Turbine Engine Division (POT), Aero Propulsion Laboratory, Wright Aeronautical Laboratories, Wright-Patterson Air Force Base, Ohio, under Project 3066, Task 06 Work Unit 42.

The work reported herein was performed during the period 7 March 1980 to 7 November 1981 under the direction of Dr. Kervyn Mach (APL/POTC), project engineer, Contract Number F33615-80-2008. The principal investigator was Dr. Robert P. Dring of the United Technologies Research Center.

The authors are indebted to many people for the successful completion of the program and in particular to Dr. Joseph R. Caspar for his inclusion of mass addition in the blade-to-blade potential flow analysis, to Mr. John Kostic for helping in the rig assembly, to Mr. Kenneth Dauphinais for writing the data reduction software and for doing the data reduction, to Mr. Charles Coffin for building the heat transfer models.

Accession For		
NTIS GRA&I	<input checked="" type="checkbox"/>	
DTIC TAB	<input type="checkbox"/>	
Unannounced	<input type="checkbox"/>	
Justification		
By _____		
Distribution/		
Availability Codes		
Dist	Avail and/or	
A	Special	



DTIC
ELECTE
FEB 2 1982
S D

TABLE OF CONTENTS

Section	Page
I. INTRODUCTION	1
II. EXPERIMENTAL FACILITY	5
III. DISCUSSION	6
A. Rotor-Stator Aerodynamic Interaction	6
1. Steady-State and High Response Instrumentation	6
2. Results	8
(a) Steady-State Pressure	8
(b) Unsteady Pressure Envelopes	10
(c) Unsteady Pressure Wave Amplitude and Phase	11
(d) Instantaneous Pressure Distributions	14
(e) Unsteady Trailing Edge Loading.	15
(f) Decay of Unsteadiness with Axial Gap	17
(g) Thin Film Gage Results - Stator	18
(h) Thin Film Gage Results - Rotor	20
B. Unsteady Effects on Stator Heat Transfer	22
1. Stator Heat Transfer Model and Instrumentation	22
2. Results.	23
C. Rotor Fullspan Aerodynamics	25
1. Flow Visualization Technique	26
2. Results.	26
3. Radial Flow Analysis	29
4. Potential Flow Modeling of Separation Bubbles	35
IV. CONCLUSIONS	37
REFERENCES	40
APPENDIX STATOR WAKE CHARACTERIZATION	44

LIST OF ILLUSTRATIONS

<u>Figure</u>	<u>Page</u>
1. Turbine Stage at 15% Gap (Kulite Sites)	46
2. Stator Kulite Instrumentation	47
3. Rotor Kulite Instrumentation	48
4. Stator Thin Film Gage Instrumentation	49
5. Rotor Thin Film Gage Instrumentation	50
6. Stator Pressure Distribution - Time Average	51
7. Rotor Pressure Distributions - Time Average	52
8. Stator Unsteady Pressure Envelope, 15% Gap, $(C_x/U) = 0.78$	53
9. Rotor Unsteady Pressure Envelope, 15% Gap, $(C_x/U) = 0.78$	54
10. Stator Unsteady Pressure, 15% Gap	55
11. Rotor Unsteady Pressure, 15% Gap	56
12. Rotor Unsteady Pressure, 65% Gap	57
13. Stator Instantaneous Pressure Distributions, 15% Gap, $(C_x/U) = 0.78$	58
14. Rotor Instantaneous Pressure Distributions, 15% Gap, $(C_x/U) = 0.78$	59
15. Stator Pressure Time History, 15% Gap, $(C_x/U) = 0.78$	60
16. Rotor Pressure Time History, 15% Gap, $(C_x/U) = 0.78$	61
17. Stator Trailing Edge Unsteady Pressure, 15% Gap, $(C_x/U) = 0.78$	62
18. Decay of Unsteady Pressure Amplitude with Axial Gap	63

LIST OF ILLUSTRATIONS (Cont'd)

<u>Figure</u>	<u>Page</u>
19. Stator Thin Film Data, 15% Gap, $(C_x/U) = 0.78$	64
20. Rotor Thin Film Data, 15% Gap	65
21. Rotor Thin Film Data, 65% Gap	66
22. Rotor Pressure and Thin Film Data at Site 7, $(C_x/U) = 0.78$	67
23. Stator Pressure Surface Heat Transfer Model	68
24. Stator Velocity and Stanton Number Distributions, $(C_x/U) = 0.78$	69
25. Stator Stanton Number Distributions, $(C_x/U) = 0.96$ and 0.68	70
26. Rotor Geometry	71
27. Rotor Midspan Inlet Flow Angle and Relative Total Pressure Coefficient Variation with (C_x/U)	72
28. Rotor Pressure Surface Flow Visualization, $(C_x/U) = 0.96$, $\beta_1 = 35^\circ$	73
29. Rotor Pressure and Suction Surface Flow Visualization, $(C_x/U) = 0.78$, $\beta_1 = 40^\circ$	74
30. Rotor Pressure Surface Flow Visualization, $(C_x/U) = 0.68$, $\beta_1 = 45^\circ$	75
31. Rotor Pressure Surface Flow Visualization, $(C_x/U) = 0.56$, $\beta_1 = 55^\circ$	75
32. Rotor Pressure Surface Flow Visualization, $(C_x/U) = 0.50$, $\beta_1 = 65^\circ$	76
33. Rotor Pressure Surface Flow Visualization, $(C_x/U) = 0.45$, $\beta_1 = 75^\circ$	76
34. Rotor Pressure and Suction Surface Flow Visualization, $(C_x/U) = 0.42$, $\beta_1 = 85^\circ$	77

LIST OF ILLUSTRATIONS (Cont'd)

<u>Figure</u>	<u>Page</u>
35. Rotor Spanwise Variation of Relative Total Pressure	78
36. Rotor Spanwise Variation of Relative Inlet Flow Angle	79
37. Rotor Midspan Pressure Distributions, $\beta_1 = 35^\circ$ to 85°	80
38. Rotor Fullspan Pressure Distributions, $(C_x/U) = 0.96$	81
39. Rotor Fullspan Pressure Distributions, $(C_x/U) = 0.78$	82
40. Rotor Fullspan Pressure Distributions, $(C_x/U) = 0.68$	83
41. Rotor Fullspan Pressure Distributions, $(C_x/U) = 0.56$	84
42. Rotor Fullspan Pressure Distributions, $(C_x/U) = 0.50$	85
43. Rotor Fullspan Pressure Distributions, $(C_x/U) = 0.45$	86
44. Rotor Fullspan Pressure Distributions, $(C_x/U) = 0.42$	87
45. Rotor Midspan Contour	88
46. Gapwise Variations of Velocity Components and Pitch Angle	89
47. Variation of Pressure and Suction Surface Pitch Angles with Relative Inlet Flow Angle	90
48. Potential Flow Simulation of Separated flow Using a Hypothetical Contour - Separation Bubble at $\beta_1 = 85^\circ$	91
49. Potential Flow Simulation of Separated Flow Using a Hypothetical Contour - Pressure Distribution at $\beta_1 = 85^\circ$	92
50. Potential Flow Simulation of Separated Flow Using Surface Blowing - Pressure and Normal Velocity Distributions at $\beta_1 = 85^\circ$	93
51. Potential Flow Simulation of Separated Flow Using Surface Blowing - Separation Bubble at $\beta_1 = 85^\circ$	94

LIST OF SYMBOLS

Symbols

B	Airfoil chord
B_x	Airfoil axial chord
C	Absolute flow speed
C_p	Specific heat
C_p	Pressure coefficient: $(P_{T1} - P)/Q_2$
\bar{C}_p	Steady state pressure coefficient: $(P_{T1} - \bar{P})/Q_2$
\hat{C}_p	Amplitude pressure coefficient: $(P_{\max} - P_{\min})/Q_2$
C_p'	Fluctuation pressure coefficient: $(P(t) - \bar{P})/Q_2$
$C_{p,U}$	Pressure coefficient: $(P_{To} - P)/1/2\rho U_m^2$
d	Airfoil trailing edge diameter
h	Stream tube height
H	Heat transfer coefficient
H_T	Total enthalpy
k	Reduced frequency: $(N\Omega B/2C)$
K_1	Defined in Eq. 7
K_2	Defined in Eq. 9
N	Number of airfoils in a row
P	Static pressure
P_T	Total pressure: $(P + 1/2\rho C^2)$
$P_{T,rel}$	Relative total pressure: $(P + 1/2\rho W^2)$

LIST OF SYMBOLS (Cont'd)

Symbols

$P_{T,rot}$	Rotary total pressure: $(P + 1/2\rho(W^2 - U^2))$
Q	Dynamic pressure
r	Radius
R_n	Geodesic curvature of a streamline
s	Streamwise distance
S	Surface arc length
St	Stanton number: $(H\rho C_p/C_l)$
St	Strouhal number
t	Airfoil thickness
t	Normalized time: $(T - T_o)/\text{Airfoil passing period}$
T	Time
T_o	Reference time
T_T	Total temperature
U	Wheel speed
W	Relative flow speed
x	Axial distance
y	Tangential distance
Y	Total pressure loss: $(\Delta P_T/Q)$
α	Absolute flow angle
β	Relative flow angle

LIST OF SYMBOLS (Cont'd)

Symbols

γ	Specific heat ratio
δ_w	Stator wake half width at mid-depth
δ^*	Displacement thickness
ρ	Density
τ	Airfoil pitch
ζ	Relative vorticity
ω	Absolute vorticity
Ω	Rotor angular rotation (radians per second)
θ	Tangential angle
Θ	Momentum thickness

LIST OF SUBSCRIPTS

Subscripts

0	Stator inlet
1	Stator exit and rotor inlet (general inlet)
2	Rotor exit (general exit)
x	Axial
r	Radial
θ	Tangential
abs	Absolute
rel	Relative
m	Midspan
R	Rotor
S	Stator
p	Pressure surface
s	Suction surface
s	Streamwise

SECTION I

INTRODUCTION

Turbine airfoil design is presently at the point where accurate design analyses are available for the compressible potential (inviscid) flow through cascades and for the boundary layer flows on airfoil surfaces. The designer can, through subtle changes in the airfoil contour, carefully optimize both the inviscid and viscous character of the flow. This optimization includes not only the aerodynamic performance but also the thermal performance, i.e. the cooling design. The vast majority of these analyses, however, are based on the assumption that the rotor and stator rows are spaced far enough apart such that the flow in each is steady, i.e. that there is no unsteadiness of any sort due to rotor-stator aerodynamic interaction. It is clear, however, that when rows are closely spaced there can be a strong interaction which will impact the aerodynamic, thermal, and structural performance of the airfoils. Furthermore, the rows of current turbines (and compressors) are already very closely spaced. Axial gaps between adjacent rows of approximately $1/4$ to $1/2$ of the airfoil chord are common practice. Thus, the problem of rotor-stator interaction is having an impact on existing turbine designs. Future designs with higher loading and lower aspect ratios, i.e. fewer and bigger airfoils, and the ever present desire to minimize engine length, will aggravate this condition even further. The reason for this problem is that currently there are no practical analytical tools or detailed experimental results that can provide guidance to the designer as to the magnitude or impact of this unsteadiness.

The phenomenology of rotor-stator aerodynamic interaction may be divided into two separate areas: potential flow (inviscid) interaction and wake (viscous) interaction. The gradients due to the potential flow over an airfoil extend both upstream and downstream of the airfoil and typically these gradients decay with a length scale equal to the pitch (or chord) of the cascade. The potential flow over a row of airfoils can cause unsteadiness in both the upstream and downstream rows if the axial gap between them is less than approximately the airfoil chord. The wake, on the other hand, is convected downstream. The far field rate of decay of the wake, however, is much more gradual than that of the potential flow. It may still be felt several chords downstream. Thus, wake interaction will be present even when adjacent rows are spaced far apart. Under most circumstances, both mechanisms occur simultaneously. Both mechanisms have been investigated to some degree over the past twenty-five years and are discussed in the literature.

One of the earliest studies of the interaction problem was conducted by Kemp and Sears (Refs. 1 and 2). After applying a number of "classical" simplifying assumptions, that is, a linearized potential flow solution for thin airfoils with small turning, they came to the conclusion that for realistically close

axial spacing of two rows of airfoils the unsteady lift amplitude could be as much as 18 percent of the steady value. Furthermore, the unsteadiness of the flow over the upstream row was much larger than that of the downstream row. They also found that "the unsteady forces arising from passage (of an airfoil) through viscous wakes are of about the same size" as those due to the potential flow interaction. Giesing (Refs. 3 and 4) carried out an "exact" solution of unsteady potential flow, and in particular, for the case of the interaction of two moving lifting bodies. Although there were no quantitative results of direct value to the present problem, the qualitative results were impressive as to the complexity of the problem and the flows that were produced.

In a series of combined analytical and experimental studies, Parker et al. (Refs. 5 through 8) provided a number of significant insights into the nature of rotor-stator interaction. They carried out a solution for the quasi-steady potential flow interaction of two rows of airfoils accounting for their relative motion. They concluded that the principal mechanism of potential flow interaction was the prevention of the accelerations normal to the surface of the closely coupled airfoils which would have occurred at those locations if the rows were not closely spaced. In addition, the unsteady pressure differences they computed on the surface of one of the airfoils of two interacting rows was roughly three times the computed pressure fluctuation amplitude at the same point without interaction, i.e., with only the moving row present. From these results, Parker raised the question of cyclic separation resulting from periodic locally strong negative pressure gradients. This would have strong implications for both the aerodynamic and thermal (heat transfer) performance of an airfoil. Although these solutions did not account for unsteady shed vorticity, they did show better agreement with measured data trends with the assumption of constant airfoil circulation than for the assumption of a fixed Kutta point.

This question of an appropriate Kutta condition for unsteady flow at intermediate values of the frequency parameter (k) was the subject of papers by Gostelow (Ref. 9) and by Satyanarayana and Davis (Ref. 10). For steady flow and in fact even in unsteady flow at low values of the frequency parameter ($k < 0.6$) the classical Kutta condition, i.e. no trailing edge loading, appeared to be reasonably accurate. However, "For problems involving rotor-stator interaction, usually at frequency parameters higher by an order of magnitude or more, the probability of instantaneous trailing edge loading is strong" (Ref. 9). Such trailing edge loading was subsequently demonstrated experimentally (Ref. 10). The importance of this question and its centrality to any analytical attack on the rotor-stator interaction problem was evident from the discussion following the presentation of the papers at the AGARD conference on unsteady phenomena in turbomachinery, Ref. 11.

Adachi and Murakami (Ref. 12) studied the passage of a wake from a moving circular cylinder as it was convected through a row of compressor stator airfoils. The instantaneous stator pressure distribution was also measured and its fluctuations were related to the instantaneous wake disturbance in the blade channel.

Gallus et al. (Ref. 13), examined rotor-stator interaction in a compressor stage having an axial gap of 60 percent of the rotor axial chord. Unsteady pressures were measured at midspan at seven locations on the rotor and at ten locations on the stator. The unsteady lift coefficient calculated from this data for the stator was sensitive to flow coefficient but typically had an amplitude of ± 0.04 . The rotor data indicated only very weak potential flow interaction with the stator at this large axial spacing. Scholz (Ref. 14) reported data taken by Ohashi and by Speidel which indicated how the total pressure loss of a row of airfoils could vary as a function of the location and motion of an upstream blade row. He described how a suitably defined Strouhal number could characterize this rotor-stator wake interaction effect. The physics here were much the same as those described by Evans (Ref. 15) when he showed that the boundary layer profile on a downstream airfoil could oscillate between characteristically laminar and turbulent conditions periodically with the passing of the wake of a moving upstream blade row.

Although investigators have been examining the problem for many years, the main result is that more questions and concerns have been raised. There is still precious little in the way of analytical tools or experimental results to guide the designer. The only exception to this is that there is a great deal of overall performance data for turbines and compressors from a wide variety of sources (Refs. 16 through 22). The conclusions from reviewing all of these results are: (1) that there is an optimum axial gap between rotors and stators, (2) that the value of this optimum spacing is hard to generalize, and (3) that for changes in axial spacing over the ranges commonly found in current engines the change in overall turbine or compressor efficiency can be as much as 2 percent. From this alone the need for a basic understanding of the impact and mechanisms of rotor-stator aerodynamic interaction is abundantly clear. The present state-of-the-art is that rotor-stator axial spacing is set based typically on mechanical (no-rub) considerations with no aerodynamic criteria at all.

Studies of two other aspects of the flow through an axial turbine stage are included in this report. First, it is well documented by Blair (Ref. 23) that unsteadiness due to free-stream turbulence can significantly increase the heat transfer of a turbulent boundary layer. As Dunn and Hause (Ref. 24) have demonstrated, the unsteadiness due to a rotor aft of a turbine stator can significantly increase the stator heat transfer. This entire area of the impact of the unsteadiness due to rotor-stator axial spacing on heat transfer is of extreme importance to the designer and could ultimately be the determining feature in setting rotor-stator axial gaps. Currently, however, very little information is available to provide this guidance.

Finally, the area of negative incidence (pressure surface) stall is also of considerable concern to the designer. This is particularly true in variable cycle engines where large variations in rotor incidence may occur. It has already been demonstrated by Dring et al. (Refs. 25 and 26) that the flow on the pressure surface of a turbine rotor blade can be highly three-dimensional in nature.

The strong radial flows that have been seen to occur are a direct result of the typically very low flow velocity on the pressure surface. When negative incidence stall occurs it is likely the three-dimensionality of the flow will become even more severe. At present there is little available to guide the designer either as to the nature of the radial flow when the pressure surface boundary layer is attached, or to the nature of the flow when negative incidence stall occurs.

This report presents the results of a research program aimed at clarifying three aspects of turbine stage fluid dynamics.

1. Rotor-stator aerodynamic interaction
2. The effect of rotor-stator gap on stator heat transfer
3. The full span aerodynamics of a rotor blade from design incidence to negative incidence stall.

SECTION II

EXPERIMENTAL FACILITY

The United Technologies Research Center (UTRC) Large Scale Rotating Rig No. I (LSRR-I) is 5 feet (1.52 meters) in diameter and it can accept a wide variety of turbine and compressor models ranging in hub/tip ratio from 0.5 to 0.8. The turbine model (0.8 hub/tip ratio) has three rows of airfoils; first vane, first blade and second vane. For the present program only the first vane (stator) and the first blade (rotor) were installed (Fig. 1)*. Both airfoils had aspect ratios (span/axial chord) of approximately unity. The airfoil chords are approximately 5 times engine scale. The large scale of the rig is a distinct advantage because it permits the use of extensive instrumentation on both the stationary and rotating airfoils. The large scale also has the advantage of giving Reynolds numbers which are typical of high pressure turbines at nominal model running conditions of 410 rpm and a test section average axial flow velocity of 75 ft/sec (23 m/s). The various absolute and relative flow angles and the airfoils that produce them (Fig. 1) are also typical of current high pressure turbine stages. Airfoil geometry and nominal operating conditions are summarized in Table 1.** Unless otherwise stated, all conditions and dimensions quoted are at midspan ($r_m = 27$ in.). The major departure from actual engine aerodynamic parameters is that the flow is virtually incompressible. The airfoil exit Mach numbers are approximately 0.2. Thus, the facility is limited to the study of phenomena which are insensitive to compressibility effects. This would include the three phenomena being examined under the present program, namely: (1) rotor-stator aerodynamic interaction, (2) unsteady effects on stator heat transfer and (3) rotor fullspan aerodynamics.

For all values of (C_x/U) at which data was obtained the axial flow velocity was held constant at a nominal value of 75 ft/sec. Variation of (C_x/U) was achieved by varying the rotor speed. The motivation for this approach was to hold the airfoil Reynolds numbers (based on exit velocity) constant at all test conditions. The only exception to this was that at the largest negative incidences (very low values of C_x/U) the rotor speed was held at 700 rpm and lower values of the axial flow velocity were used. The motivation here was a vibration problem that developed at very high speeds.

A complete description of the computerized steady state data acquisition and control system and the steady state transducer calibration procedure were presented by Dring and Joslyn (Ref. 26). The specialized instrumentation used in each of the three tests of the present program are described in context throughout this report.

*Figures are located on pages 46 through 94.

**See page 45.

SECTION III

DISCUSSION

A. Rotor-Stator Aerodynamic Interaction

The turbine rotor-stator aerodynamic interaction program consisted of acquiring and analyzing high response pressure and thin film gage data at midspan on the rotor and stator airfoils at three flow conditions corresponding to the rotor design incidence ($C_x/U = 0.78$, $\beta_1 = 40^\circ$) and at $\pm 5^\circ$ of rotor incidence ($C_x/U = 0.96$, $\beta_1 = 35^\circ$ and $C_x/U = 0.68$, $\beta_1 = 45^\circ$). Data were acquired at two rotor-stator axial spacings. The closest spacing was 15 percent of the nominal (average) axial chord, as in Fig. 1, and the largest spacing was 65 percent of the nominal axial chord.

1. Steady State and High Response Instrumentation

Both the rotor and the stator had 22 pressure taps around their perimeters at midspan which were used to establish the steady state, or time averaged, pressure distributions. These rotor and stator pressure taps were each connected to 48 channel Scanivalves (Scanivalve, model 48J9-1290) mounted in the rotating and stationary frames of reference, respectively. Transducer calibration procedures for these Scanivalves were discussed in Ref. 26.

Both the rotor and the stator also had 15 miniature high response pressure transducers (Kulite, model XCS-093 \pm 2D) distributed around each airfoil at midspan (Figs. 2 and 3). The transducers were inserted into chambers which were connected to the airfoil surface by a 0.020 in. diameter hole. The geometry of the installation was such that a frequency response of approximately 10 kHz was realized. This response was 50 times blade passing frequency and hence it was judged to be adequate for the present application. The transducers and all wiring were recessed into channels machined into the airfoils' surfaces. After installation was completed, these channels were filled and the airfoils were restored to their original contours.

As can be seen in Figs. 1 and 2 the stator transducers were concentrated on the suction surface, toward the trailing edge, in the uncovered portion of the airfoil surface. Sites 1 through 10 were on the suction surface. Site 11 was on the trailing edge mean camber line and Sites 12 through 15 were on the pressure surface toward the trailing edge. Site 12 was shifted slightly spanwise so as not to interfere with Site 10 on the opposite side of the airfoil. The transducers were concentrated toward the aft end of the stator since the interaction was expected to be strongest here due to close proximity to the rotor.

As can be seen in Figs. 1 and 3 the rotor transducers were concentrated on the suction surface, toward the leading edge. Sites 1 through 10 were on the suction surface. Site 11 was on the leading edge mean camber line and Sites 12

through 15 were on the pressure surface toward the leading edge. The transducers were concentrated toward the front of the rotor since the interaction was expected to be strongest here due to close proximity to the stator.

Signal conditioning and preliminary amplification for the transducers were provided by a circuit developed specifically for this type of application by UTRC. These units were mounted as near to the transducers as possible to minimize noise pickup. In the case of the rotor transducers, the electronics were located within the rotor hub. The electronics for the stator transducers were mounted to the rig outer casing adjacent to the instrumented stator. The signals were then appropriately routed to the high response data system.

Both the rotor and the stator had 10 thin film gages distributed around each airfoil at midspan (Figs. 4 and 5). These gages were custom manufactured for this application by DISA. The custom gage configuration was similar to the DISA model 55R47 but it allowed all lead connections to be confined to a region near the tip of the stator and to a region near the root of the rotor where they would create no significant disturbances in the airfoil boundary layers. The gages themselves were bonded into depressions which had been chemically etched into the airfoil surfaces to a depth of 0.003 inch. The result was a smooth airfoil surface which would not artificially trip the boundary layer.

As can be seen in Figs. 1 and 4, the stator gages were concentrated on the suction surface and toward the aft end. Gages were mounted at Sites 1 through 7 (Fig. 1), between Sites 7 and 8 (referred to as Site 7.5), at Site 9 and on the pressure surface at Site 13. The numbers on Fig. 4 do not refer to Site numbers.

As can be seen in Figs. 1 and 5, the rotor gages were also concentrated on the suction surface but toward the leading edge. Gages were mounted on the suction surface at Sites 2 through 9, and on the pressure surface between Sites 13 and 14 (referred to as Site 13.5) and between Sites 14 and 15 (referred to as Site 14.5).

The gages were operated in a constant temperature mode at a nominal resistance ratio of 1.5. The anemometer modules for the rotor gages were located within the rotor hub. These units were developed at UTRC specifically for on-rotor measurements and require no adjustments after initial setup. The gages mounted on the stator were operated by rack-mounted equipment, placed as close as possible to the rig. All anemometer outputs were appropriately routed to the high response data system.

The high response pressure transducer output and the thin film gage output were acquired and recorded in digital form for subsequent off-line processing by the Aeromechanics Transient Logging and Analysis System (ATLAS) which accepted up to 26 channels of data. Each channel may be amplified and filtered as required. The heart of the system was a 26 channel transient recorder which digitized and stored each channel simultaneously at sampling rates up to 200 kHz as selected

by the operator. System control was provided by an Perkin Elmer 7/16 minicomputer system which interfaced with the operator through a graphics display terminal. The data system was capable of self-calibration using a built in programmable voltage standard which was under computer control. Data were recorded on a 9-track digital magnetic tape for subsequent processing. The system offered several modes of operation ranging from fully manual, where each step in the sequence (calibration, acquisition, and recording) was under operator control with the capability of aborting at any time, to fully automatic where these tasks were computer controlled according to preset parameters. Data acquisition may be initiated manually, by the computer, or on receipt of an external trigger pulse. For this program, the system was run in the external trigger mode so that data could be synchronized with the rotor position. An optical sensor (Optron, OPB-253-A) which detected the passing of a polished rotor blade tip provided the trigger pulse. The system was programmed to self-calibrate and then to acquire and write onto tape 100 scans (i.e., 100 rotor revolutions) of data. Each scan consisted of 1024 samples for each channel acquired at 40,000 samples per second. Typical rotor speeds yielded data over approximately 5 blade pitches (roughly 200 samples per blade passing period). The external triggering insured that data acquisition always began at the same relative position of the rotor and stator. Since the speed of the rig was very stable, the 100 scans taken at each flow configuration could be averaged to remove random variations in the blade surface pressures (referred to as phase-locked or ensemble averaging). This was done in an off-line reduction program which simultaneously converted the system output to pressure coefficient form using the internal voltage calibration and operator supplied scale factors for the transducers. The thin film gage data were not averaged but rather was reduced on an instantaneous (rev. by rev.) basis to preserve any random fluctuations which might signify turbulence or separation.

2. Rotor-Stator Aerodynamic Interaction

2.a Steady-State Pressure Distributions

The results of the steady-state stator and rotor midspan pressure distribution measurements are summarized in Figs. 6 and 7 respectively. The steady pressure coefficient (\bar{C}_p) for the stator (Fig. 6) was based on the measured stator inlet total pressure and a midspan exit static pressure based on a free vortex interpolation between the measured flowpath static pressures at the hub and tip. The measured data (symbols) were compared with a theoretical distribution (curve) based on the method of Caspar et al. (Ref. 27). The total pressure loss input to the analysis was based on the measured loss ($Y_2 = 0.04$) and the stream tube contraction ($h_2/h_1 = 0.996$) was based on a design through-flow analysis. The excellent agreement between the measured and computed results was obtained by varying the exit flow angle until a best match occurred. For the 15 percent axial gap this occurred at an exit flow angle of 22.5° for all three values of (C_x/U) and at which data was obtained (0.68, 0.78 and 0.96). At the 65 percent axial gap the data was also invariant with (C_x/U) and differed from the 15 percent gap data by no more than 0.03 in \bar{C}_p . This very small difference occurred in the throat. Practically speaking then, the stator steady-state pressure distribution was invariant with rotor speed and rotor-stator axial gap and the data agreed well with potential flow for an exit angle of

22.5°. From the pressure distribution it could be seen that the suction surface recompression occurred smoothly from the throat to the trailing edge, showing no evidence of boundary layer separation. Previous surface flow visualization studies had indicated the same result of attached and nearly two-dimensional boundary layers on both the suction and pressure surfaces of the stator at midspan.

The steady state pressure coefficient for the rotor (Fig. 7) was based on an incident relative total pressure whose level was inferred from the surface static pressure measured on the rotor pressure surface at 24-percent chord. This method was described in greater detail in Refs. 25 and 26. As with the stator, the rotor exit midspan static pressure was based on a free vortex interpolation between measured values at the hub and tip. Measured and computed (Ref. 27) pressure distributions are shown for all three values of (C_x/U) examined. The total pressure loss input to the analysis was based on a previously measured value ($Y_1 = 0.33$, Ref. 26) and the stream tube contraction ($h_2/h_1 = 1.015$) was based on a design through-flow analysis. Here again the excellent agreement between the measured and computed results was obtained by varying the inlet and exit flow angles until a best match occurred. At the 15 percent axial gap (Fig. 7) this occurred for an exit angle of 26.2° for all three values of (C_x/U) . At the 65-percent axial gap the pressure coefficient in the throat region ($X/B_x = 0.7$) was slightly higher ($\Delta C_p = 0.06$) and a match was obtained for an exit flow angle of 25.5° for all three values of (C_x/U) . The present data taken at this larger spacing was practically identical with data taken earlier at this spacing (Refs. 25 and 26) where the same exit angle provided a best match. The rotor thus did indicate a weak dependence of the steady state pressure distribution on axial spacing.

The best match with the data at the three values of (C_x/U) , 0.68, 0.78 and 0.96 occurred at rotor relative inlet angles of 45°, 40° and 35° respectively. These inlet flow angles gave excellent agreement at both axial spacings and they correspond to an absolute stator exit angle of 22° (compared to the 22.5° flow angle inferred from the stator pressure distributions). This agreement was believed to be excellent and within the level of experimental and analytical matching uncertainty.

In summary, the steady-state flow over the rotor showed a weak dependence on axial gap and the expected dependence on relative inlet air angle. The suction and pressure surface flows were well behaved, showing no indication of boundary layer separation over the entire inlet flow angle range from 35° to 45°. The absence of midspan boundary layer separation on either surface had been demonstrated by previous flow visualization (Ref. 26) and by more extensive flow visualization described in part III.C of this report. Note, however, that there was strong radial flow on the pressure surface (Refs. 25, 26 and part III.C below) due to inviscid effects. For reasons that were suggested in Ref. 26, and which will be discussed in part III.C below, these radial flows had little impact on the pressure distribution. There were also strong radial flows on the rotor suction surface due to secondary flow in the endwall regions. It was shown in Ref. 26, (and also in part III.C below) that these radial flows do penetrate to the midspan region downstream

of the throat. It will be shown in part III.C below, however, that these endwall secondary flows had a relatively weak impact on the pressure distributions, particularly at midspan.

2.b Unsteady Pressure Envelopes

The envelopes defined by the maximum and minimum unsteady pressures on the stator and rotor at the 15 percent gap and at the design conditions ($C_x/U = 0.78$ ($\beta_1 = 40^\circ$)), are shown superimposed on the theoretical steady state pressure distributions in Figs. 8 and 9 respectively. The maximum and minimum of the periodic (phase-lock-averaged) pressure fluctuations are plotted symmetrically above and below the computed result at each site. In order to relate this data to physical locations on the airfoils (Fig. 1), Site numbers are indicated (Figs. 8 and 9). For the stator (Fig. 8) it may be seen that the amplitude decreased on the suction surface going from Site 1 aft to Site 4 (which was located just downstream of the throat, on the uncovered portion of the suction surface, Fig. 1). From Site 4 aft toward the trailing edge (Site 10) the amplitude increased to ± 15 percent of Q_2 . There was an abrupt drop in amplitude at the trailing edge at Site 11 on the mean camber line. The amplitude increased going around to the pressure surface (Site 12) and then decreased gradually going forward on the pressure surface (to Site 15). This periodically fluctuating pressure on the stator was due to the potential flow interaction with the rotor passing by downstream. Of particular interest were the relatively large amplitude (± 15 percent of Q_2) and the fact that the pressure fluctuations penetrate very far forward on the stator. The minimum amplitude at Site 4 was also of interest and it will be discussed below. When considering the unsteady potential flow fluctuations on the stator due to the rotor it should be kept in mind that the rotor was moving relatively slowly, i.e., at typically half the stator exit absolute flow speed (see Fig. 1).

The rotor unsteady pressure envelope at the 15 percent gap and at an inlet angle of 40° is shown in Fig. 9. There was a failure in the transducer at Site 1 and no data was obtained there. The amplitude generally decreased toward the trailing edge. On the suction surface, however, there was a weak minimum at Site 7 (reminiscent of the minimum at Site 4 on the stator) and on the pressure surface the decay with distance aft was very gradual. The amplitude at Site 5 on the suction surface was ± 18 percent of Q_2 . Near the leading edge (at Site 10) the amplitude of the fluctuation is ± 36 percent of Q_2 or ± 80 percent of Q_1 . On the pressure surface the amplitude is typically ± 9 percent of Q_2 . These large amplitude periodic pressure fluctuations on the rotor pressure and suction surfaces were due to the combined influences of (1) the potential (inviscid) flow and (2) the viscous wake of the stator passing by upstream. In the light of the presence of the stator wake it was not surprising that the fluctuation amplitude on the rotor (Fig. 9) was in general larger than that on the stator (Fig. 8). When considering the fluctuations on the rotor due to the stator it should be kept in mind that the stator was moving (relative to the rotor) at typically 80% of the rotor inlet relative flow speed (see Fig. 1).

2.c Unsteady Pressure Wave Amplitude and Phase

The unsteady pressure distributions on the rotor and on the stator all had as their reference initial time ($t = 0$) the instant when the stator trailing edge circle center was in line with the rotor leading edge circle center. This condition is illustrated by the top two airfoils in Fig 1. All events were referenced to this moment for both high response pressure and thin film gage instrumented rotors and stators. The unsteady stator and rotor pressures were examined in terms of fluctuation amplitude and phase (relative to $t = 0$). This data is presented in Fig. 10 for the stator at the 15 percent gap and in Figs. 11 and 12 for the rotor at the 15 percent and 65 percent gaps respectively. The stator results at the large spacing were not included here due to their very small amplitude but they will be discussed subsequently.

The fluctuating pressure data for the stator for the 15 percent gap is shown in Fig. 10. Included on the figure is (1) the theoretical steady state pressure distribution (\bar{C}_p), (2) the fluctuating pressure amplitude (max to min) distribution (\tilde{C}_p) and (3) the phase relationships of the various pressure maxima and minima (relative to $t = 0$), all three plotted against arc length from the trailing edge mean camber line (S) normalized by stator axial chord (B_x). For reference purposes the transducer sites are also indicated in the figure. The figure includes data for all three values of (C_x/U), 0.68, 0.78 and 0.96. Recall that \bar{C}_p was invariant with (C_x/U).

The variation in unsteady pressure amplitude around the stator can be seen clearly here (Fig. 10). The increase in amplitude on the uncovered portion of the suction surface toward the trailing edge and the minima occurring at Site 4 and at the trailing edge (Site 11) are particularly evident. The phase is indicated for the high (H) points of the pressure wave (maxima) and for the low (L1 and L2) points of the wave (minima). Included on the figure for comparison purposes is the phase of a disturbance traveling at the local convective velocity (C) and also the phase of a disturbance traveling at wheel speed (U). It can be seen that pressure waves were traveling upstream and downstream from about Site 5. This was close to the location where the fluctuation amplitude was at a minimum (Site 4). It appeared from the data that the pressure wave from the rotor blade first struck the uncovered portion of the stator suction surface around Sites 4 and 5 and that waves traveled fore and aft from that point. The low-pressure region of the forward traveling wave (L2) was distinctly separate from the low-pressure region of the rearward traveling wave (L1). Such a distinction could not be made for the high-pressure region (H).

In the uncovered portion of the channel (Sites 4 through 10) the pressure maxima (H) were traveling aft faster than the local flow velocity and the minima (L1) were traveling aft more slowly than the local flow velocity but not as slow as wheel speed. These differences were evident in the different slopes of the phase plots in these regions. This indicated a steepening of the pressure rise

portion of the wave as it proceeded aft. This distorted wave form was indeed seen in the data near the trailing edge (Fig. 14) and its source will be discussed subsequently. There was a sudden variation in amplitude and phase around the trailing edge. This indicated that for unsteady flow of this type, i.e. with reduced frequency on the order of unity, that the steady Kutta condition of no loading at the trailing edge no longer applied. This matter will be explored more fully below in the discussion of Fig. 17.

Another interesting feature of the unsteady pressures on the stator was seen by comparing the nearly constant phase on the suction surface between Sites 2 and 4 (located just upstream of the throat) with that on the pressure surface at Sites 12 through 15. If these sites had been on the same channel instead of on the same airfoil, i.e., if Sites 12 through 15 had been on the pressure surface of the adjacent airfoil facing Sites 2 and 4 on the suction surface, then they would all have been very nearly in phase. Moving Sites 12 through 15 to the adjacent airfoil would have advanced their phase by $[1 - (22/28)] = 0.21$ of a blade passing period (or an inter-stator phase angle of 77°). This would be very close to the phase of Sites 2 and 4. The conclusion was that when viewed as a channel, the fluctuations of the flow on both sides of the channel were nearly in phase.

The fluctuating pressure data for the rotor for the 15 percent gap is shown in Fig. 11. The format is the same as that for the stator (Fig. 10) except that for the rotor arc length (S) was measured from the leading edge stagnation point location at a $(C_x/U) = 0.78$ ($\beta_1 = 40^\circ$). Unlike the stator, the rotor steady state pressure distribution was a function of (C_x/U) . The three distributions of the computed steady pressure distribution (\bar{C}_p) have been included in the figure. Aspects of the fluctuating pressure distribution (C_p') evident in the data include very high amplitudes at the leading edge (truncated at $C_p' = 0.5$ in the figure), an amplitude decreasing with distance on the pressure surface, a local minimum amplitude on the suction surface between Sites 6 and 7, a local maximum between Sites 4 and 5 and a rapid decay in amplitude back to Site 2. Recall that the transducer at Site 1 was inoperative. The peak in amplitude at the leading edge occurred at Site 10 which was at the minimum X location (Fig. 1). For inlet flow angles (C_x/U) of 35° (0.96), 40° (0.78) and 45° (0.68) the fluctuation amplitude (C_p') at Site 10 was 0.98, 0.72 and 0.61 respectively.

The phase behavior of the rotor was considerably more complicated than that of the stator. The high pressure part of the wave (H) and one of the low pressure parts (L_1) were moving aft on the suction surface at approximately the local convective velocity (W). These high and low pressure regions will be shown to be associated with the flow between stator wakes. The low pressure region (L_2) will be shown to be associated with the flow in the stator wake and it could be seen to impact the entire suction surface almost at once (at $t \approx 0.5$), i.e., with a very high phase velocity. This matter will be discussed below in conjunction with Fig. 22, however, the possibility that the stator wake impacted a long region

of the rotor suction surface all at once at $t \approx 0.5$ was not unreasonable. The uncovered portion of rotor suction surface (Sites 5 through 9) reached the stator wake at about $t \approx 0.5$. This could be seen in Fig. 1 by extending the stator trailing edge mean camber line into the rotor channel. Using this extended mean camber line as an estimate of the stator wake position it could be seen that when the rotor had moved down 1/2 of the stator pitch ($t = 0.5$) the uncovered portion of the rotor suction surface was in line with the stator wake. An event on the rotor occurring at $t = 0.5$ (such as L_2) would occur on the stator at $t = 0.5 \times (N_R/N_S) = 0.64$. Thus, the nearly constant phase low pressure region on the rotor suction surface (L_2) occurred at nearly the same instant as the constant phase low pressure region on the stator suction surface (L_2), i.e., at $t \approx 0.64$ (Fig. 10). Note that at this instant the stator trailing edge stagnation point streamline and the rotor leading edge stagnation point streamline were nearly coincident.

The fluctuation on the rotor pressure surface was in nearly constant phase. As with the stator, if the pressure surface sites had been in the same channel as the suction surface sites (as opposed to on the same airfoil), i.e. if Sites 13 through 15 had been on the pressure surface of the adjacent airfoil facing Sites 2 through 10 on the suction surface, then the low pressure regions L_2 and L_3 would have been approximately in phase. Moving Sites 13 through 15 to the adjacent airfoil would have retarded their phase by $[(28/22) - 1] = 0.27$ of a stator passing period (or an inter-rotor phase angle of 98°). This would have put them close to the phase of Sites 2 through 10. Thus, when viewed as a channel the events at L_2 and L_3 were occurring nearly simultaneously, particularly for the two higher values of (C_x/U) .

The fluctuating pressure data for the rotor at the 65-percent gap is shown in Fig. 12. The fluctuation amplitude at this larger spacing is reduced by typically a factor of 2 relative to that at the 15-percent gap. The high amplitude at the leading edge had moved from Site 10 (the minimum X location, Fig. 1) at the 15-percent gap to Site 11 (the mean camber line location) at the 65-percent gap. The magnitude of this peak had been reduced by typically a factor of 6. There was a second amplitude maximum at Site 9 for a (C_x/U) of 0.96. This maximum may be related to the very steep gradient in the steady state pressure distribution (\bar{C}_p) at this location due to the positive incidence leading edge overspeed. It seemed reasonable to expect relatively high amplitude fluctuations to occur at regions of steep gradients in the steady state pressure. This same reasoning provided some explanation for the curious increase in fluctuation amplitude observed on the stator at Site 1 toward the leading edge. The gradient of the steady state pressure was relatively steep there also. The phase plot indicated that the high pressure part of the wave (H) on the suction surface was moving aft at about the local convective velocity but that the low pressure part (L) was moving aft much more slowly, at about wheel speed. This was similar to what occurred on the stator. A large phase shift around the leading edge was also evident in the data.

The stator data at the 65 percent gap was not presented in the manner of Figs. 10 through 12 due to the relatively low amplitude of the pressure fluctuations that occurred at this larger spacing ($\bar{C}_p = 0.02$). The reason for this rapid drop in stator amplitude with increased axial gap will be discussed in conjunction with Fig. 18.

2.d Instantaneous Pressure Distributions

In an effort to provide some indication of the complex nature of the instantaneous pressure distributions (C_p'), the data was plotted at several instants, i.e. at several values of t , for the stator and the rotor in Figs. 13 and 14 respectively for the 15 percent gap and for a (C_x/U) of 0.78. The figures included the steady state distributions (\bar{C}_p), the symmetric envelope formed by the maximum and minimum local instantaneous pressure fluctuations (\bar{C}_p) and the distributions of the instantaneous pressure fluctuations (C_p') within the envelope, all versus normalized axial distance. For the sake of clarity only suction surface fluctuating pressure data has been plotted.

The stator results (Fig. 13) have been plotted when the fluctuating pressure (C_p') at Site 8 was a maximum ($t = 0.05$), when it was zero and dropping ($t = 0.33$), when it was a minimum ($t = 0.71$). These events were roughly evenly spaced in time due to the non-sinusoidal wave shape of the fluctuation (mentioned above in conjunction with Fig. 10) which had a rapid pressure rise and a relatively slow drop. Since the instantaneous fluctuating pressure distributions had many extremes and many zero crossings it would be difficult to make an accurate estimate of the instantaneous force on the airfoil without a far more dense array of instrumentation around the entire perimeter of the airfoil. Similar results for the rotor were presented in Fig. 14 when the fluctuating pressure (C_p') at Site 8 was zero and dropping ($t = 0.15$), when it was a minimum ($t = 0.42$), when it was zero and rising ($t = 0.68$) and when it was maximum ($t = 0.87$). These events were roughly evenly spaced in time due to the more sinusoidal nature of the wave form on the rotor. As with the stator, any estimate of unsteady force would clearly require many more transducer sites than were available in this experiment. Both the stator and the rotor data demonstrated the very complex nature of the pressure fluctuation that occur at reduced frequencies on the order of unity.

This same stator and rotor data was presented in a different format in Figs. 15 and 16. These plots were prepared by Dr. Kevin Mach (UW-MAL) using the PERSYS graphics routine. These figures were composite pressure-time histories for each pressure transducers. The data for both airfoils included the suction and pressure surface sites and they were located along the coordinate axis at distances proportional to their arc length distance from the leading or trailing edge. Data was shown for several blade passing periods but for the sake of clarity the data at every instantaneous time was not included. Only enough instantaneous data was included to give a clear indication of the pressure-time history.

Since the most interesting features of the stator data were the low pressure regions it has been plotted with pressure decreasing in the upward direction (Fig. 15), i.e., low pressure regions appear as ridges and high-pressure regions appear as valleys. The increase in unsteadiness amplitude from Site 5 aft toward the trailing edge at Site 11 can be seen along with the fact that the low-pressure region L1 was a wave moving slowly aft on the airfoil, i.e., it was moving aft at a finite speed as seen by the way in which the wave crossed the lines of constant time. In contrast, the wave moving forward from Site 5 toward Site 1 (L2) was nearly at a constant phase, i.e., the low pressure occurred at nearly the same instant for Sites 4 through 2. These phase relationships have also been discussed above in connection with Fig. 10. An unusual feature evident in Fig. 15 was that the minimum amplitude at Site 4 (see also Fig. 10) occurred due to the wave moving toward the trailing edge being out of phase with the wave on the forward portion of the suction surface. Said another way, the low pressure region at Sites 1 through 3 (L2) had its origin in the high-pressure region at Site 5 and the low-pressure region moving aft from Site 5 (L1) had its origin in the high-pressure region at Site 4. The abrupt changes in amplitude and phase at the trailing edge and the nearly constant phase behavior on the pressure surface could also be seen.

The rotor data is presented viewed from a different perspective and with pressure increasing in the upward direction in Fig. 16. The salient feature here was the high amplitude on the suction surface near the leading edge. The phase shift in the high-pressure region (H) and in the low-pressure region (L1) as they moved aft along the suction surface was evident here (and also in Fig. 11). The nearly constant phase of the suction surface low-pressure region (L2) and the pressure surface high (H) and low (L3) regions could also be seen. This figure clearly illustrated the extremely high amplitude near the leading edge and its decay along the suction surface as well as the abrupt drop in amplitude going toward the pressure surface.

2.e Unsteady Trailing Edge Loading

The fact that the fluctuating pressure produced unsteady loading at the stator trailing edge was illustrated in Fig. 17 where the pressure time history at the trailing edge mean camber line (Site 11) was compared with those slightly upstream on the suction and pressure surfaces (Sites 10 and 12 respectively). The existence of this unsteady loading at the stator trailing edge was mentioned above in conjunction with Fig. 10. From Fig. 10 it could also be seen that any phase shift in the pressure wave as it proceeded from Sites 10 and 12 downstream to the trailing edge (a distance of 5.3 percent to 6.3 percent of axial chord) was small relative to the phase differences that existed between these sites. This was particularly true in comparing Sites 11 and 12 since the phase gradient on the pressure surface was very small.

The fact that the pressure fluctuations at Sites 10, 11 and 12 were (1) all considerably out of phase and (2) of significantly different amplitude, indicated the existence of unsteady trailing edge loading. The expectation (by Gostelow, Ref. 9 and by Satyanarayana and Davis, Ref. 10) that unsteady trailing edge loading would become significant above a reduced frequency of 0.6 was born out by this data. The reduced frequency for the stator was based on the true chord (B) and the absolute stator exit velocity (C) as follows.

$$k = \left(\frac{N_R \Omega B}{2C} \right) = \left(\frac{N_R}{2} \right) \left(\frac{B/R_m}{C_x/U} \right) \sin \alpha$$

For the range of values of (C_x/U) tested, 0.68, 0.78 and 0.96, the reduced frequencies were 2.7, 2.3 and 1.9. From these results it appeared likely that any analytical model of the rotor-stator interaction process that did not account for unsteady trailing edge loading would be limited to low reduced frequencies.

The stator trailing edge pressure fluctuations (Fig. 17) were also examined with respect to their wave shape. In the discussion of Figs. 10 and 13 it had been pointed out that near the stator trailing edge the wave form was one of a rapid pressure rise ($\Delta t = 0.3 \sim 0.4$) and a relatively slow pressure drop ($\Delta t = 0.6 \sim 0.7$). This could be seen in the data from Sites 10, 11 and 12. Also included in Fig. 17 was a prediction of the unsteady pressure wave based on the predicted (Ref. 27) steady potential flow around the rotor. At an axial location upstream of the rotor leading edge corresponding to the 15 percent axial gap between the stator trailing edge and the rotor leading edge, the steady rotor pitchwise static pressure variation was used to determine C_p' at the stator trailing edge, i.e. the steady spatial variation in the rotor frame of reference was viewed as a temporal variation in the stator frame of reference (ignoring the presence of the stator). It was seen that this rather simple approach resulted in a surprisingly accurate prediction of the wave form, amplitude and phase of the stator trailing edge pressure fluctuations. This relatively close agreement was contrary to the results by Parker (Ref. 5) which indicated that the local amplitude with interaction was roughly three times that without interaction. Had this been the case the computed amplitude in Fig. 17 would have been approximately half its actual value. This point will also be discussed in conjunction with Fig. 18.

The stator trailing edge data was also examined to see if there was any evidence of pressure fluctuations due to the Karman vortex street. For a Strouhal number (St) of 0.21 the shedding frequency was determined as follows.

$$f = St \cdot C/d_s$$

or

$$(f/N_R\Omega) = St \cdot \left(\frac{\tau_R}{d_S}\right) \left(\frac{(C_x/U)}{\sin \alpha}\right) = 11.8 \text{ @ } (C_x/U) = 0.78$$

Spectral analysis of the analog (on-line) output from the high-response pressure transducers at Sites 10 through 12 revealed a small peak at a frequency of 11.5 times rotor passing frequency (at a C_x/U of 0.78) at all three sites. The Reynolds number based on trailing edge diameter (d_S) and stator absolute exit velocity (C) was 2.2×10^4 . This was well above the minimum Reynolds number (10^3) at which Roshko (Ref. 28) demonstrated that a constant Strouhal number of 0.21 was established for flow past a circular cylinder. The existence of a Karman vortex street on a turbine airfoil was in agreement with similar observations by Lawaczeck and Heinemann (Ref. 29). Ensemble averaging the data over 100 rotor revolutions totally suppressed this effect in the averaged data.

2.f Decay of Unsteadiness with Axial Gap

The same potential flow analysis (Ref. 27) that was used to predict the amplitude, phase and wave form at the stator trailing edge (Fig. 17) was also used to predict the amplitude of the pressure fluctuations (C_p) on the rotor and the stator as the axial gap separating them was changed from 15 percent to 65 percent of axial chord. The theoretical potential flow results and the measured data are shown in Fig. 18. As in Fig. 17, the tangential variations in the computed static pressure downstream of the stator and upstream of the rotor were normalized with the exit dynamic pressure of the rotor and the stator respectively. Note that the predicted C_p for the stator was a function of (C_x/U) due to the changing rotor incidence but that for the rotor it was independent of (C_x/U) . The measured data were from the aft end of the stator suction surface, Sites 7 through 10 (see Figs. 1 and 10), and from the midchord region of the rotor suction surface, Sites 4 and 5 (see Figs. 1 and 11).

For the prediction on the stator the agreement between the measured and predicted results was excellent as to level and the trends with (C_x/U) and with relative axial spacing. When the data was viewed in this manner it appeared possible that the indications from Parker's (Ref. 5) results, that the presence of the upstream airfoil increased the fluctuation amplitude over what it would have been at that point without the airfoil present, may indeed be qualitatively correct. For the change in axial spacing from 15 percent to 65 percent gap there was a reduction by about a factor of ten in unsteady pressure amplitude. Parenthetically, it was because of this very low amplitude that the stator data at 65 percent gap was not presented in the manner of Fig. 10.

For the unsteady pressure amplitude on the rotor, however, the decrease with axial gap predicted by potential flow was much too strong and in general the predicted amplitude was much too low. This suggested that the influence of the stator wake was considerably stronger than that of the stator potential flow in determining the amplitudes on the rotor (at least at Sites 4 and 5). The possibility that this unsteadiness on the rotor was primarily due to the stator wake was further strengthened when it was observed that the amplitude decay was nearly proportional to $X^{-1/2}$, i.e. the amplitude was decaying in the same manner as a wake. This observation was further supported by the fact that due to the velocity triangles of a turbine one would expect the stator wakes to migrate toward the rotor suction surface. In contrast to this behavior on the suction surface it was noticed that near the rotor leading edge stagnation point (Sites 11 and 12), while the amplitudes were still much larger than predicted by potential flow, the decay in amplitude with increasing axial gap was much closer to the potential flow prediction. On the rotor both viscous and inviscid mechanisms of rotor-stator interaction are occurring, whereas on the stator it is purely a potential flow effect.

The computed results shown in Figs. 17 and 18 made possible a number of additional observations regarding the stator data presented in Fig. 10. Based on the decay with axial distance of the potential flow unsteadiness on the stator due to the rotor (Fig. 18), one would expect the unsteady pressure amplitude at the 15% gap condition to decrease by approximately a factor of ten going from the trailing edge forward on the stator suction surface to Site 4. From Fig. 10 it can be seen that this is very close to what was measured. From Fig. 17 it was shown that the unsteady pressure wave form on the stator (due to the rotor potential flow) closely matched the measured wave form near the trailing edge (at Sites 10, 11, 12). It is reasonable, therefore, that the low pressure region (L_1) is moving downstream on the stator suction surface at a speed very close to wheel speed (U), i.e., it is moving with the rotor. However, the reason for the much higher phase velocity of the high pressure region (H) on the suction surface is not clear. As mentioned above, the different phase velocities of the high and low pressure regions cause a steepening of the pressure rise portion of the wave as it travels downstream. This change in wave form is also evident in the potential flow results. At an axial location 15% ahead of the rotor the wave has a non-sinusoidal rapid pressure rise (as seen in Fig. 17). However, as also seen in the data, at an axial location 50% ahead of the rotor the wave was nearly sinusoidal.

2.g Thin Film Gage Results - Stator

Up to this point discussion of the high response data has been focused purely on the ensemble averaged pressures. Turning our attention now to the thin film gage data it must be kept in mind that this data must be viewed on an instantaneous basis. All of the thin film data represented a portion of the data acquired over a single rotor revolution. It was not averaged over

100 revolutions as was the pressure data. This approach permitted one to distinguish, for example, the difference between laminar and turbulent portions of the flow. On all of the thin film data plots increased power input to the gage resulted in an increased output, i.e. positive (upward) deflection. The gages were all operated at the same sensitivity and hence the output amplitudes were directly comparable.

Typical thin film data for the stator at a (C_x/U) of 0.78 and a 15-percent gap is shown in Fig. 19 for most of the gages located on the suction surface (Sites 2 through 9). Site 2 upstream of the throat (Figs. 1 and 10), indicated nearly steady laminar flow (as did Site 1). This was somewhat surprising in light of the pressure fluctuation at this Site (Fig. 10). At Site 3, at the throat and just downstream of the minimum pressure, the flow was still laminar but there was a weak oscillation at rotor passing frequency. At Site 4, in the recompression region, a very distinct high frequency oscillation was present superimposed on the oscillation at rotor passing frequency. This high frequency (approximately 6 kHz based on Fig. 19) was independent of (C_x/U) i.e., rotor speed. It was seen on the spectrum analyses as a broad band from 5 to 7.5 kHz. It was seen in the instantaneous Kulite data and also, surprisingly, in the ensemble averaged Kulite data. Since boundary layer transition was expected to occur at or about Site 4, these oscillations were examined in the light of Tollmien-Schlichting waves. Based on the results presented in Ref. 30 (Figs. 16.12 and 16.18), and those presented by Fink (Ref. 31) and by Erens and Chasteau (Ref. 32) it was estimated that Tollmien-Schlichting waves would have had a frequency of 4 to 7 kHz in the present stator situation. The conclusion reached was that these were indeed Tollmien-Schlichting waves. In addition, their presence gave a high level of confidence that the thin film gages had been mounted sufficiently flush to the airfoil surface so as to have no significant effects on the boundary layer. It was also noteworthy that the Tollmien-Schlichting waves could be observed on the high-response pressure transducer at this location. The stator suction surface boundary layer was turbulent from Site 5 downstream to Site 9 near the trailing edge (Figs. 1 and 19). Recall that Site 9 was the aft-most gage. The superimposed periodic unsteadiness increased in magnitude significantly as the trailing edge was approached.

On the pressure surface the thin film gage at Site 13 indicated a laminar boundary layer with a weak periodic oscillation at blade passing frequency. The data was very similar to that at Site 3 on the suction surface. That the flow was laminar was not unexpected due to the strong acceleration up to this point (Fig. 8).

When the rotor-stator axial gap was increased from 15 percent to 65 percent the frequency of the Tollmien-Schlichting waves and the Site at which they were observed on the suction surface were unchanged. The random fluctuations in the turbulent region were of the same magnitude (as at 15 percent) but the periodic fluctuations were virtually eliminated. This was consistent with the large reduction in the amplitude of the periodic pressure fluctuations that occurred when the gap was increased to 65 percent.

2.h Thin Film Gage Results - Rotor

Samples of the rotor thin film gage data for the three rotor inlet gas angles (35° , 40° and 45°) were shown for the 15 percent gap in Fig. 20 and for the 65 percent gap in Fig. 21. Data was shown for Sites 5 and 7 located on the suction surface toward the leading edge. For the rotor, periodic events occurred at the stator passing frequency which was indicated on the figures relative to $t = 0$. There was a strong unsteadiness at stator passing frequency at Site 7 (near the leading edge) which was greatly reduced at the further downstream location on the rotor (Site 5). Both locations for both spacings showed regions of large random fluctuation due to the turbulence in the stator wake superimposed on the periodic fluctuation. At Site 7 there were portions of the stator passing period (between the stator wakes) where the randomness was very small. These occurred where the gage output was near a minimum. There were also indications of this type of behavior at Site 5, especially at the 45° inlet angle ($C_x/U = 0.68$) for 65 percent axial spacing. In general the portion of the stator passing period where the random fluctuations were small increased with increasing inlet gas angle, i.e. with reduced (C_x/U) or reduced turning. The reduced leading edge overspeed with reduced (C_x/U) at $\beta_1 = 45^\circ$ produced a laminar boundary layer on the rotor suction surface which was interrupted periodically by the impingement of the turbulent upstream stator wake. Evidence of these laminar regions at an inlet gas angle of 45° ($C_x/U = 0.68$) persisted all the way to the rotor trailing edge, particularly at the 65 percent gap. The gage near the leading edge at Site 8 indicated primarily periodic laminar flow (at all incidences) at the 15 percent gap and only a slight increase in randomness at the 65 percent gap. (The gage at Site 9 had become inoperative early in the program.) The essentially laminar behavior at Site 8 indicated that the leading edge overspeeds (Fig. 7) did not trip the boundary layer immediately. At the most positive incidence, however, the overspeed did appear to accelerate the transition process as seen by the increased random fluctuations in the low output regions between the stator wakes at both spacings. The periodic oscillation between laminar and turbulent boundary layer flow on the rotor suction surface was in agreement with similar observations made by Evans (Ref. 15) and by Speidel (as reported by Scholz, Ref. 14).

The output of the high response pressure transducer and the thin film gage at Site 7 on the rotor suction surface were compared at a (C_x/U) of 0.78 ($\beta_1 = 40^\circ$) at both axial spacings in Fig. 22. At the 15 percent gap it was seen that the high pressure region (H , as in Fig. 11) corresponded to the laminar region between stator wakes and that the low pressure region (L_2) corresponded to the turbulent region within the stator wakes. As the rotor passed through the stator wake, the wake impacted a long region along the suction surface at about the same instant. This can be seen in Fig. 11 by the fact that the phase of L_2 is nearly constant from Site 2 to Site 10. This effect could be seen in the thin film output as well as in the pressures. The initial development of the second low pressure region (L_1) is also indicated (Figs. 11 and 22).

At the 65 percent gap the high-pressure region (H) at Site 7 was again between the stator wakes and the low-pressure region (L) was in the wakes. It was observed that at this downstream location the increased width of the turbulent region was in agreement with the increase in wake width expected with downstream distance. The phase of the thin film output could only be distinguished in the data at the inlet flow angle of 45° . For this case the phase was not constant as L_2 has been at the close spacing (Fig. 11), but rather the wake moved down the airfoil as indicated by the (H) and (L) in Fig. 12.

The rotor pressure surface thin film gage output (Site 13.5) indicated weakly periodic turbulent flow at all combinations of spacing and incidence. The gage at Site 14.5 was inoperative. Note from Fig. 12 that even though the motion of the wake on the pressure surface could not be clearly distinguished in the thin film gage data, its effect on surface pressure was distinct. In particular, unlike the constant wake phase on the pressure surface (L_3) at the close spacing, at the large spacing the wake effect was proceeding aft on the pressure surface in a manner similar to that on the suction surface, i.e., the phase was not constant.

B. Unsteady Effects on Stator Heat Transfer

The stator heat transfer phase of the present program was conducted simultaneously with the aerodynamic measurements described above. At both axial spacings (15 percent and 65 percent axial gap) stator heat transfer data was acquired at the same three flow conditions at which aerodynamic data had been acquired, i.e., values of (C_x/U) of 0.68, 0.78 and 0.96. The results indicated that reducing the axial gap from 65 percent to 15 percent caused an increase in the heat transfer coefficient of typically 25 percent. The measurement technique and the experimental results are discussed in the following sections.

1. Stator Heat Transfer Model and Instrumentation

The basic approach to the heat transfer measurement was the same as that employed in Refs. 23 and 33. It consisted of fabricating a low thermal conductivity foam model of the stator and covering it with an instrumented heater strip. As with the aerodynamic measurements described above, the heat transfer measurements were made at the midspan section of the stator. As discussed in Section III.A.1 the flow in this midspan region was known to be strongly two-dimensional, free of end effects and attached all the way to the trailing edge.

Two stator heat transfer models were fabricated, one for the suction surface and one for the pressure surface. The partially completed pressure surface model was shown in Fig. 23 viewed from the suction surface. An aluminum stator airfoil used in the turbine model was used to make a mold. This mold was constructed using Hydrocalic cement which had extremely low shrinkage and gave an accurate duplicate of the original metal airfoil. A metal structure consisting of hub and tip airfoil sections and two spanwise spars was constructed to provide structural integrity to the model. Urethane foam (Isofoam^R, Witco Chemical) was poured into the mold around the metal structure to form an accurate duplicate of the metal airfoil. This foam was chosen as a suitable airfoil material since its thermal conductivity was very low ($0.02 \sim 0.03$ Btu/hr ft °F), being close to that of still air. The effect was to minimize thermal conduction within the model. Bus bars (visible in Fig. 23) were installed to provide power to the heater foils. The foil was 0.001 inch thick stainless steel, which when electrical current was passed through it provided a nearly uniform surface heat flux. This foil was glued to one surface (pressure or suction) of the airfoil and typically 20 thermocouples (0.003 inch diameter Chromel-Alumel) were welded to its back surface through predrilled holes in the foam. The foil was then wrapped around and glued to the remaining surface of the airfoil and connected to the bus bars. This was the condition of the airfoil in Fig. 23.

The back surface of the airfoil (i.e. with the buss bars and thermocouple leads) was restored to its original contour with joint compound and the entire airfoil was sprayed with flat black paint to obtain a known emissivity. The separate suction and pressure surface instrumented airfoils were mounted in

the turbine model with several unheated airfoils separating them. The airfoils and endwalls in the channels facing the instrumented stator surfaces were also spray painted flat black to obtain a known emissivity. The thermocouples were connected to a programmable thermocouple scanning device. Power to heat the foil was provided by a single low ripple regulated D.C. power supply. The D.C. power passing through the foil was measured using two precision shunt resistors and a digital voltmeter.

2. Unsteady Effects on Stator Heat Transfer - Results

All of the stator heat transfer testing was conducted at a constant stator Reynolds number (based on axial chord and exit velocity) of 5.9×10^5 . All variations of (C_x/U) were obtained by changing the rotor speed. The tests were conducted with a nearly constant heater power input which gave temperature differences of typically 10°F to 49°F . At these levels, the radiant flux and the conduction loss (based on thermocouples on the back side of the airfoils) were typically 2 to 10 percent and 0 to 3 percent respectively of the total generated surface heat flux. Several thermocouples indicated little in the way of spanwise gradients on either airfoil.

The measured suction and pressure surface heat transfer data are presented in Fig. 24 along with the surface velocity distribution for a (C_x/U) of 0.78 as a function of distance from the stagnation point. The velocity distributions were included to provide perspective on the heat transfer data. The relative magnitude of the rotor speed ($U/C_1 = 0.78^{-1} = 1.28$) was included to demonstrate that it was moving relatively slowly behind the stator (see Fig. 1). The measured and computed (Ref. 27) velocity distributions and the locations where the boundary layers were either laminar, turbulent or had Tollmien-Schlichting oscillations, were all included. Recall that all of these were very insensitive to (C_x/U) as well as to axial gap. The same could not be said for the heat transfer results. They were presented in terms of a Stanton number based on the inlet flow velocity. The Stanton number distribution directly reflected the heat transfer coefficient distribution. A significant drop was observed in the Stanton numbers as the rotor-stator axial gap was increased from 15 percent to 65 percent, particularly on the suction surface. The heat transfer data were compared with laminar and fully turbulent calculations based on the theory by Carter and Edwards (Ref. 34). The boundary layer calculations were in turn based on the surface velocity distribution computed by the method of Caspar et al. (Ref. 27).

The suction surface heat transfer results (Fig. 24) indicated that the boundary layer was laminar to an (S/BX) of about 0.75 and turbulent from about 1.0 to the trailing edge. This was in good agreement with the known locations of laminar, transitional and turbulent flow based on the thin film data (from another stator airfoil). The source of the small difference in transition location for the two gaps was uncertain since the thin film (and Kulite) data indicated no change.

Generally speaking, at the 65 percent gap the measured and computed heat transfer results were in rather good agreement. However, with the rotor stator gap reduced to 15 percent the measured suction surface heat transfer coefficients increased by typically 25 percent. At this time the fundamental mechanism behind this increase is unclear. The pressure surface heat transfer results indicated that the boundary layer was transitional over its entire length and that the change in axial gap had a much weaker impact on the heat transfer coefficient there.

As indicated in Fig. 25, the Stanton number behavior at the higher and lower values of (C_x/U) was very similar. There were slight variations on the suction surface and little or no variations on the pressure surface. The data reported here were in qualitative agreement with that reported by Dunn and Hause (Ref. 24) where stator heat transfer data was reported both with and without a rotor present. Their data, however, indicated some sensitivity to the presence of the rotor on both the suction and pressure surface heat transfer.

C. Rotor Fullspan Aerodynamics

Upon completion of the unsteady aerodynamics and heat transfer phases of the program the fullspan rotor aerodynamics were examined. This testing was conducted exclusively at the larger axial spacing (65 percent gap). This was the axial gap used in all previous testing with this turbine model (Refs. 25 and 26). Two aspects of the flow were given particular attention. The first objective was to examine the strong radial flow known to be present on the rotor pressure surface (Refs. 25 and 26). The second objective was to examine the nature of the pressure surface flow under conditions of strong negative incidence stall. To these ends fullspan flow visualization and fullspan rotor pressure distribution data were acquired over a range of relative rotor inlet flow angles at midspan up to 85° (nearly axial). The bulk of this data was acquired at a fixed flow rate (fixed airfoil Reynolds numbers based on exit relative flow speed) by varying the rotor speed. At the largest incidence, however, a somewhat lower flow speed was used in order to keep the rotor speed down to a reasonable value (approximately 700 rpm).

The root, midspan and tip contours of the rotor airfoil were shown in Fig. 26. The airfoil axial chord was constant with span. The leading edge was leaned in the direction of wheel speed and the trailing edge was leaned approximately the same amount in the opposite direction. The nominal tip clearance was 1.4 percent of the rotor span.

The running conditions, that is, the values of (C_x/U) at which the flow visualization and pressure distributions were to be acquired were established as follows. The inlet flow angle at midspan was deduced from the measured rotor midspan pressure distribution by comparing measured and computed results. This process was described earlier in the discussion of the rotor-stator aerodynamic interaction results. Recall that in matching the measured and computed results the exit static pressure was based on measured hub and tip values, the stream tube contraction was based on the design value, the total pressure loss was based on the measured results in Ref. 26 and the rotor inlet relative total pressure was inferred from the measured pressure surface static pressure at 24 percent axial chord. The deduced exit flow angle used in Ref. 25 and 26 of 25.5° was shown to give excellent results in the present study (at the 65 percent gap). An inlet relative flow angle at midspan of 40° was deduced at a value of (C_x/U) of 0.78. The rotor inlet flow angle was then calculated as a function of (C_x/U) assuming that the absolute stator exit velocity was invariant with wheel speed. The results are shown in Fig. 27. A value of (C_x/U) of 0.42 was required to obtain a relative inlet flow angle of 85° . Values of (C_x/U) were selected which would provide 10° steps in the relative inlet flow angle from 45° to 85° . Also shown in the figure is the rotor inlet relative total pressure at midspan. This was calculated in the same manner as the flow angle.

1. Flow Visualization Technique

The flow visualization technique was the same as that employed in Refs. 25 and 26. In brief, it consisted of flowing a small amount of ammonia out of the rotor pressure taps. The ammonia caused blue streaks to appear on Ozalid paper which had been glued to the surface of the airfoil. The earlier studies had indicated that the limiting streamlines produced in this way are very insensitive to ammonia blowing rate.

2. Rotor Fullspan Aerodynamics - Results

With the test conditions established, fullspan flow visualization was carried out at each selected rotor midspan inlet flow angle. The results are shown in Figs. 28 through 34 for the inlet angle varying from 35° to 85° . At 40° ($C_x/U = 0.78$) and at 85° ($C_x/U = 0.42$) flow visualization was obtained on the suction surface and on the tip as well as on the pressure surface.

At 35° ($C_x/U = 0.96$, Fig. 28) the pressure surface had a strong radial flow toward the tip. Toward the trailing edge, where the flow accelerated strongly, the radial flow was greatly reduced. In addition, at the hub there was also relatively little radial displacement. This may have been due to the presence of the endwall corner and to the somewhat higher pressure surface flow velocity at the hub.

At 40° ($C_x/U = 0.78$, Fig. 29) the pressure surface limiting streamlines were similar to those at 35° . It was demonstrated by Dring and Joslyn (Ref. 26) that these pressure surface flow patterns were not a result of tip leakage. When the tip clearance was reduced from 1.4 to 0.1 percent span the flow pattern was the same except in the immediate vicinity of the tip. It will be demonstrated below that these radial deflections on the pressure surface can be attributed to the "relative eddy" present in the blade-to-blade flow.

The rotor suction surface (at 40°) was free of boundary layer separation and was very two-dimensional until it is influenced by the hub and tip secondary flow vortices downstream of the throat. The tip leakage flow is in the direction of the pressure gradient on the tip. An interesting feature of the tip leakage flow was the vena contracta located on the tip at the pressure surface corner (Fig. 29). The vena contracta was evident as a separation bubble on the pressure surface corner of the tip. Evidence of its presence could be seen in the increased width of the flow visualization streak at the corner. Its presence is more apparent on the actual airfoil than in the photograph. The blockage to the flow caused by this bubble could be expected to produce very high leakage flow velocities and very high heat loads along the pressure surface side of the tip.

Little change was observed in the nature of the pressure surface limiting streamlines as (C_x/U) was lowered and the rotor inlet flow angle was increased (Figs. 30 and 31), as long as the boundary layer remained attached. However, at a (C_x/U) of 0.50 ($\beta_1 = 65^\circ$) the pressure surface boundary layer was separated at the leading edge and over the entire span (Fig. 32). The flow within the bubble was generally radially outward and reattachment occurred at locations varying from about 20 percent axial chord at the root to 60 percent axial chord at the tip. As the rotor inlet angle was increased further the chordwise extent of the bubble also increased (Fig. 33). At the largest inlet flow angle examined (85°) the reattachment location varied from 50 percent chord axially at the root to 70 percent at the tip (Fig. 34). The impact of this separation bubble on the rotor pressure distribution will be discussed below.

As seen in Figs. 29 and 34 the suction surface limiting streamlines were seen to have changed little with the increase in inlet angle from 40° to 85° . However, the greater flow acceleration (convergence) in the rotor channel at 85° caused some reduction in the spanwise extent of the endwall secondary flow cells and an increased region of nearly two-dimensional flow at midspan.

The tip leakage flow changed significantly as a result of the increased inlet angle. At 85° there was flow from the suction surface onto the tip of the airfoil and then returning to the suction surface (Fig. 34). This reversal in the nature of the tip flow was a result of the severe leading edge overspeed occurring on the pressure surface due to the large negative incidence. This matter will be discussed in greater detail below.

In the analysis of the rotor fullspan pressure distributions both the inlet relative total pressure and the inlet relative flow angle had to be deduced. The midspan values of these parameters were shown in Fig. 27 as a function of (C_x/U) . Recall that they were based on the assumption that the stator exit absolute velocity vector was invariant with the rotor speed. An extension of this reasoning was applied for the fullspan data. The spanwise distribution of relative inlet total pressure (deduced from the rotor pressure surface static pressure at 24 percent chord) corresponded very closely to a constant rotary total pressure ($P_{T,rot} = \text{const}$) as shown in Fig. 35. The deduced relative total pressure for the seven spanwise locations from 6.25 percent span to 98 percent span and for the seven values of (C_x/U) examined are shown and compared to a curve corresponding to constant rotary total pressure. Except near the hub at the largest negative incidence ($C_x/U = 0.42$) the agreement is excellent. The inlet flow angles had to be treated differently.

Inlet flow angles were deduced at the seven spanwise locations at a (C_x/U) of 0.78. Based again on the assumption that the absolute velocity vector was invariant with rotor speed, the spanwise distributions at the other six values of (C_x/U) were calculated. The results are shown in Fig. 36. Note that the range

of angle variation increases considerably with span. In all forty nine cases (seven spans and seven inlet flow angles) the constant exit angle of 25.5° was found to give best agreement. As mentioned above, this was consistent with earlier experience (Refs. 25 and 26) with this rotor at this axial gap (65 percent).

The midspan measured and predicted pressure distributions are shown in Fig. 37 for the seven inlet flow angles from 35° to 85° . At 35° the suction surface decelerated from the leading edge overspeed all the way to the trailing edge. The pressure surface, on the other hand, accelerated from the leading edge stagnation point to the trailing edge. At 40° much of the suction surface had only a very small pressure gradient. At inlet angles from 45° to 85° the suction surface boundary layer accelerated smoothly to the throat (at about 60 percent chord) and then decelerated to the trailing edge. On the pressure surface there was a weak overspeed at 45° which increased in depth as the inlet angle was increased. It was known from the flow visualization results that pressure surface separation first appeared at 65° ($C_x/U = 0.50$). Its impact on the pressure distribution could be seen clearly at inlet flow angles of 75° and 85° where the predicted pressure surface leading edge overspeeds were not present in the data and where the predicted recompressions in the midchord region did not occur. The measured and computed pressure surface results came together at about the location where the reattachment was seen to occur, e.g. at 60 percent chord at 85° (Fig. 34). Finally, as could be seen from the measured and computed results, the stagnation point moved from a location at about 5 percent axial chord on the pressure surface at 35° , around toward the suction surface to a location at 0 percent axial chord at 85° . This would be an important consideration in any rotor leading edge cooling scheme design.

The fullspan nature of the rotor pressure distributions for the seven values of (C_x/U) examined is illustrated in Figs. 38 through 44. Each figure contains the measured and computed pressure distributions for the seven spanwise locations from 6.25 percent to 98 percent span. Recall that the tip clearance was 1.4 percent span. The input to the computed distributions was illustrated in Figs. 35 and 36. For values of (C_x/U) from 0.96 ($\beta_{lm} = 35^\circ$) down to 0.56 ($\beta_{lm} = 55^\circ$) the agreement between the measured and computed results was excellent from 12.5 percent span out to 87.5 percent span on both the suction and pressure surfaces. The strong radial flow due to the hub and tip secondary flow vortices appeared to have no significant effect on the pressure distributions at these span locations. As pointed out in Ref. 26, the strong radial flow on the pressure surface had little effect on the pressure distribution because the radial component was small relative to the total flow speed and the total dynamic pressure itself was very small there. Close to the hub at 6.25 percent span there was considerable unloading on the suction surface relative to the computed result. A very similar effect was observed by Langston et. al. (Ref. 35) in a turbine cascade experiment of similar geometry. At 98 percent there was a large departure from the computed results. The velocities on the pressure surface were much higher due to the close proximity of the tip corner. The suction surface velocities aft of the throat were also much higher than predicted. This was probably a result of the combined influences of the tip leakage and the tip secondary flow.

As (C_x/U) was reduced from 0.50 to 0.45 to 0.42, the effects of the negative incidence stall on the pressure surface became increasingly severe. At 0.50 (Fig. 42, $\beta_{lm} = 65^\circ$) the leading edge overspeed was not nearly as well predicted from 75 percent span outward as it had been at 0.56 (Fig. 41). At 0.45 (Fig. 43, $\beta_{lm} = 75^\circ$) the impact of negative incidence stall was seen over the entire span. Likewise at 0.42 (Fig. 44, $\beta_{lm} = 85^\circ$) the severe pressure surface leading edge overspeed predicted by the analysis was not at all evident in the data. Rather, the data showed a long separation bubble extending back to about 60 percent axial chord at midspan. The more extreme nature of the leading edge overspeed predicted at the tip relative to that predicted at the root was due to the much larger incidence variation at the tip relative to that at the hub (Fig. 36). It was interesting to note that as the inlet angle was increased (and also the rotor convergence ratio) the agreement between the measured and computed results on the suction surface near the hub (at 6.25 percent span) was improved. At 85° the area of poorest agreement on the suction surface was at the tip (98 percent span) and aft of the throat.

3. Radial Flow Analysis

Radial flows are of concern to the turbine designer for a number of reasons. The assumption of strip-theory is at the heart of many design analyses and the degree to which it is violated can influence many aspects of the turbine design. Radial flows, for example, will cause a spanwise redistribution of total pressure loss and total temperature. This greatly complicates the task of deducing spanwise performance, or efficiency, distributions.

It was demonstrated above that strong radial flows can occur on the pressure surface of a turbine rotor blade and that they have a powerful impact on the trajectory of film cooling air discharged there (Ref. 25). In a previous study (Ref. 26) it was demonstrated that the source of the radial flow on this rotor blade was not significantly related to any of the following mechanisms: centrifugal pumping of the blade boundary layer, leakage over the unshrouded blade tip, or secondary flow in the blade-to-blade channel. It was suggested that the most likely source of the radial flow was the three-dimensional inviscid flow over the airfoil.

Subsequent testing of a compressor rotor (Ref. 36) had demonstrated the presence of the "relative eddy" (Ref. 37) in the flow downstream of that rotor. It will be demonstrated in the following paragraphs that prior to separation, the radial flow on the turbine rotor pressure surface (Figs. 28 through 31) was primarily due to the relative eddy, a three-dimensional inviscid mechanism.

The axial component of relative vorticity was expressed in terms of the relative velocity components as follows.

$$\zeta_x = \frac{1}{r} \left[r \left(\frac{\partial W_\theta}{\partial r} \right) + W_\theta - \left(\frac{\partial W_r}{\partial \theta} \right) \right] \quad (1)$$

A convenient location in the rotor blade channel at which to examine this expression was at the axial plane where W_θ and its radial derivative are small. For the particular rotor airfoil of the present program and in Refs. 25 and 26, shown in Figs. 1 and 26, this occurred at the plane 30% of the way from the leading edge to the trailing edge at midspan (Fig. 45). At this axial location (and only at this axial location) W_θ was very small and the local velocity vectors were close to axial. This was true across the entire blade channel and from hub to tip since the maximum blade heights on both the suction and pressure surfaces occurred close to the 30% chord location (see Figs. 26 and 45). At this plane, since W_θ and its radial derivative were small the following approximation was made.

$$\zeta_x \approx - \frac{1}{r} \left(\frac{\partial W_r}{\partial \theta} \right)$$

This was integrated across the blade-to-blade channel to yield

$$(W_r/U)_p - (W_r/U)_s = - \int_{\theta_s}^{\theta_p} (\zeta_x / \Omega) d\theta \quad (2)$$

Strictly speaking, this was only true near midspan on a relatively high aspect ratio airfoil where hub and tip effects were not important. It was now necessary to determine the distribution of relative vorticity across the rotor blade channel, i.e. $\zeta_x(\theta)$.

The relative vorticity was related to the absolute vorticity as follows.

$$\vec{\zeta} = \nabla \times \vec{W} = \nabla \times (\vec{C} - \vec{U}) = \vec{\omega} - 2\vec{\Omega} \quad (3)$$

Hawthorne (Ref. 38) had shown that for the flow through an axial turbomachine (where the axial and circumferential gradients are zero in the axial region between blade rows) the streamwise growth of the streamwise component of absolute vorticity is given by the following expression (Ref. 38, Eq. 54).

$$\begin{aligned} \frac{\partial}{\partial s} \left(\frac{\omega_s}{\rho W} \right) = & \left(\frac{2}{\rho W^2 R_h} \right) \left\{ (H_T - UC_\theta + \frac{1}{2} U^2) \frac{\partial \ln P_T}{\partial r} \frac{r-1}{Y} \right. \\ & + (UC_\theta - \frac{1}{2} U^2) \frac{\partial \ln T_T}{\partial r} \\ & \left. - \left(\frac{\partial UC_\theta}{\partial r} \right) \right\}_1 \end{aligned} \quad (4)$$

R_n was the geodesic curvature of the relative streamline passing through the rotor blade channel. The term in braces was evaluated at the rotor inlet (Station 1) where axial and circumferential gradients are assumed to be negligible. This was the "small disturbance, large turning" case and the rotation of Bernoulli surfaces was neglected.

For uniform density flow this reduced to the following.

$$\frac{\partial}{\partial s} \left(\frac{\omega_s}{W} \right) = \left(\frac{2}{\rho W^2 R_n} \right) \left(\frac{\partial P_{T, \text{rot}}}{\partial r} \right)_1 \quad (5)$$

where $P_{T, \text{rot}}$ is the "rotary total pressure". If the flow entering the turbine stage had a uniform total pressure and if the stator total pressure loss was constant with span then -

$$\left(\frac{\partial P_{T, \text{rot}}}{\partial r} \right)_1 = - \rho \left(\frac{\partial UC_\theta}{\partial r} \right)$$

and from Eq. 5

$$\begin{aligned} \frac{\partial}{\partial s} \left(\frac{\omega_s}{W} \right) &= - \left(\frac{2}{W^2 R_n} \right) \left(\frac{\partial UC_\theta}{\partial r} \right) \\ &= - \left(\frac{2 \Omega C_x}{W^2 R_n} \right) K_1 \end{aligned} \quad (6)$$

where

$$K_1 = \left(\frac{1}{C_x} \frac{\partial (r C_\theta)}{\partial r} \right)_1 \quad (7)$$

Note that the parameter K_1 depended only on the stator and that it was independent of the rotor speed. Equation (6) was integrated along streamlines to arrive at the following expression.

$$\left(\frac{\omega_s}{\Omega} \right)_2 = \left(\frac{W_2}{W_1} \right) \left\{ \left(\frac{\omega_s}{\Omega} \right)_1 - 2K_1 \sin \beta \int_1^2 \left(\frac{W}{W_1} \right)^{-2} d\sigma \right\} \quad (8)$$

where σ was the local streamline turning, given by

$$d\sigma = \left(\frac{ds}{R_n} \right)$$

The integral in Eq. 8 was from station 1 upstream of the rotor to station 2 within the rotor channel. The streamwise component of vorticity in the flow approaching the rotor was expressed as follows.

$$\left(\frac{\omega_s}{\Omega_1}\right) = K_2 \left(\frac{C_x}{U}\right) \cos(\beta_1 - \alpha_\omega) \quad (9)$$

where

$$K_2 = \left(\frac{\omega_1}{\Omega}\right) / \left(\frac{C_x}{U}\right) = \left(\frac{r}{C_x} \cdot \omega_1\right)$$

α_ω was the angle of the absolute vorticity vector (from tangential) and $(\beta_1 - \alpha_\omega)$ was the angle between the absolute vorticity vector and the relative velocity vector at the rotor inlet. Note that K_2 depended only on the stator and that it was independent of the rotor speed.

If station 2 was taken to be the axial location in the blade channel where the local flow vectors are nearly axial, i.e. at the 30% chord location for the blade in Fig. 45, then the streamwise direction was the axial direction and equations 3, 8, and 9 were combined to give

$$\left(\zeta_x/\omega\right) = -2 + \left(\frac{W_2}{W_1}\right) \left\{ \left[K_2 \frac{C_x}{U} \cos(\beta_1 - \alpha_\omega) \right] - \left[2 K_1 \sin \beta_1 \int_1^2 \left(\frac{W}{W_1}\right)^{-2} d\sigma \right] \right\} \quad (10)$$

The first term (-2) was due to the rotating frame of reference. The first term in the braces was the component of absolute vorticity in the relative velocity direction at the rotor inlet. The second term in the braces was the generation of streamwise absolute vorticity due to turning of the flow.

This distribution of relative vorticity was integrated across the channel (in the plane at the 30% chord location) according to Eq. (2) to give the gapwise variation of radial velocity between adjacent rotor blades. The fact that there could be no net radial in- or out-flow required that the gap averaged value of W_r be zero. This established the magnitude of the radial velocity on the suction and pressure surfaces.

For free vortex flow at the rotor inlet both K_1 and K_2 are identically zero. This approximation was reasonably accurate for the present test since,

as shown in Fig. 35, the inlet relative total pressure corresponded very closely to a radially constant rotary total pressure (Eq. 5). Under this condition the radial velocity in the blade channel came about purely due to the rotating frame of reference relative eddy. Equation (10) then reduced to

$$(\zeta_x/\Omega) = -2$$

and Equation 2 could be integrated to give

$$(W_r/U)_p - (W_r/U)_s = -2 (\theta_p - \theta_s)$$

The blade channel shown in Fig. 45 had a $(\theta_p - \theta_s)$ of 0.17 radians. Thus, the radial velocity (W_r/U) varied from -0.17 on the suction surface to +0.17 on the pressure surface at the 30% chord location as shown in Fig. 46. Also plotted in this figure was the gapwise variation of the axial component of velocity (W_x/U) at the 30% chord location. This was based on a blade-to-blade potential flow analysis (Ref. 27) which very closely matched the measured blade pressure distribution (Figs. 37 through 41). The gapwise pitch angle distribution based on these radial and axial velocity components was also shown in the figure. On the suction surface, the high value of W_x resulted in a small pitch angle (-4.4°) toward the hub. On the pressure surface, however, the low value of W_x resulted in a large pitch angle ($+25.5^\circ$) toward the tip.

As the flow coefficient (C_x/U) of the turbine stage was changed the rotor incidence changed and this changed the rotor pressure distribution (Fig. 37). The calculation described above for free vortex flow at the rotor inlet was carried out over a range of rotor inlet angle. The results were shown in Figure 47. There was a gradual increase in the radial out-flow angle on the pressure surface and in the radial in-flow angle on the suction surface with increasing rotor inlet angle (i.e., with higher rotor speed). These changes were due to changes in the airfoil pressure distribution, i.e. changes in (W_x/U) . (W_r/U) was independent of flow coefficient for this free vortex case. Parenthetically, it was observed that at the largest inlet angles, i.e. at large negative incidence, the assumption of axial flow at the 30% chord location was beginning to break down.

For controlled vortex (non-free vortex) flow at the rotor inlet, both K_1 and K_2 had to be included in the calculation of the relative vorticity (Eq. 10). The through-flow design of this stage had been slightly non-free vortex in nature. This design calculation was used to determine the values of K_1 and K_2 which were used in the solution of Eq. (10). For this design the vane produced an absolute vorticity (K_2) of 1.74 oriented at an angle (α_w) of 26.6° from tangential (in the wheel speed direction). The value of K_1 for this design was 0.78.

The parameter K_1 was related to the radial variation of rotary total pressure as follows (from Eq. 7 with P_T constant).

$$\left(\frac{\partial P_{T,rot}}{\partial r} \right) = -\rho \Omega C_x K_1 \quad (11)$$

Experimental evidence based on a circumferential traverse in the stationary frame of reference in the axial gap between the stator and the rotor indicated that K_1 was approximately 70% of its design value. This estimate was based on relating the radial derivative of rC_θ required in Eq. 7 to the measured circumferential derivative of C_r assuming that the flow between the stator wakes was irrotational. The non-zero radial gradient of $P_{T,rot}$ that this implied was within the uncertainty of the deduced values of $P_{T,rel}$ in Fig. 35. This gradient would have decreased $C_{PT,rel}$ by 0.09 at the root and increased it by 0.09 at the tip (varying linearly in between).

Equation (10) was employed to give the gapwise distribution of the axial component of relative vorticity at the 30% chord plane, using the design values of K_1 and K_2 and using the analysis of Ref. 27 to provide the velocity field and streamline information necessary to evaluate the integral. This distribution of (ζ_x/Ω) was integrated across the channel (according to Eq. 2) to give the gapwise distribution of radial velocity. The gap averaged radial velocity was again set to zero to satisfy continuity. The resulting distribution of the radial flow angle was shown in Fig. 46. In comparing the controlled vortex and free vortex radial angle distributions it should be noted that for this design the two terms inside the braces in Eq. (10) are of opposite sign. The streamwise component of the rotor inlet absolute vorticity was in the streamwise direction for this design. Thus, the first term (involving K_2) had a positive contribution to ζ_x . It tended to produce negative radial velocity on the rotor pressure surface (i.e. toward the hub). The streamwise component of secondary vorticity that was generated within the channel, for this design, had a negative contribution to ζ_x . This occurred since K_1 was positive (a radially decreasing $P_{T,rot}$) and the integral in Eq. (10) was generally positive. Thus, the second term in the braces tended to produce a positive radial velocity on the pressure surface. Considering the effect of a positive K_1 in another way, low rotary total pressure fluid at the tip would be carried toward the suction surface by secondary flow. This would produce a positive radial velocity on the rotor pressure surface and a negative one on the blade suction surface. In summary, for this stage design, the two terms inside the braces in Eq. (10) tended to cancel causing the dominant influence to be the "-2" due to the rotating frame of reference.

The major deviation between the controlled vortex and the free vortex radial angle profiles was near the blade surfaces (Fig. 46). This was seen in Fig. 47 where results were shown for a range of rotor inlet angles. The effect of the slightly non-free vortex nature of the flow was to reduce the already small radial inflow angle on the suction surface and to increase slightly the radial out-flow angle on the pressure surface.

The major uncertainty areas of this analysis were: (1) the distortion of the absolute vorticity, i.e. Bernoulli surface rotation in the blade channel, (2) the approximation of W_θ being small at the 30% chord location, (3) the approximate nature of the solution of Eq. 1 and (4) other three-dimensional inviscid effects due to the radial variations of blade geometry (Fig. 26). The arguments given above were not valid close to the hub or the tip. The flow near the hub was influenced by the higher pressure surface velocity there which greatly reduced the radial flow angle (Fig. 29). The flow close to the tip was influenced by leakage flow over the blade tip (Fig. 29). As the flow speed on the pressure surface increased as the flow accelerated toward the blade trailing edge, the pitch angle also dropped. This was seen in the flow visualization results of Fig. 29.

The large region of relatively low velocity fluid adjacent to the pressure surface experienced the strongest radial displacement due to this mechanism. Thus, in addition to producing a radial component to the trajectory of any pressure surface film cooling air (Ref. 25), this flow mechanism would also produce a significant radial redistribution of fluid from the rotor inlet to the rotor exit. Specifically, one would expect this mechanism to cause considerable attenuation to the radial profile of total temperature as the flow passed through the rotor.

From the point of view of the designer the main concern is what control he can exercise over this mechanism. There are at least three ways in which the turbine designer can reflect the presence of the relative eddy. First, its strength could, to some extent, be influenced by the degree of "non-free vortex" flow in his through-flow design. Second, for a given strength of the relative eddy, i.e. for a given relative vorticity, the radial displacement (pitch angle) on the pressure surface could be reduced by increasing the pressure surface flow velocity. Finally, for a given radial displacement, film coolant blowing sites could be positioned in order to compensate for the radial component of the coolant trajectory.

4. Potential Flow Modeling of Separation Bubbles

The powerful impact that negative incidence stall could have on the rotor pressure distribution was seen in the midspan data in Fig. 37 and in the fullspan data in Fig. 44. The pressure surface stall bubble had its origin in the inability of the boundary layer to negotiate the severe recompression of the leading edge over-speed. The effect of the stall was to greatly reduce the depth of the over-speed (from a C_p of 0.3 to 0.6 at $\beta_{lm} = 85^\circ$) and to greatly increase the distance over which recompression occurred. The bubble was seen to close at about 60% chord in both the flow visualization (Fig. 34) and in the pressure distribution (Fig. 44).

In an attempt to estimate the size and shape of the stall bubble at midspan and at 85° two approaches were explored: (1) modeling the bubble by changing the airfoil pressure surface contour and (2) modeling the bubble by mass addition and removal along the pressure surface. The results of the first approach are illustrated in Figs. 48 and 49. The actual airfoil contour and the hypothetical contour used to model the pressure surface bubble are shown in Fig. 48. The hypothetical contour was arrived at by adjusting the pressure surface contour until reasonably close agreement had been obtained with the measured data. The measured data and the computed results for the actual and hypothetical contours are shown in Fig. 49. The hypothetical contour provided an excellent match between the measured and computed results along the entire pressure surface and also along the suction surface. The increased blockage due to the bubble had caused higher velocities (lower pressure) not only on the pressure surface but also on the suction surface.

There was a feature of this comparison which, however, was not totally defensible. The measured data and the computed results for the actual contour represented pressures along the actual contour. For the hypothetical contour the computed results represented pressures along the bubble displacement surface (i.e. on the hypothetical contour) which were not necessarily the same as those on the actual contour.

In the second approach to modeling the size and shape of the stall bubble a distribution of the normal velocity component was specified along the pressure surface. Here again the distribution of normal velocity was adjusted until reasonably close agreement had been obtained with the measured pressure data. The distribution of positive and negative normal velocity was specified in such a way that there was no net addition of mass to the flow. The measured results and the computed results both with and without blowing on the pressure surface are shown in Fig. 50. Also shown is the distribution of normal velocity. The results are much the same as in Fig. 49 but in the present case both the measured and computed results are on the actual airfoil contour. The pressure distribution in the fluid along the dividing stream line between the fluid in the separation bubble and the mainstream flow over it is also shown in Fig. 50. As can be seen the differences between the pressure on the surface and along this dividing streamline are substantial. The dividing streamline is shown in Fig. 51. It is similar to the hypothetical contour shown in Fig. 4 but local differences here are also substantial.

IV. CONCLUSIONS

An extensive body of experimental data and analytical results for an axial turbine stage have been presented which provide detailed information on (1) the nature of the unsteadiness in the midspan flow over the rotor and the stator due to rotor-stator interaction, (2) the impact of this unsteadiness on the stator midspan time averaged heat transfer and (3) the fullspan nature of the flow over the rotor with particular attention given to the relative eddy and negative incidence stall. Specific conclusions in each of these areas were as follows.

Rotor-Stator Aerodynamic Interaction

1. The stator midspan time averaged pressure distribution was in agreement with potential flow and it was independent of rotor speed and only a very weak function of rotor-stator axial gap.
2. The rotor midspan time averaged pressure distribution was in excellent agreement with potential flow over a wide range of incidence and it was only a weak function of rotor-stator axial gap.
3. The unsteady pressures on the stator at the 15% gap were as high as $\pm 15\%$ of the dynamic pressure with waves propagating both upstream and downstream on the suction surface.
4. The unsteady pressures on the rotor leading edge at the 15% gap were as high as $\pm 80\%$ of the incident relative dynamic pressure.
5. Unsteady stator trailing edge loading was observed to occur at the reduced frequencies present in this experiment ($k = 1.9$ to 2.7) and it is probably a required feature in any analytical model of rotor-stator interaction.
6. The variation of the fluctuating pressure on the stator with axial gap was well predicted by a steady rotor potential flow calculation.
7. The fluctuating pressure on the rotor was of a much larger amplitude than could be explained by the stator potential flow alone and its decay with increased axial gap was similar to that of wake decay ($\propto X^{-1/2}$).
8. The high response pressure transducers at the stator trailing edge gave evidence of a Karman vortex street at a Strouhal number of 0.21 based on trailing edge diameter.
9. The stator boundary layer (as evidenced by thin film gages) evolved from laminar, to transitional (with Tollmien-Schlichting waves), to turbulent, all with a periodic oscillation at rotor passing frequency.

10. The Tollmien-Schlichting waves were evident in the high response pressure transducer output.
11. The rotor suction surface boundary layer varied periodically between turbulent and laminar flow as it passed into and out of the stator wakes. This was particularly evident when the rotor was at negative incidence.
12. The instantaneous high or low pressures on the rotor suction surface occurred when the rotor was between or within the stator wakes respectively.
13. No evidence was found to indicate that either the stator or the rotor was experiencing periodic separation and reattachment due to rotor-stator interaction.

Unsteady Effects on Stator Heat Transfer (Stanton number)

1. At the 65% gap the stator suction surface Stanton number was initially at a laminar level, went through transition, and was at a turbulent level to the trailing edge.
2. At the 65% gap the laminar and turbulent suction surface Stanton number levels were in good agreement with a theoretical prediction.
3. At the 15% axial gap (on the suction surface) the same laminar, transitional and turbulent flow was observed but the Stanton number was higher by typically 25%.
4. At both axial gaps, the transition location on the suction surface, as indicated by the Stanton number distributions, was very close to that indicated by the thin film gages and by the high response pressure transducers.
5. The pressure surface Stanton number distributions indicated transitional flow along the entire surface at both axial gaps and a much smaller increase due to reduced axial gap.
6. The stator Stanton number distribution was only a very weak function of rotor speed.

Rotor Fullspan Aerodynamics

1. Strong radial out-flow was observed on the rotor pressure surface in the vicinity of design incidence.
2. It was demonstrated that the strong radial out-flow on the rotor pressure surface was due to the relative eddy and that its magnitude and variation with rotor incidence could be predicted.

3. Fullspan negative incidence stall occurred above an inlet angle of 55° and grew in extent to 60% of axial chord at 85° .
4. Strong radial flow existed within the stall bubble.
5. The rotor pressure distributions were in excellent agreement with potential flow from 12 1/2% span to 87 1/2% span, prior to negative incidence stall.
6. The rotor suction surface was influenced by the hub and tip secondary flow vortices but a major portion of it was covered by attached, nearly two-dimensional boundary layer flow.
7. Evidence of the secondary flow at the root was seen in the pressure distribution at 6.25% span and evidence of the secondary flow and the leakage flow at the tip was seen in the pressure distribution at 98% span.
8. At large negative incidence, due to the strong leading edge overspeed, tip leakage flow passed from the suction surface onto the tip.
9. A vena contracta was present on the unshrouded rotor tip as the leakage flow passed from the pressure surface, across the tip to the suction surface.
10. The effect of negative incidence stall on the rotor pressure distribution at midspan was accurately simulated by computing the pressure distribution for a hypothetical airfoil, that is, one with its pressure surface contour thickened to simulate the stall bubble.
11. The effect of negative incidence stall was also accurately simulated by computing the pressure distribution for an airfoil with a pressure surface distribution of blowing and suction used to simulate the stall bubble.

REFERENCES

1. Kemp, N. H. and W. R. Sears: Aerodynamic Interference Between Moving Blade Rows. *J. Aero. Sci.*, Vol. 20, n. 9, p. 585-597, September 1953.
2. Kemp, N. H. and W. R. Sears: The Unsteady Forces Due to Viscous Wakes in Turbomachines. *J. Aero. Sci.*, Vol. 22, n. 7, p. 478-483, July 1955.
3. Giesing, J. P.: Nonlinear Two-Dimensional Unsteady Potential Flow with Lift. *J. Aircraft*, Vol. 5, n. 2, p. 135-143, March-April 1968.
4. Giesing, J. P.: Nonlinear Interaction of Two Lifting Bodies in Arbitrary Unsteady Motion. *Trans. ASME, J. Basic Eng.*, p. 387-394, September 1968.
5. Parker, R.: Calculation of Flow Through Cascades of Blade Having Relative Motion and the Generation of Alternating Pressures and Forces Due to Interaction Effects. *Proc. Inst. Mech. Eng.*, Vol. 182, pt. 1, n. 11, p. 229-242, 1967-68.
6. Parker, R.: Pressure Fluctuations Due to Interaction Between Blade Rows in Axial Flow Compressors. *Proc. Inst. Mech. Eng.*, Vol. 183, pt. 1, n. 7, p. 154-164, (1968-69).
7. Parker, R.: Relation Between Blade Row Spacing and Potential Flow Interaction Effects in Turbomachines. *Proc. Inst. Mech. Eng.*, Vol. 184, pt. 3G (11), p. 1-8, (1969-70).
8. Parker, R. and J. F. Watson: Interaction Effects Between Blade Rows in Turbomachines. *Proc. Inst. Mech. Eng.*, Vol. 186, 21/72, (1972).
9. Gostelow, J. P.: Trailing Edge Flows Over Turbomachine Blades and the Kutta-Joukowski Condition. *ASME Paper No. 75-GT-94*, March 1975.
10. Satyanarayana, B. and S. Davis: Experimental Studies of Unsteady Trailing-Edge Conditions. *AIAA Journal*. Vol. 16, n. 2, p. 125-129, February 1978.
11. AGARD Conference Proceedings No. 177 on Unsteady Phenomena in Turbomachinery, 46th PEP Meeting, September 22-26, (1975).
12. Adachi, T. and Y. Murakami: Three-Dimensional Velocity Distribution between Stator Blades and Unsteady Force on a Blade due to Passing Wakes, *JSME*, Vol. 22, No. 170, August 1979, pp. 1074-1082.

REFERENCES (Cont'd)

13. Gallus, H. E., J. Lambertz and Th. Wallmann: Blade-Row Interaction in an Axial Flow Subsonic Compressor Stage. ASME, J. Eng. for Power, January 1980, Vol. 102 pp. 169-177.
14. Scholz, N.: Aerodynamics of Cascades. Translated and revised by A. Kline, AGARD-AG-220, pp. 341-344.
15. Evans, R. L.: Boundary Layer Development on an Axial-Flow Compressor Stator Blade, ASME, Jour. Eng. for Power, April 1978, vol. 100, n. 2 pp. 287-293.
16. Smith, L. H.: Casing Boundary Layers in Multistage Compressor, Flow Research in Blading, ed. L. S. Dzung, March 1969.
17. Mikolajczak, A. A.: The Practical Importance of Unsteady Flow, Paper No. 1 in Ref. 11.
18. Hetherington, R. and R. R. Moritz: Influence of Unsteady Flow Phenomena on the Design and Operation of Aero Engines, Paper No. 2 in Ref. 11.
19. Kosyak, Yu. F., S. P. Sobolev, Yu. E. Yushkovich, V. I. Golamn and P. S. Petrusenko: Selecting the Axial Clearances Between the Stages of a Turbine, Thermal Engineering, Vol. 3, p. 22 (Tepolenergetika, 1973 20 (3) 17-18), (1973).
20. Messegee, J.: Influence of Axial and Radial Clearances on the Performance of a Turbine stage with Blunt Edge Non-Twisted Blades. A. E. Thesis, U.S. Naval Postgraduate School, September 1967.
21. Due, H. F., A. E. Easterling and C. Rogo: Cascade Research on Small, Axial High-Work, Cooled Turbine. ASME Paper No. 75-GT-62, March 1975.
22. Okapuu, U.: Some Results From Tests on a High Work Axial Gas Generator Turbine, ASME Paper No. 74-GT-81, March 1974.
23. Blair, M. F. and M. J. Werle: The Influence of Free-Stream Turbulence on the Zero Pressure Gradient Fully Turbulent Boundary Layer, AFOSR Report No. September, 1980.
24. Dunn, M. G. and A. Hause: Measurements of Heat Flux and Pressure in a Turbine Stage, ASME Paper No. 81-GT-88, presented at the Gas Turbine Conf., Houston, TX, March 1981.

REFERENCES (Cont'd)

25. Dring, R. P., M. F. Blair and H. D. Joslyn: An Experimental Investigation of Film Cooling on a Turbine Rotor Blade, Trans. ASME, Jour. Eng. for Power, Vol. 102, No. 1, January 1980, pp. 81-87.
26. Dring, R. P. and H. D. Joslyn: Measurements of Turbine Rotor Blade Flows. Trans. ASME, Jour. Eng. for Power, Vol. 103, No. 2, April 1981, pp. 400-405.
27. Caspar, J. R., D. E. Hobbs and R. L. Davis: Calculation of Two-Dimensional Potential Cascade Flow Using Finite Area Methods, AIAA Journal, Vol. 18, NO. 1., Jan. 1980, pp. 103-109.
28. Roshko, A.: On the Development of Turbulent Wakes from Vortex Streets, NACA TR-1191, 1954, also presented by Schlichting, H.: Boundary Layer Theory, 6th ed, 1968, Fig. 2.9.
29. Lawaczeck, O. and H. J. Heinemann: Von Karman Vortex Streets in the Wakes of Subsonic and Transonic Cascades, AGARD-CP-177, Unsteady Phenomena in Turbomachinery, Paper No. 28, April 1976.
30. Schlichting, H.: Boundary Layer Theory, 6th ed., 1968.
31. Fink, M. R.: Prediction of Airfoil Tone Frequencies, J. Aircraft, Vol. 12, No. 2, Feb. 1975, pp. 118-120.
32. Erens, P. J. and V.A.L. Chasteau: Laminar Boundary-Layer Response to Free-stream Disturbances, AIAA Journal, Vol. 12, No. 1, Jan. 1974, pp. 93-94.
33. Graziani, R. A., M. F. Blair, J. R. Taylor and R. E. Mayle: An Experimental Study of Endwall and Airfoil Surface Heat Transfer in a Large Scale Turbine Blade Cascade, ASME. Jour. Eng. for Power, April 1980, Vol. 102, pp. 257-267.
34. Edwards, D. E., J. E. Carter and M. J. Werle: Analysis of the Boundary Layer Equations Including a New Composite Coordinate Transformation, UTRC Report No. UTRC81-30, 1981.
35. Langston, L. S., M. L. Nice and R. M. Hooper: Three-Dimensional Flow Within a Turbine Cascade Passage, ASME Jour. Eng. for Power, Vol. 99, No. 1, Jan. 1977, pp. 21-28.
36. Dring, R. P., H. D. Joslyn, and L. W. Hardin: An Investigation of Axial Compressor Rotor Aerodynamics, ASME Paper No. 81-GT-56, to be Published in the ASME Jour. Eng. for Power.

REFERENCES (Cont'd)

37. Lewis, R. I. and G. W. Fairbairn: Analysis of the Through-Flow Relative Eddy of Mixed-Flow Turbomachines, Int. J. Mech. Sci., Vol. 22, No.9, pp. 535-549, 1980.
38. Hawthorne, W. R.: Secondary Vorticity in Stratified Compressible Fluids in Rotating Systems. CUED/A-Turbo/TR 63, University of Cambridge, England, 1974.

APPENDIX

STATOR WAKE CHARACTERIZATION

The stator wake at midspan was documented in an effort to provide a basis for any future analytical efforts in the area of the gust response of the rotor. The wake documentation was accomplished using a 5-hole probe at midspan at a flow coefficient (C_x/U) of 0.78. The circumferential traverse was conducted at a plane 17% of the stator axial chord axially aft of the stator trailing edge. The traverse was by necessity conducted with the 65% rotor-stator axial gap. The wake shape was analyzed in the same manner as in Ref. 36, i.e. using a linear variation for the "inviscid" velocity across the wake to establish the "ideal" velocity at the wake center (V_c). The present wake profile shape was in excellent agreement with the Gaussian and polynomial profiles discussed in Ref. 36. The stator wake was summarized by the following parameters.

Y_2	=	0.036
δ_w/τ	=	0.045
δ^*/τ	=	0.0172
θ/τ	=	0.0149
H	=	1.154
$(V_c - V_m)/V_c$	=	0.182
$K' = \frac{\frac{V_c - V_m}{V_c}}{1 - \frac{1}{H}}$	=	1.358

Recall that the wake shape parameter (K') was 1.414 for a Gaussian profile, 1.40 for the polynomial profile in Ref. 36 and that it averaged out to 1.39 ± 0.06 for the sixteen mispan wake profiles of the compressor rotor reported in Ref. 36.

TABLE I

Airfoil Geometry and Nominal Operating Conditions, $(C_x/U) = 0.78$

Airfoil	Stator Vane	Rotor Blade
Number	22	28
B_x (ins)	5.93	6.34
(τ/B_x)	1.30	0.96
Span (ins)	6.00	6.00
(Span/B_x)	1.01	0.95
Inlet flow angle (deg.)	90.0	40.0
Exit flow angle (deg.)	22.5	25.5
$\text{Re}(B_x, C_2 \text{ or } W_2)$	5.9×10^5	5.5×10^5

 $C_x = 75 \text{ ft/sec } (\approx \text{Const})$ $N = 410 \text{ rpm } (\text{Variable})$

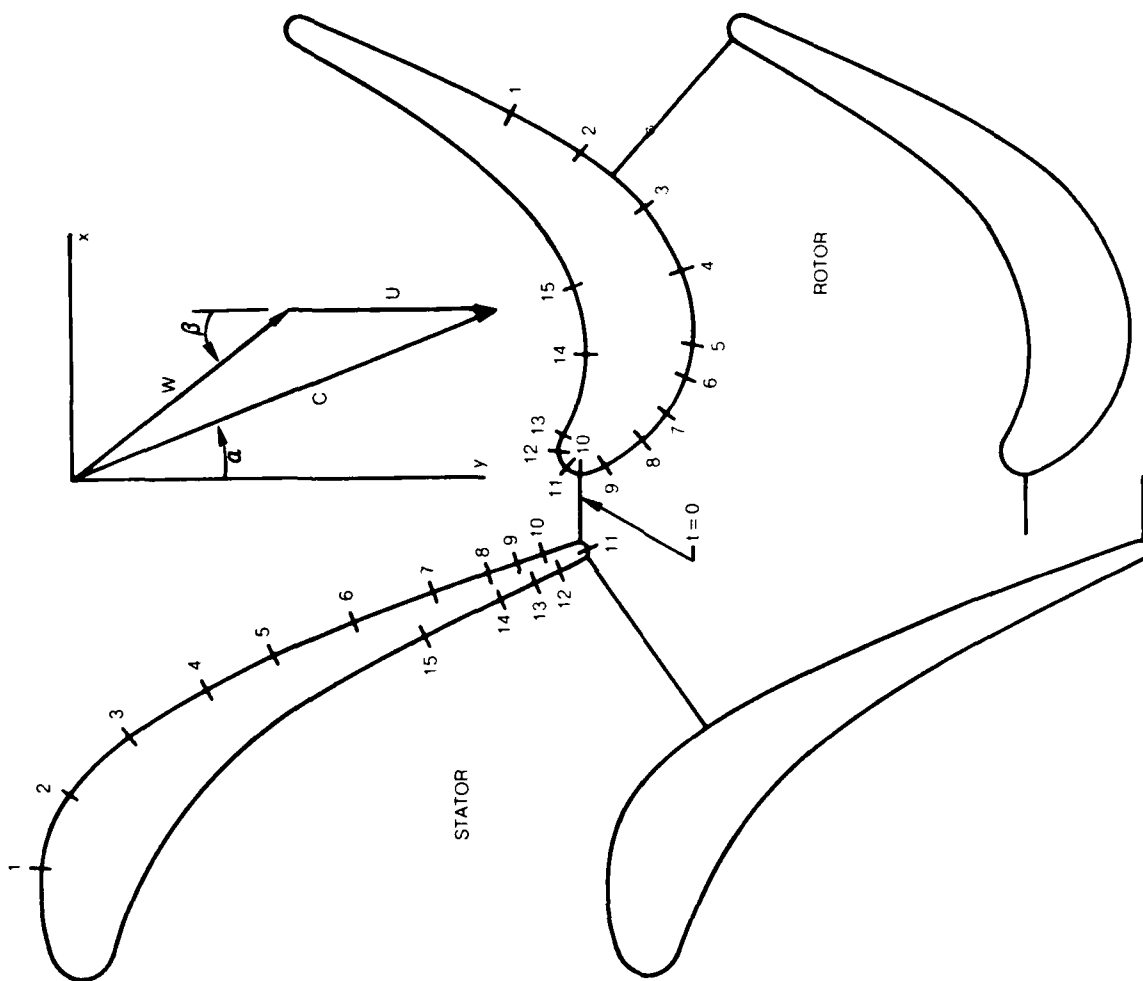
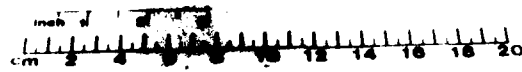


Fig. 1 Turbine Stage at 15% Gap (Kulite Sites)



7. SUCTION SURFACE



8. SUCTION SURFACE

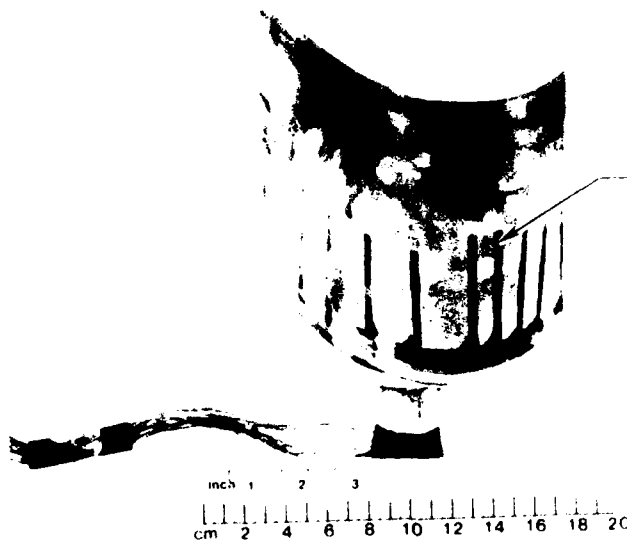


Fig. 1. (a) (b) (c) (d) (e) (f) (g) (h) (i) (j) (k) (l) (m) (n) (o) (p) (q) (r) (s) (t) (u) (v) (w) (x) (y) (z)

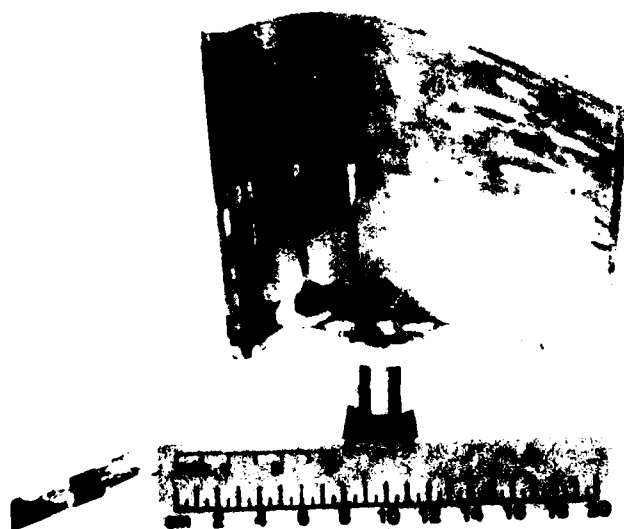
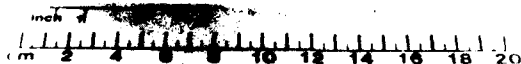
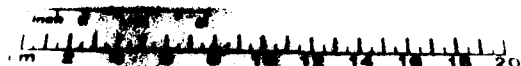
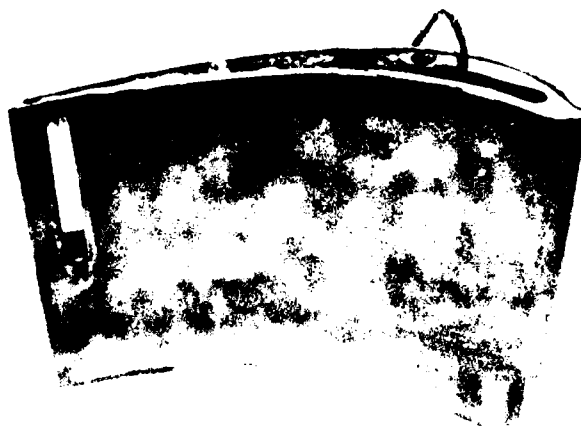


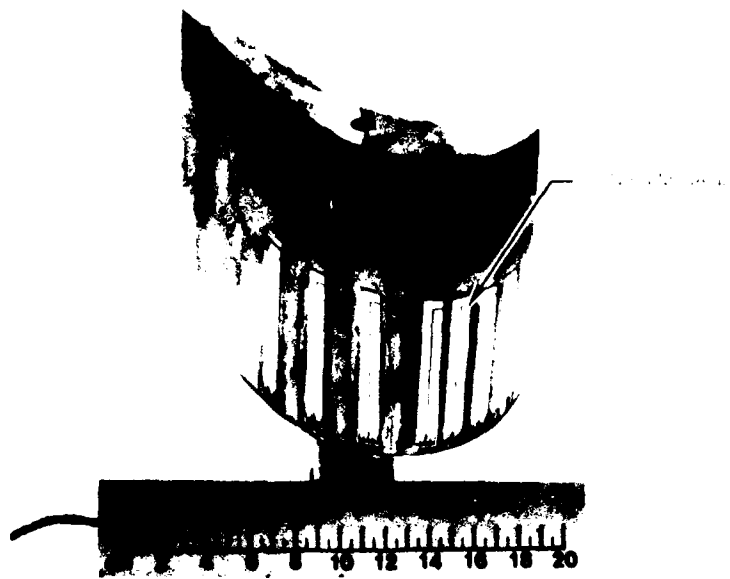
Fig. 2. (a) (b) (c) (d) (e) (f) (g) (h) (i) (j) (k) (l) (m) (n) (o) (p) (q) (r) (s) (t) (u) (v) (w) (x) (y) (z)



REDUCTION SURFACE



REDUCTION SURFACE



a SUCTION SURFACE



b PRESSURE MEASUREMENT

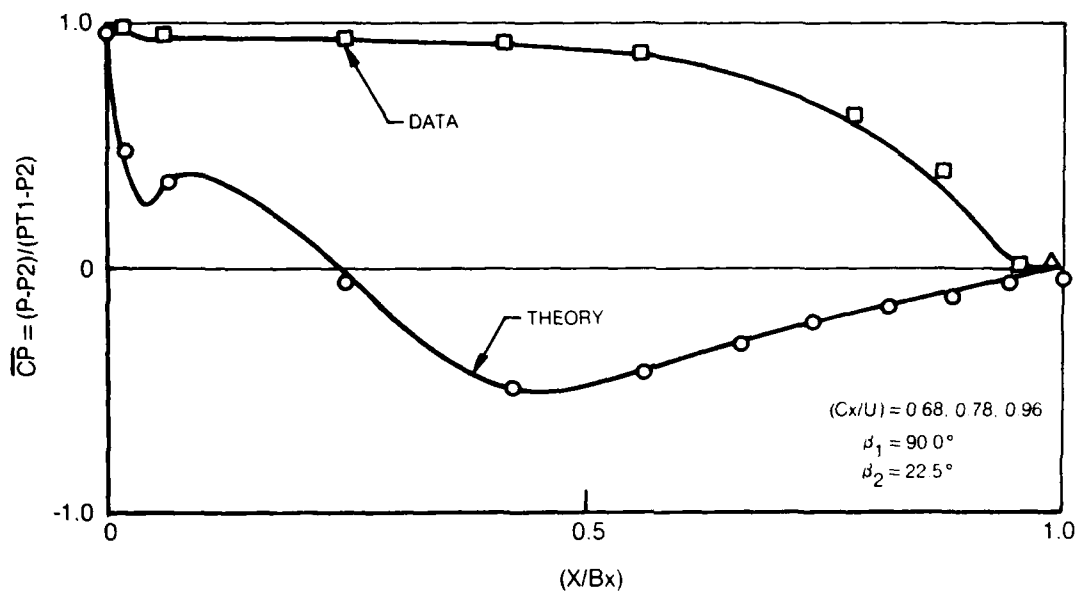


Fig. 6 Stator Pressure Distribution - Time Average

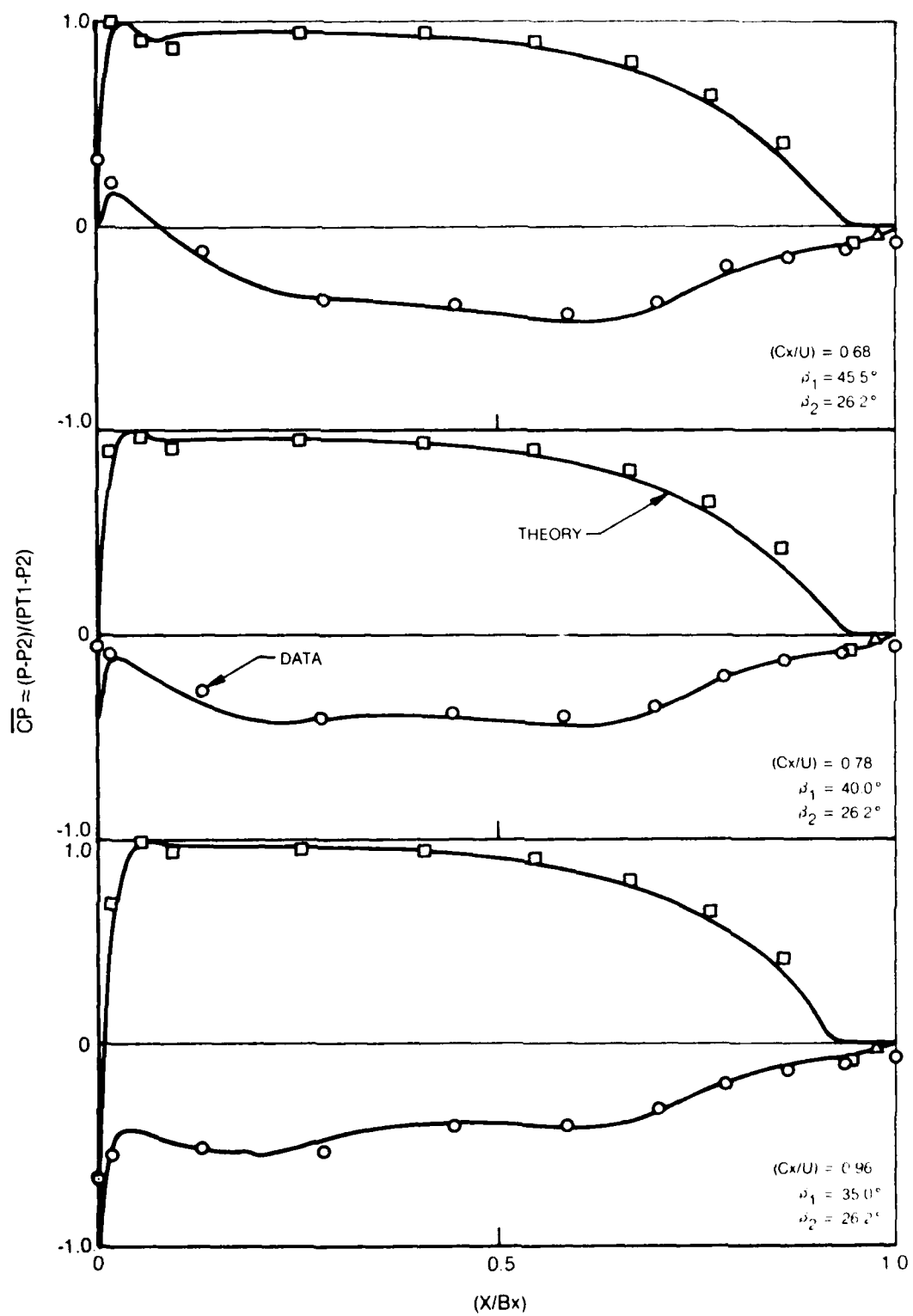


Fig. 7 Rotor Pressure Distributions - Time Average

81-4-88-7

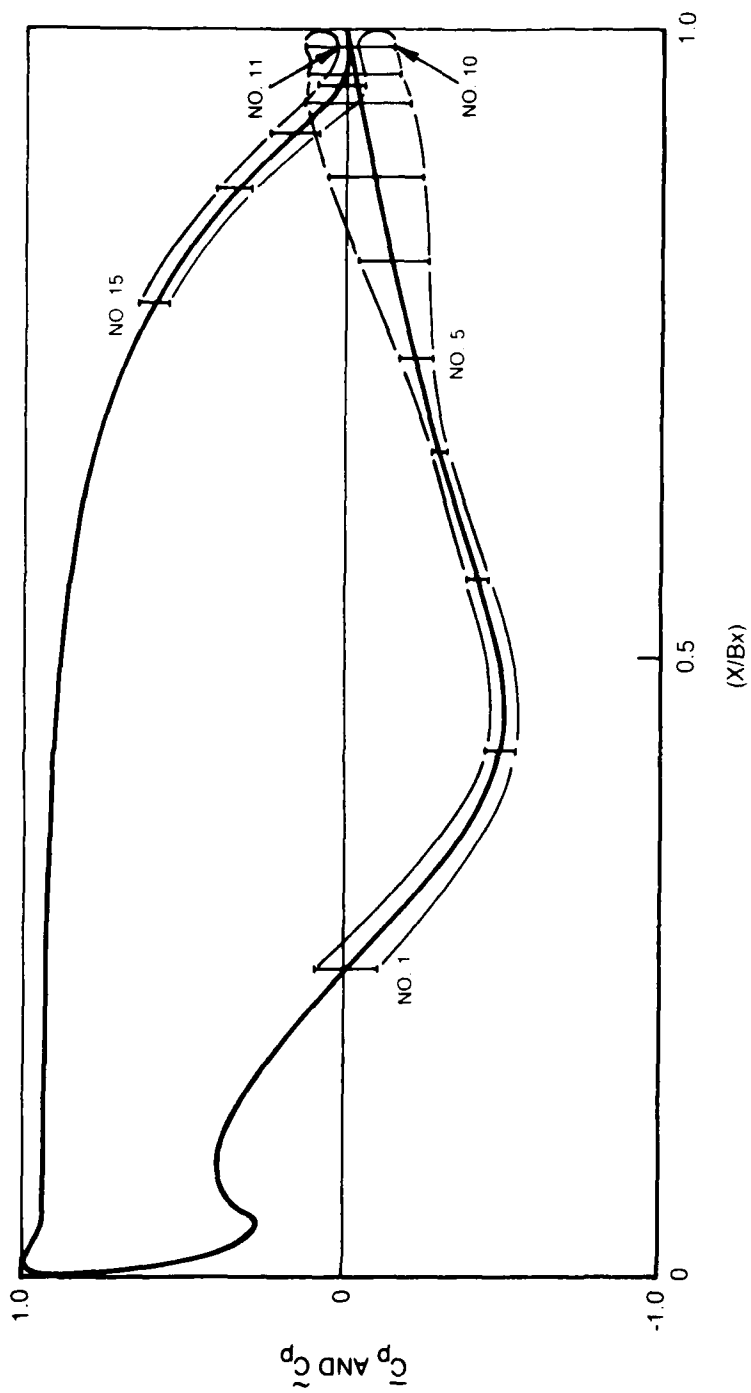


Fig. 8 Stator Unsteady Pressure Envelope, 15% Gap, $(C_x/U) = 0.78$

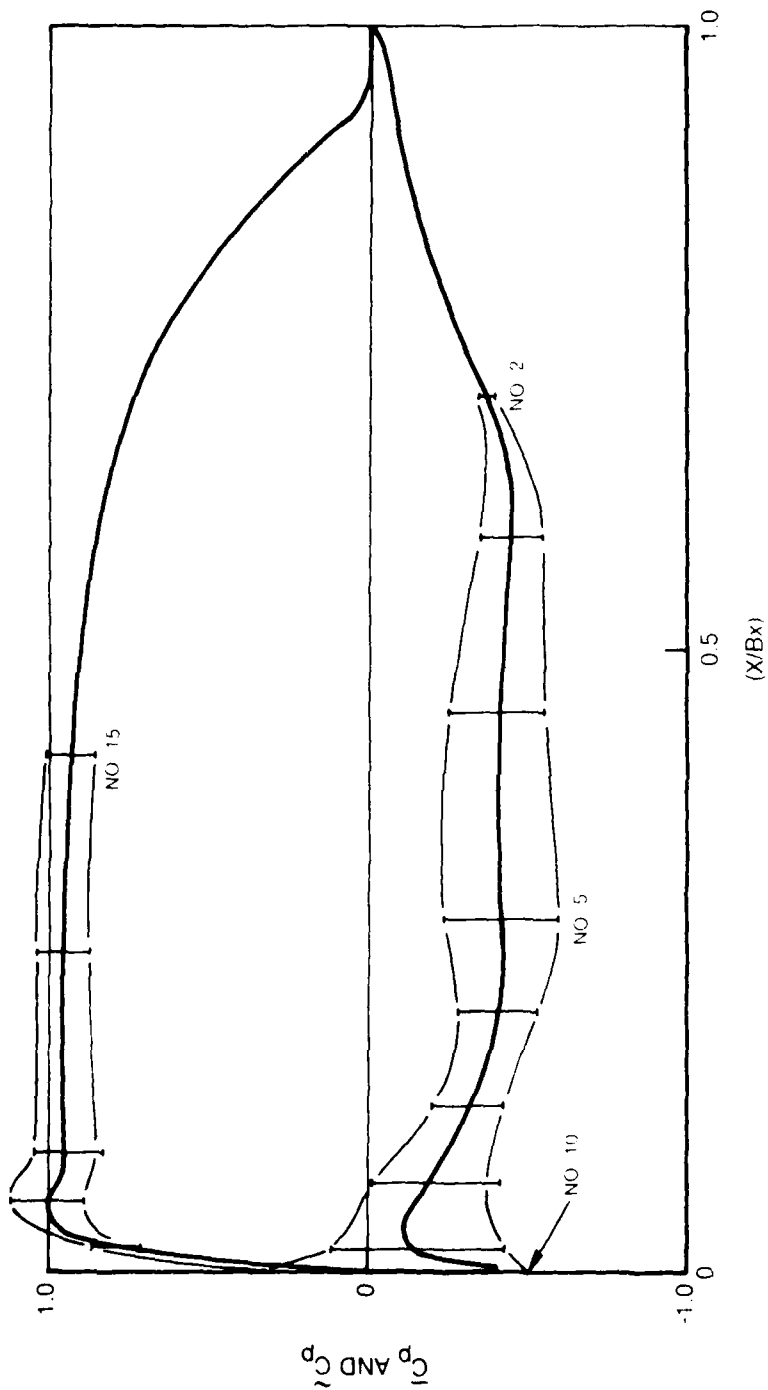


Fig. 9 Rotor Unsteady Pressure Envelope, 15% Gap, $(C_x/U) = 0.78$

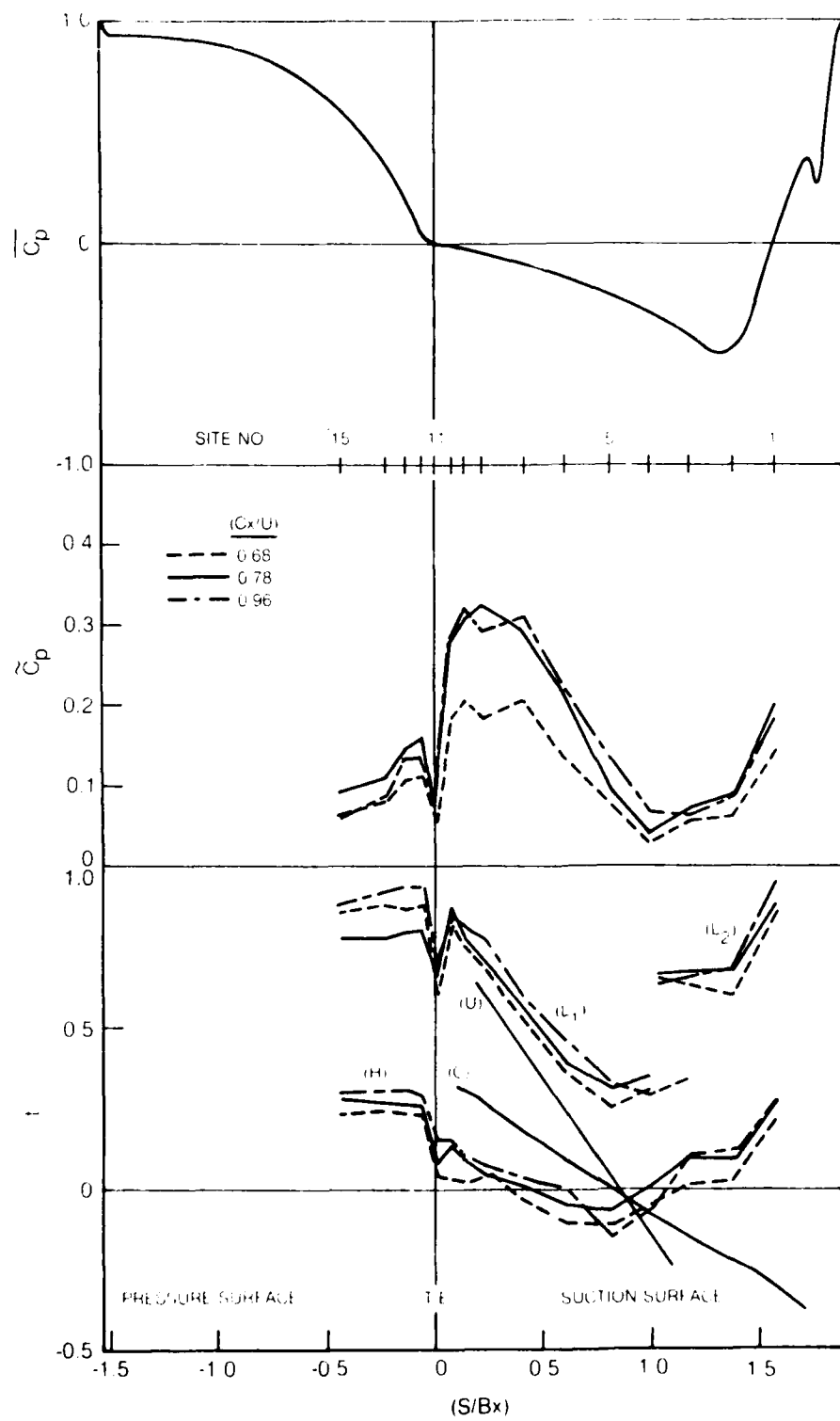


Fig. 10 Stator Unsteady Pressure, 15% Gap

81-4-88-10

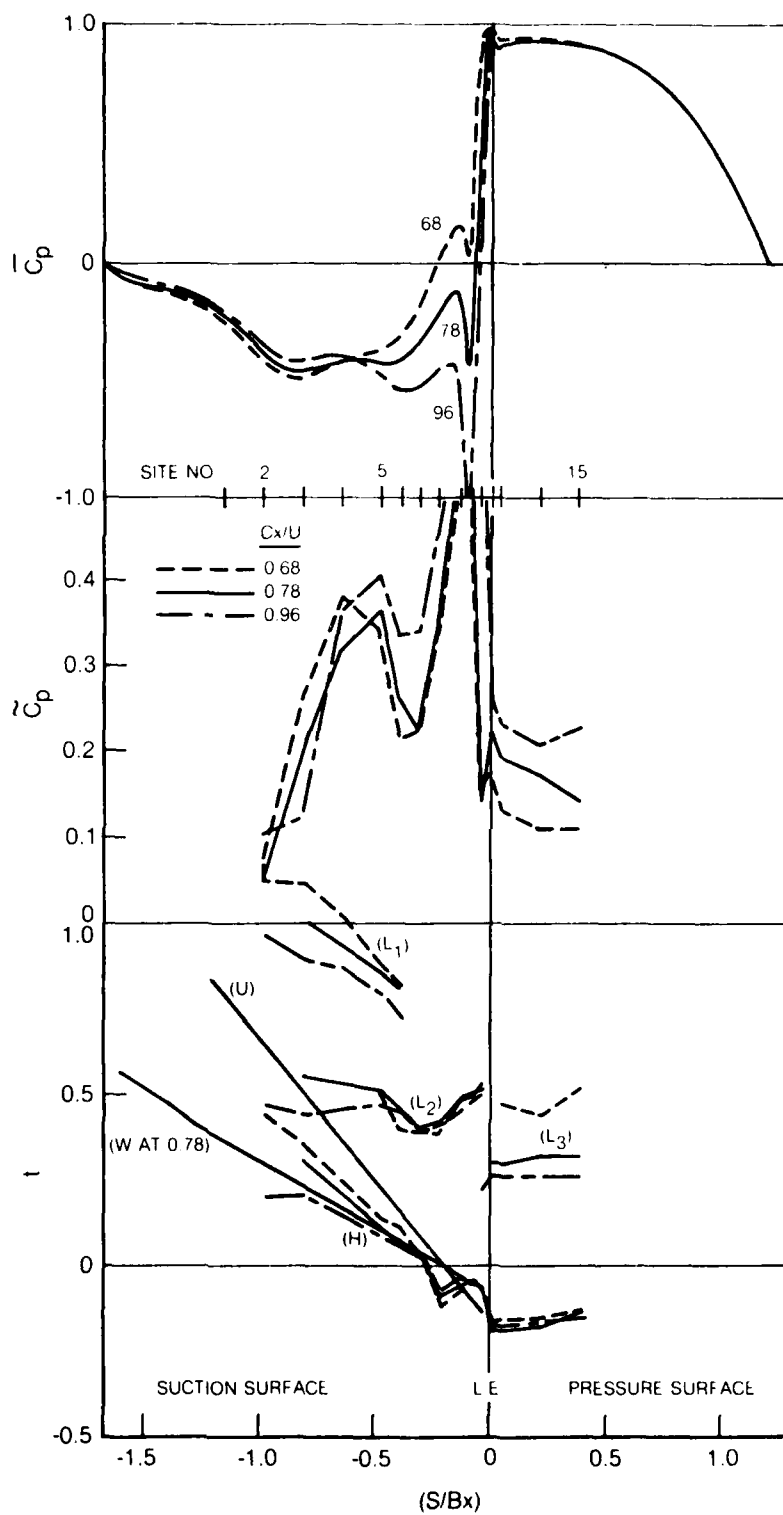


Fig. 11 Rotor Unsteady Pressure, 15% Gap

81-4-88-11

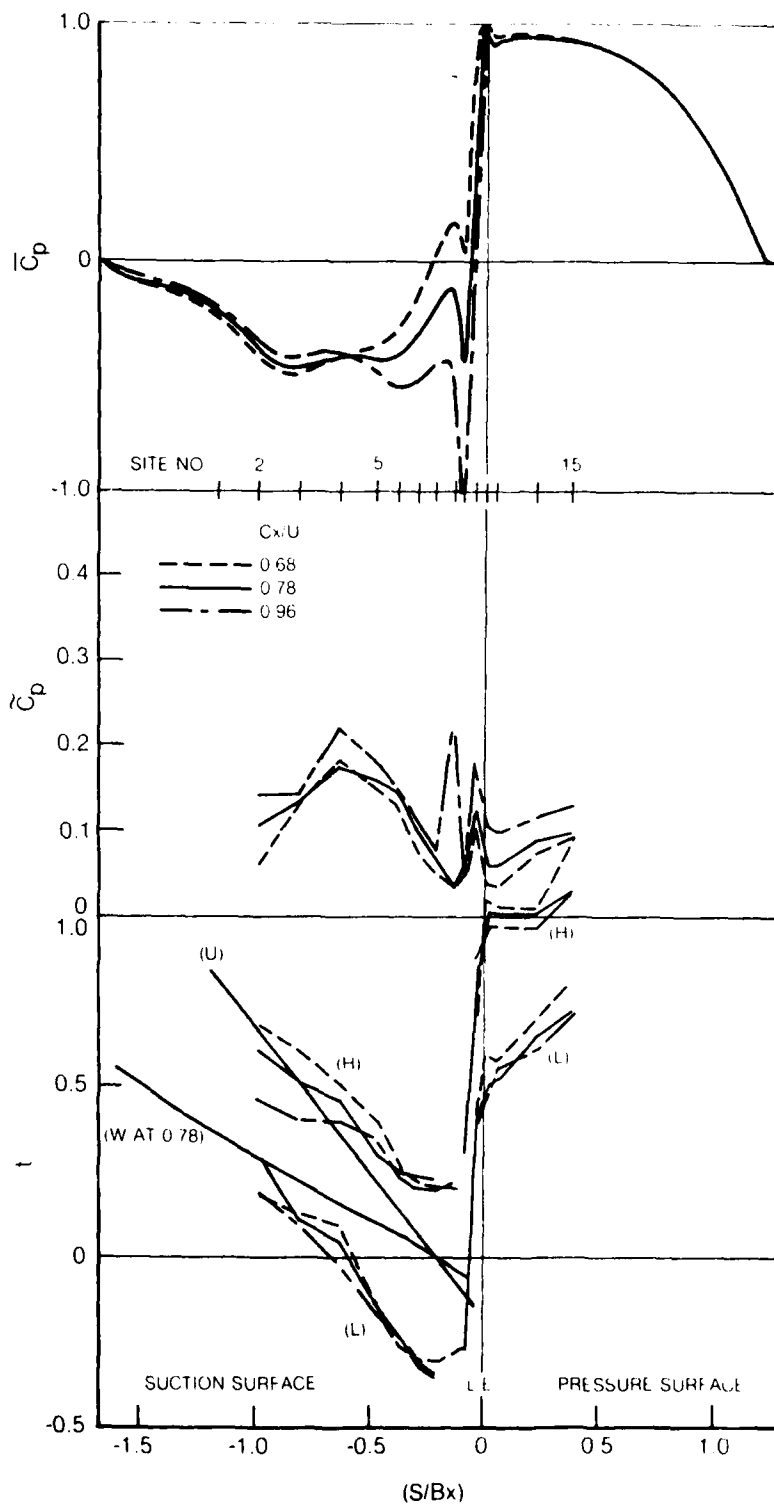


Fig. 12 Rotor Unsteady Pressure, 65% Gap

81-4-88-12

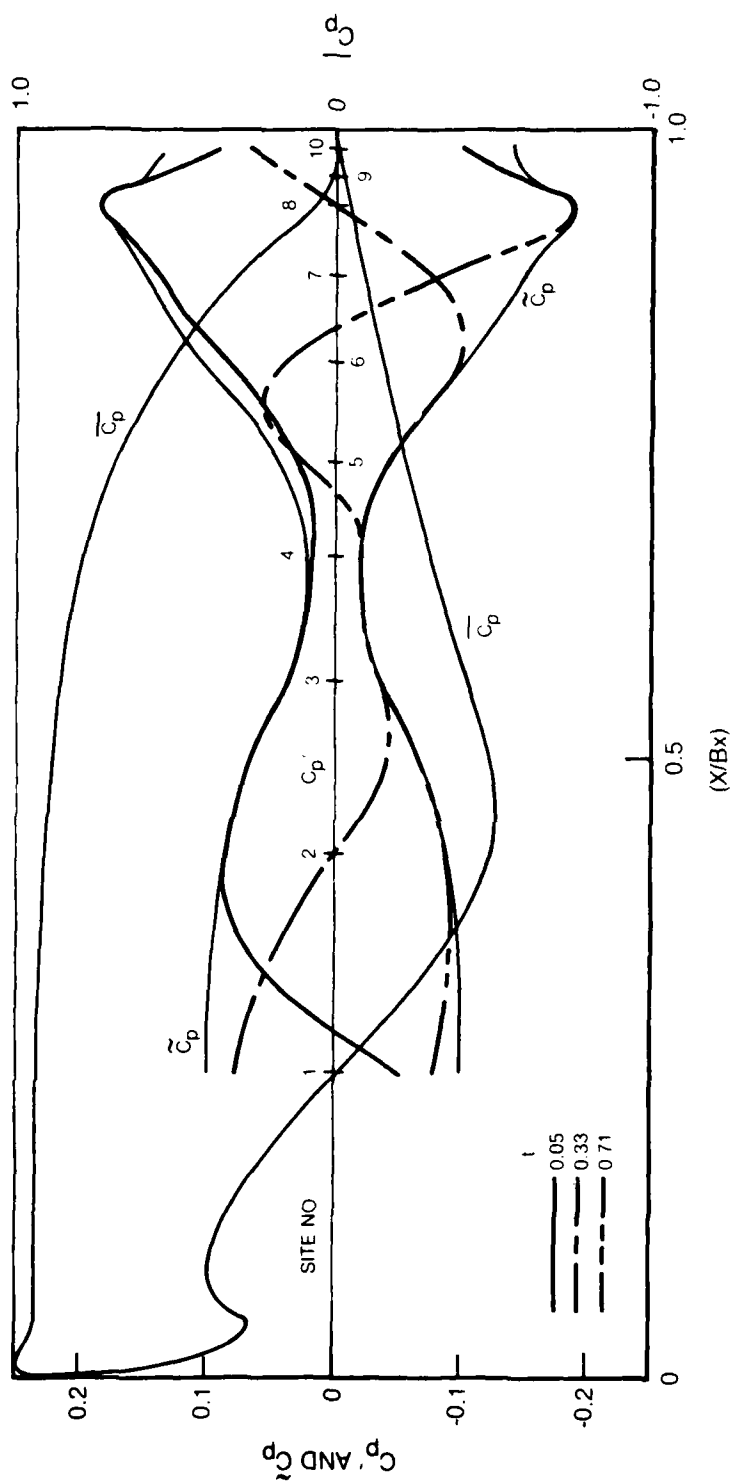


Fig. 13 Stator Instantaneous Pressure Distributions, 15% Gap,
 $(C_x/U) = 0.78$

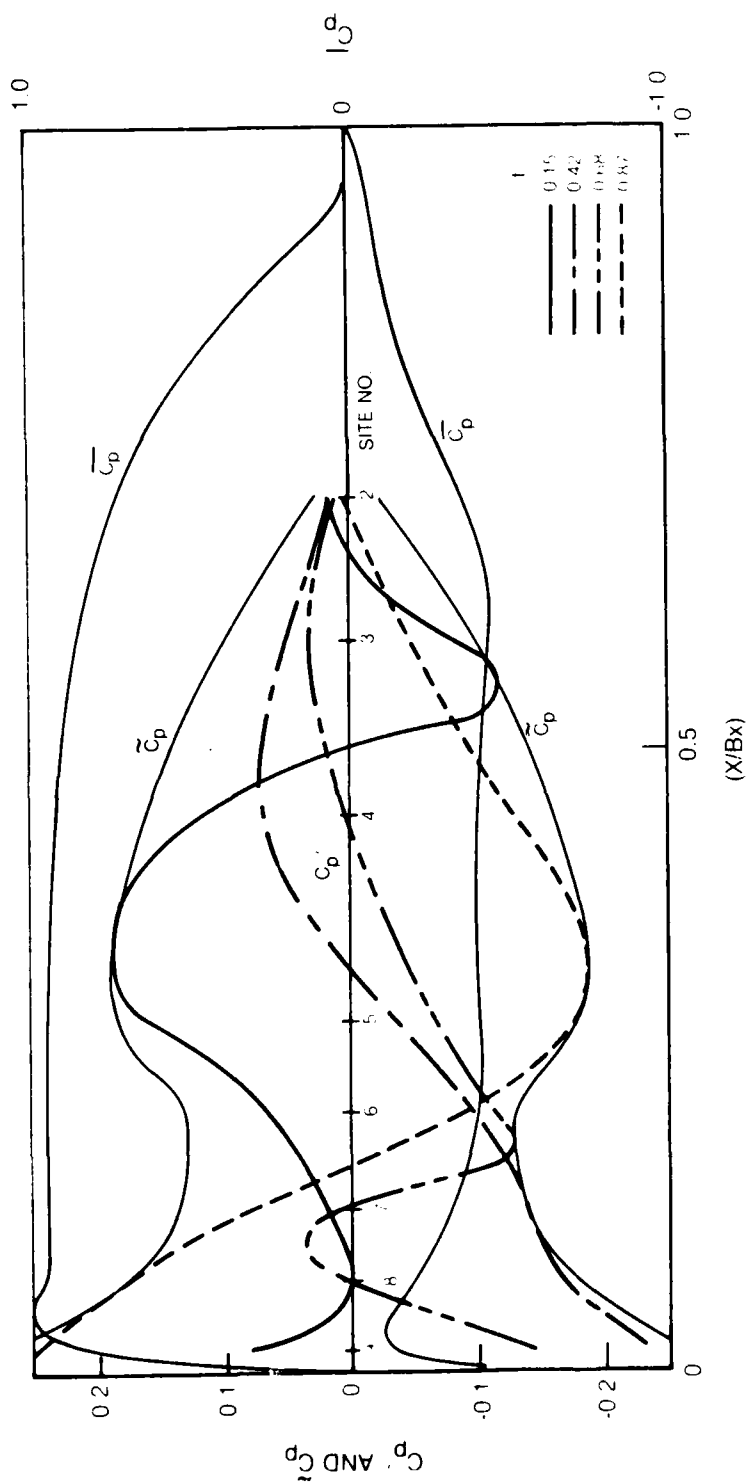


Fig. 14 Rotor Instantaneous Pressure Distributions, 15% Gap,
 $(C_x/U) = 0.78$

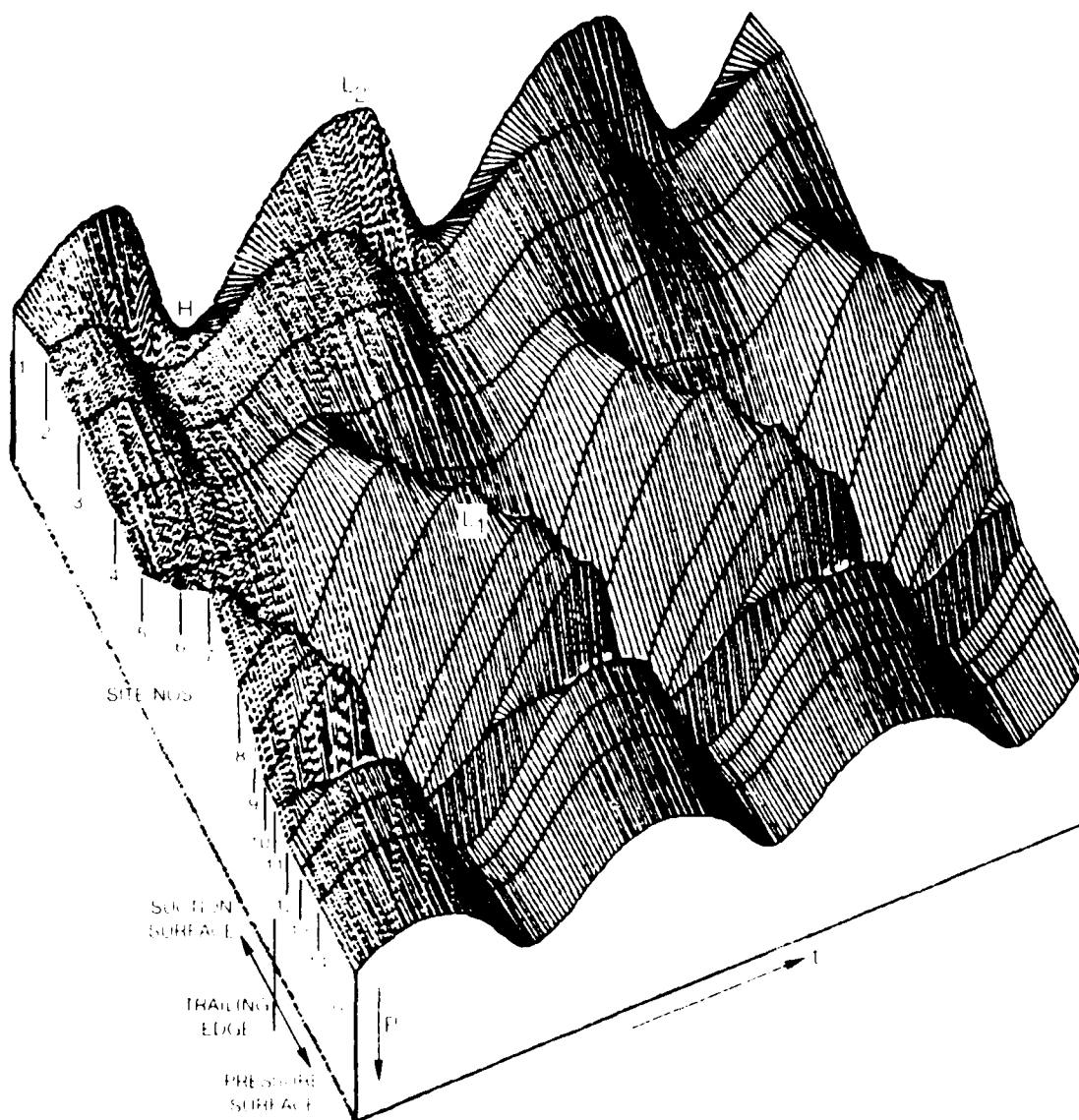


Fig. 15 Stator Pressure Time History, 15% Gap, $(C_x/U) \approx 0.78$

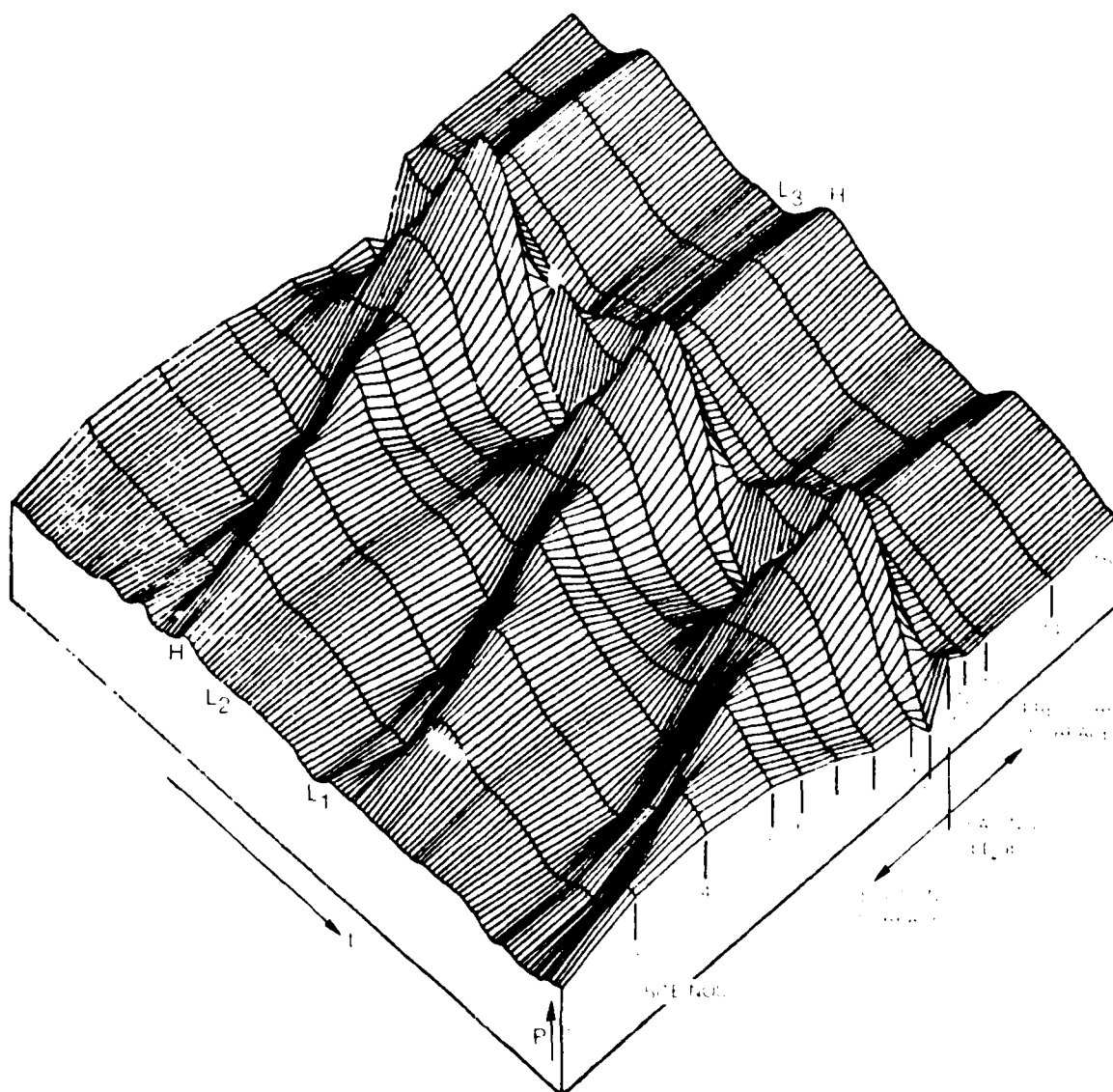


Fig. 16 Rotor Pressure Time History, 15% Gap, $(C_x/U) = 0.78$

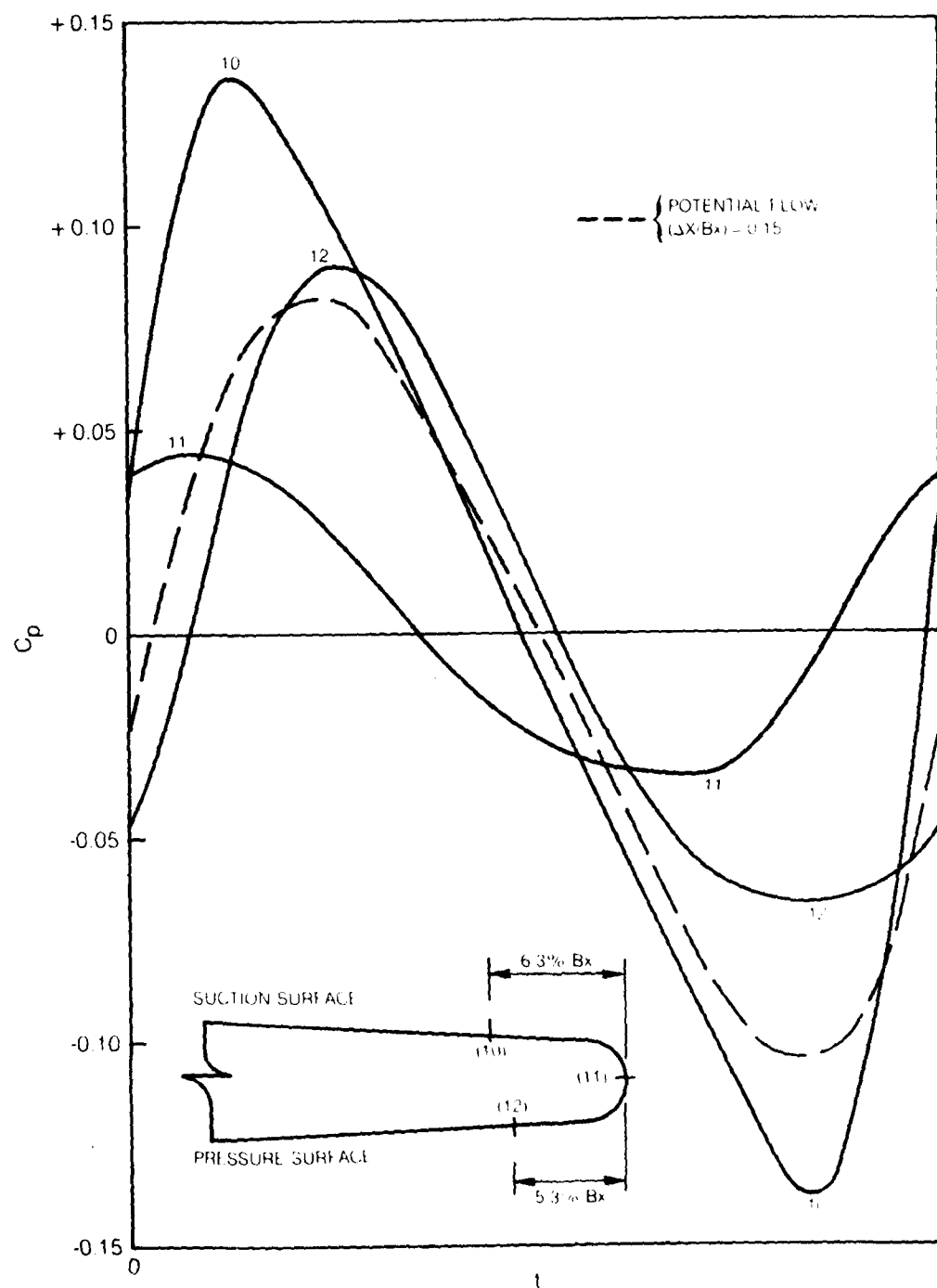


FIG. 17 Stator Trailing Edge Unsteady Pressure, 15% Gap,
 $(C_x/U) = 0.78$

81-4-88-17

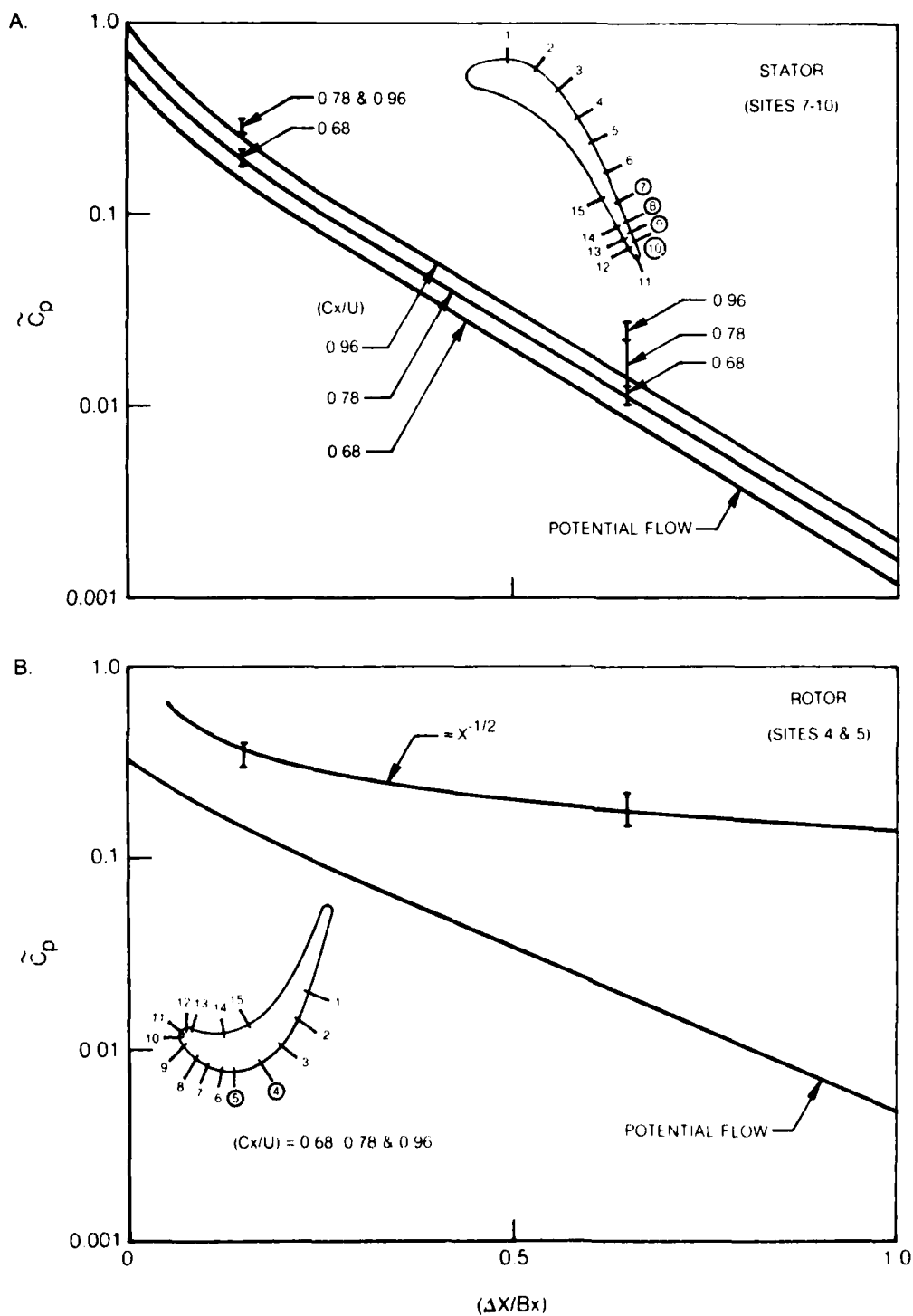


Fig. 13 Decay of Unsteady Pressure Amplitude with Axial Gap

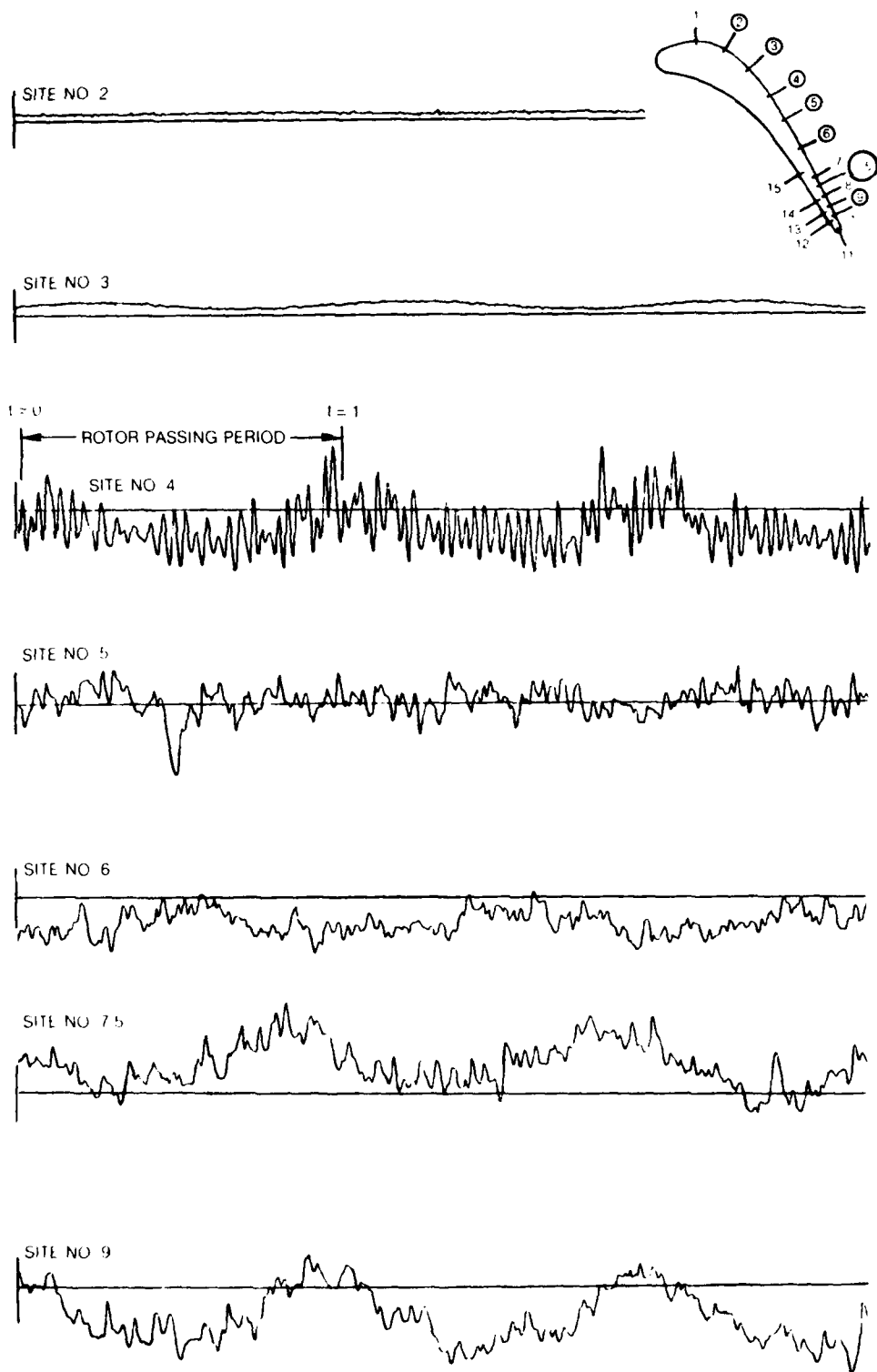
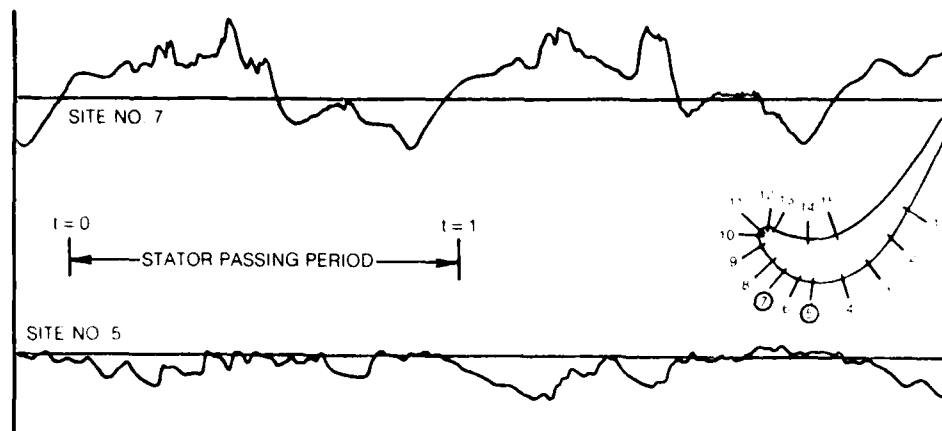


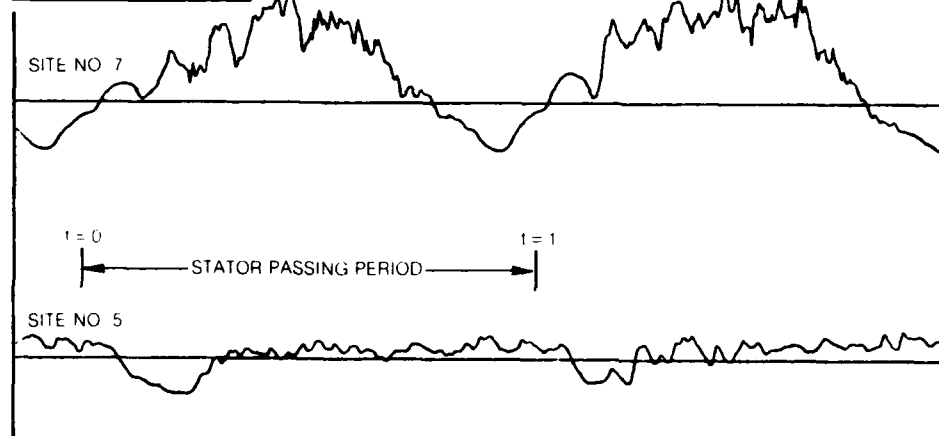
Fig. 19 Stator Thin Film Data, 15% Gap, $(C_x/U) = 0.78$

81-4-88-19

$(C_x/U) = 0.68, \beta_1 = 45^\circ$



$(C_x/U) = 0.78, \beta_1 = 40^\circ$



$(C_x/U) = 0.96, \beta_1 = 35^\circ$

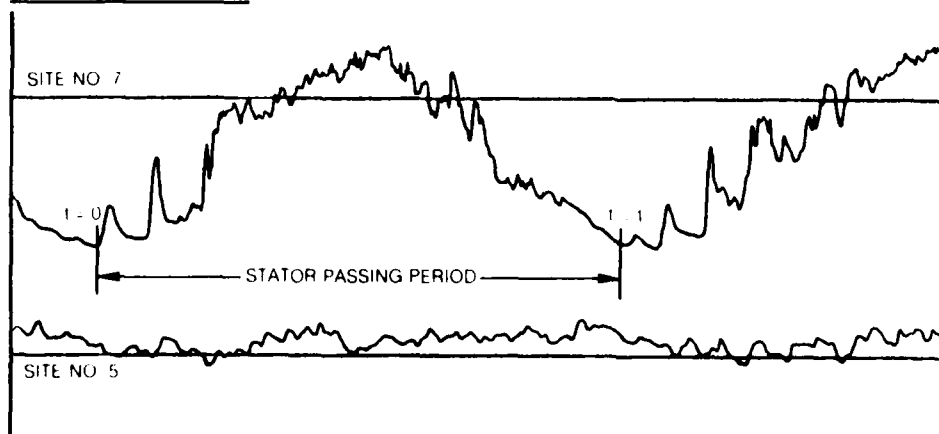
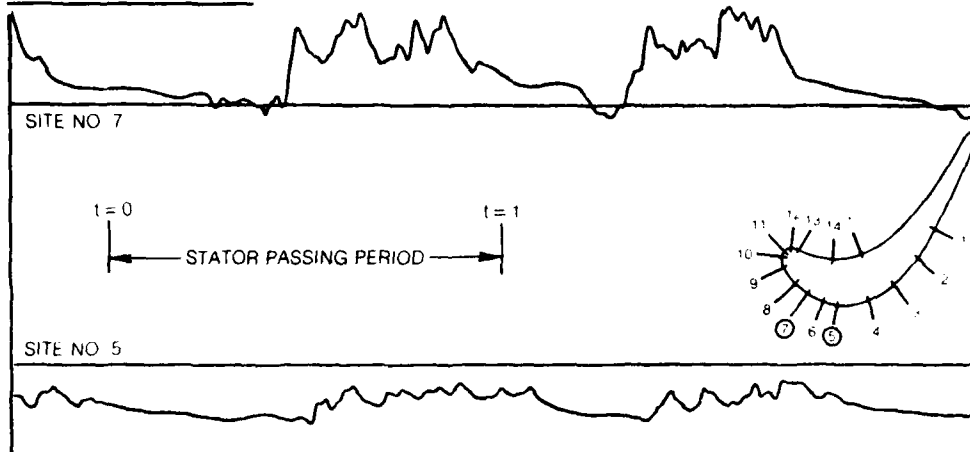


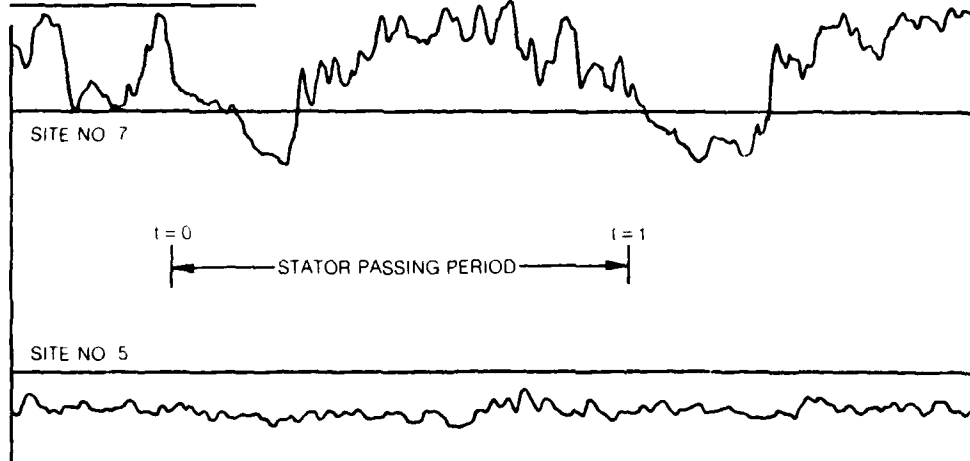
Fig. 20 Rotor Thin Film Data, 15% Gap

81-4-88-20

$(C_x/U) = 0.68, \beta_1 = 45^\circ$



$(C_x/U) = 0.78, \beta_1 = 40^\circ$



$(C_x/U) = 0.96, \beta_1 = 35^\circ$

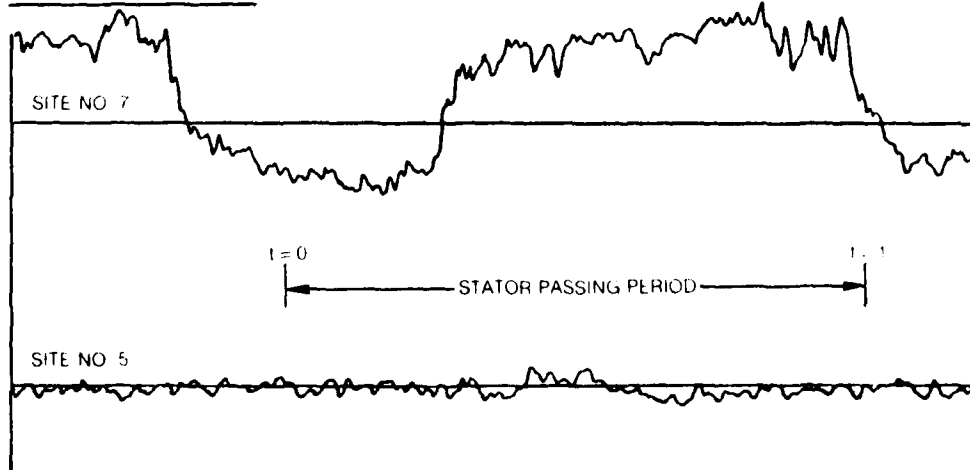


Fig. 21 Rotor Thin Film Data, 65% Gap

81-4-88-21

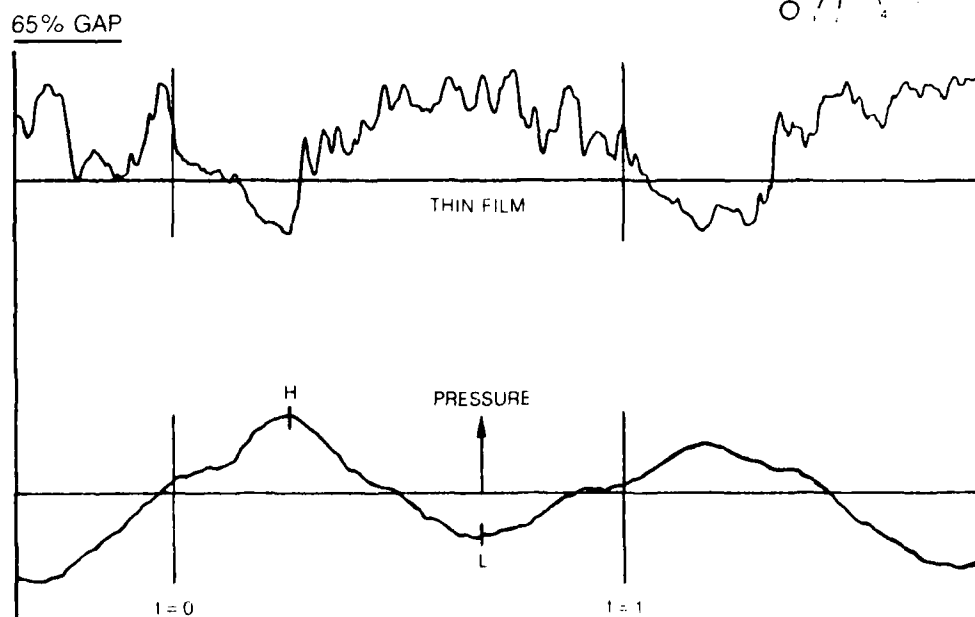
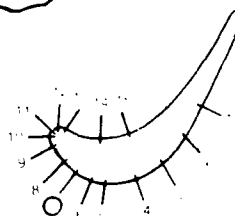
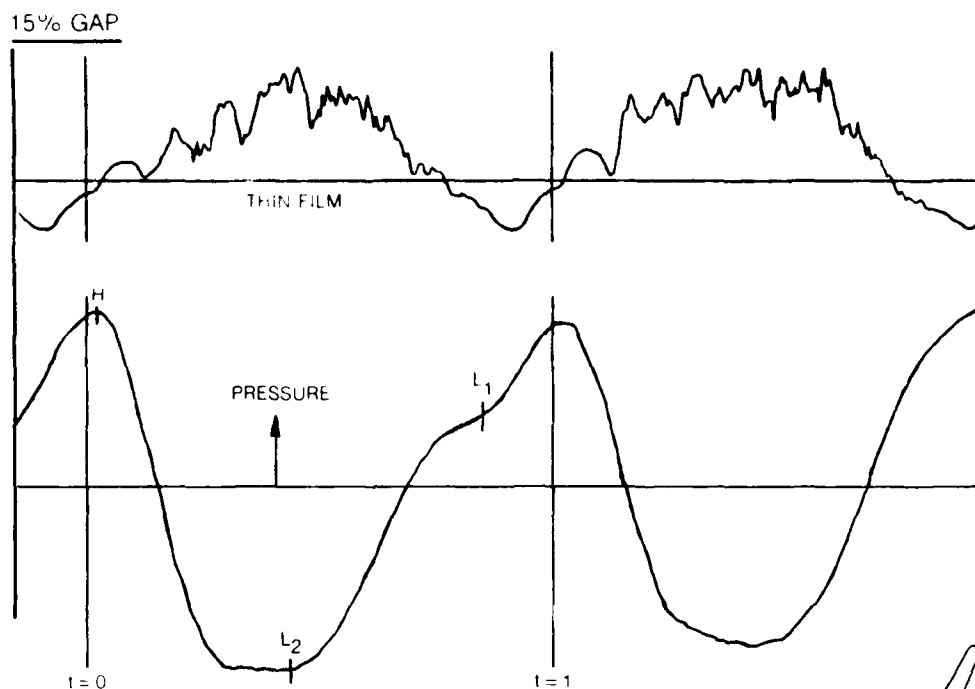


Fig. 22 Rotor Pressure and Thin Film Data at Site 7, $(C_x/U) = 0.78$

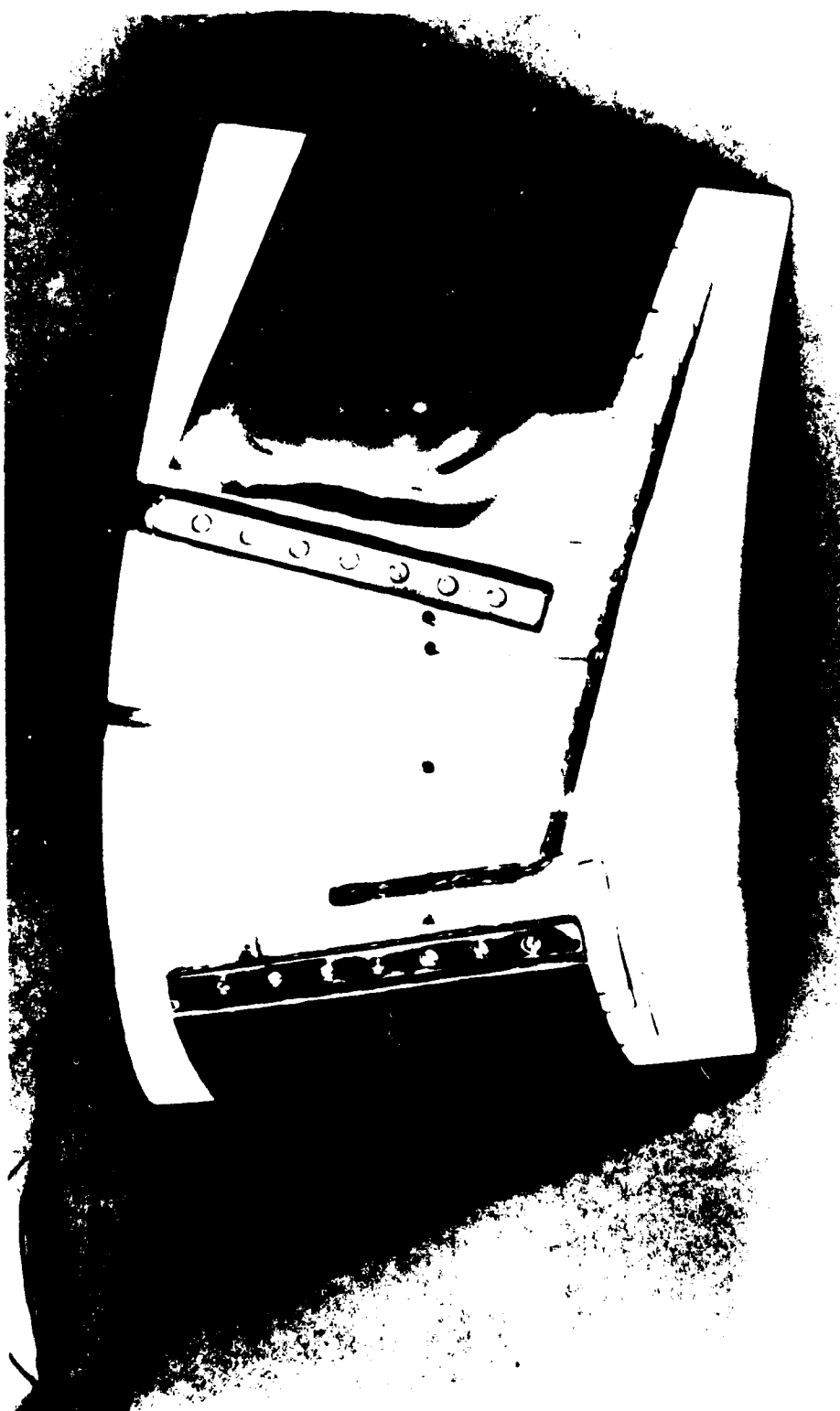


Fig. 2.3. Greater Pressure Sensor Head Tri-Order

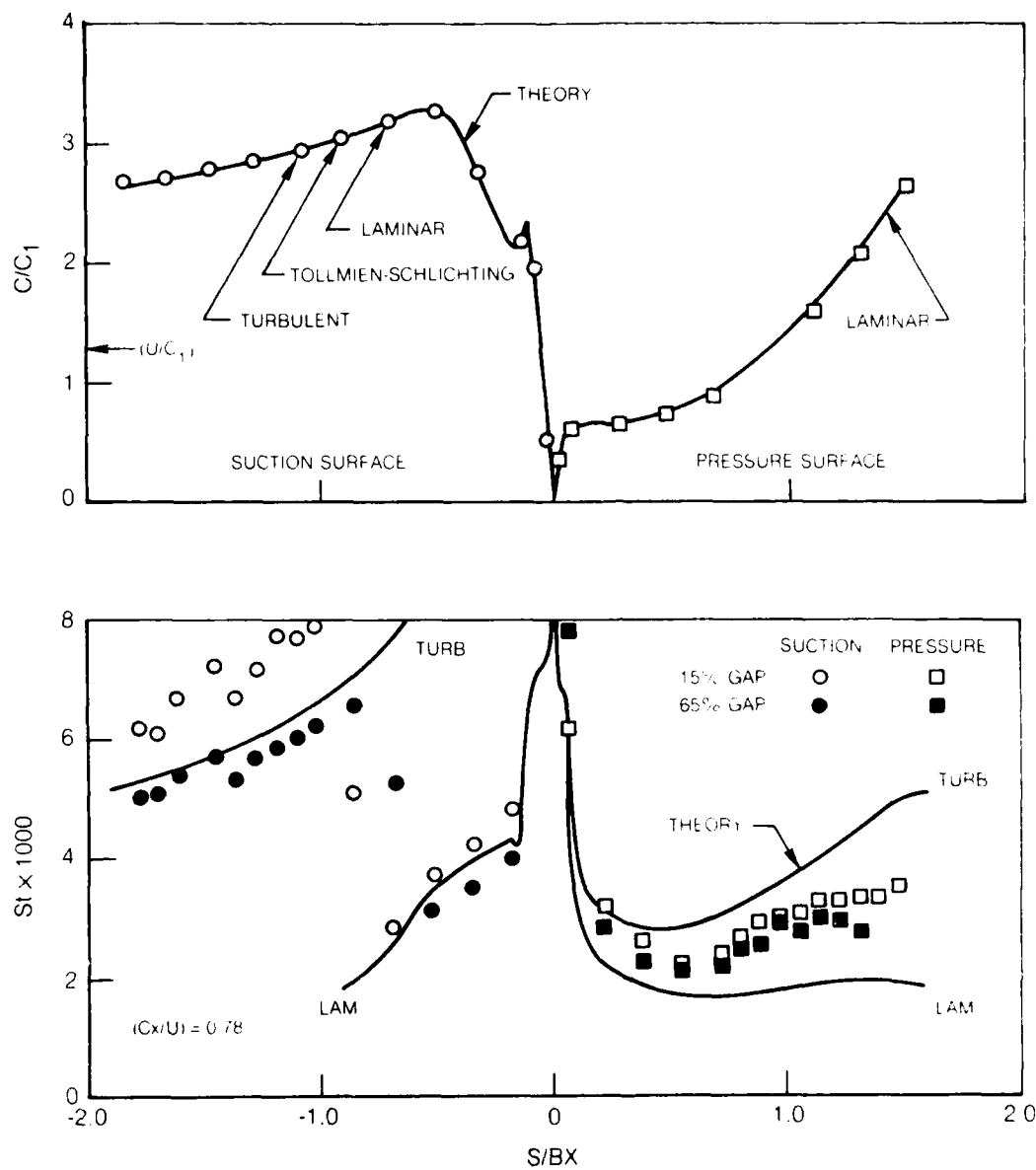


Fig. 24 Stator Velocity and Stanton Number Distributions,
 $(C_x/U) = 0.78$

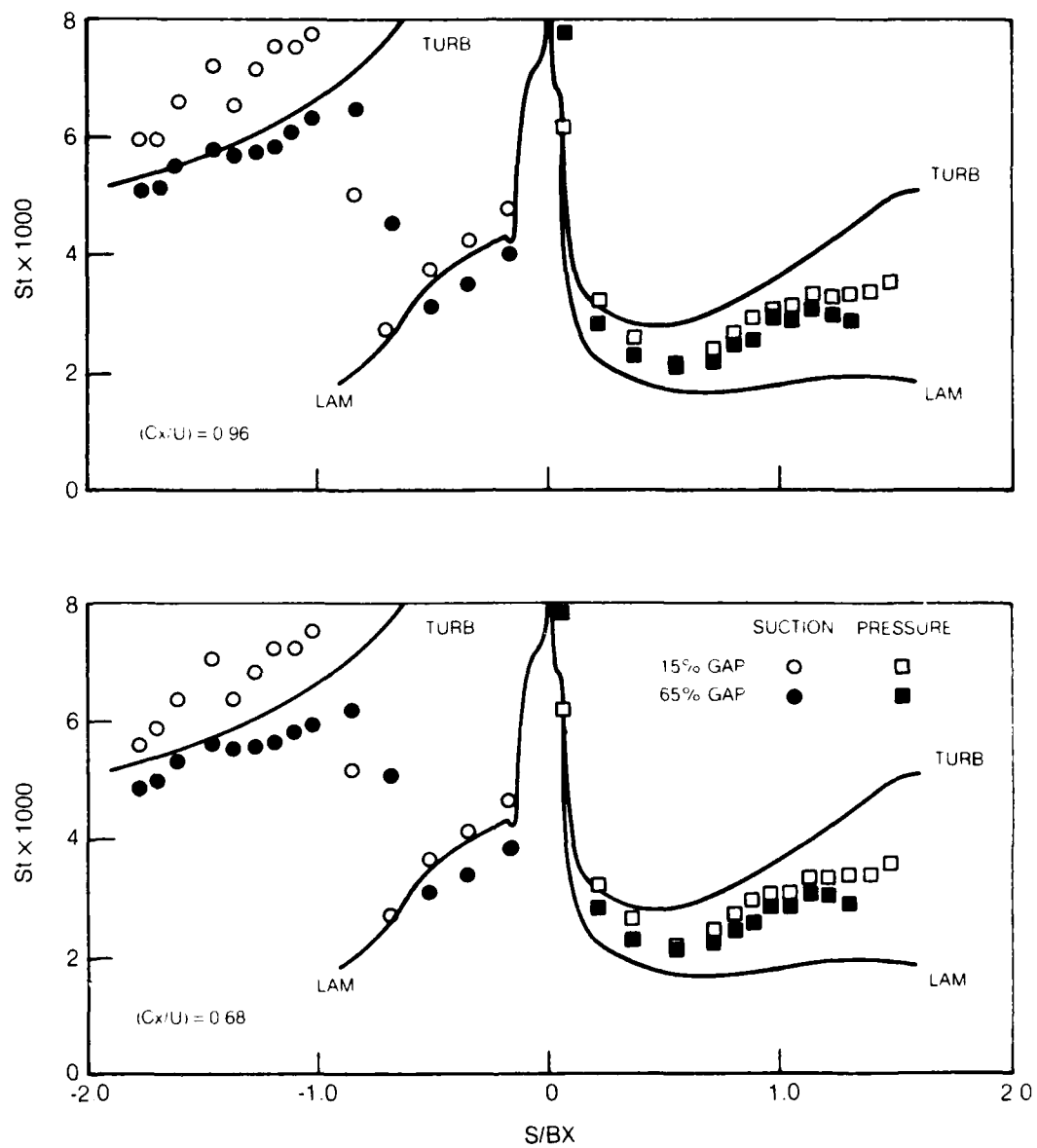


Fig. 25 Stator Stanton Number Distributions, $(C_x/U) = 0.96$ and 0.68

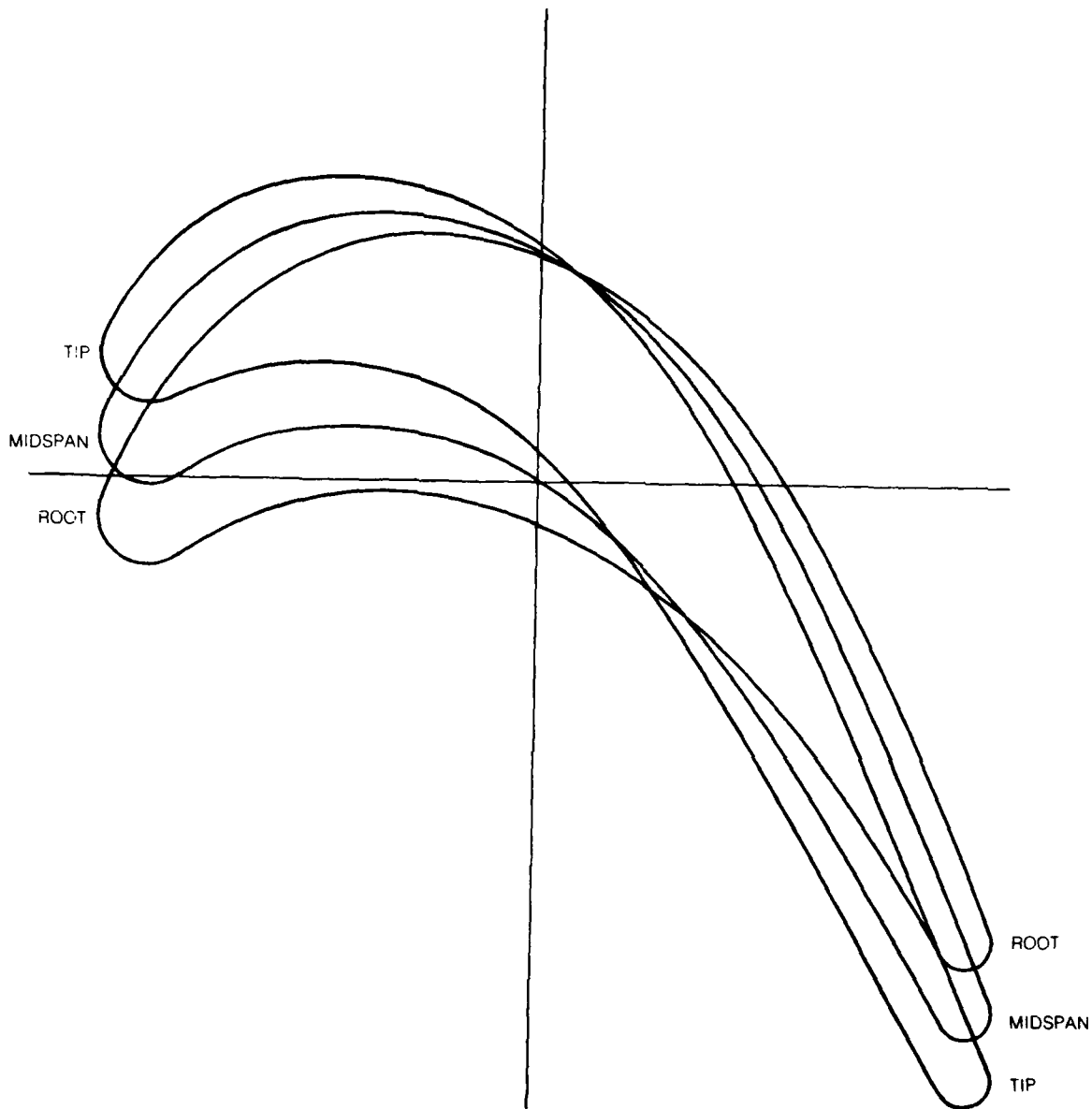


Fig. 26 Rotor Geometry

81-4-88-26

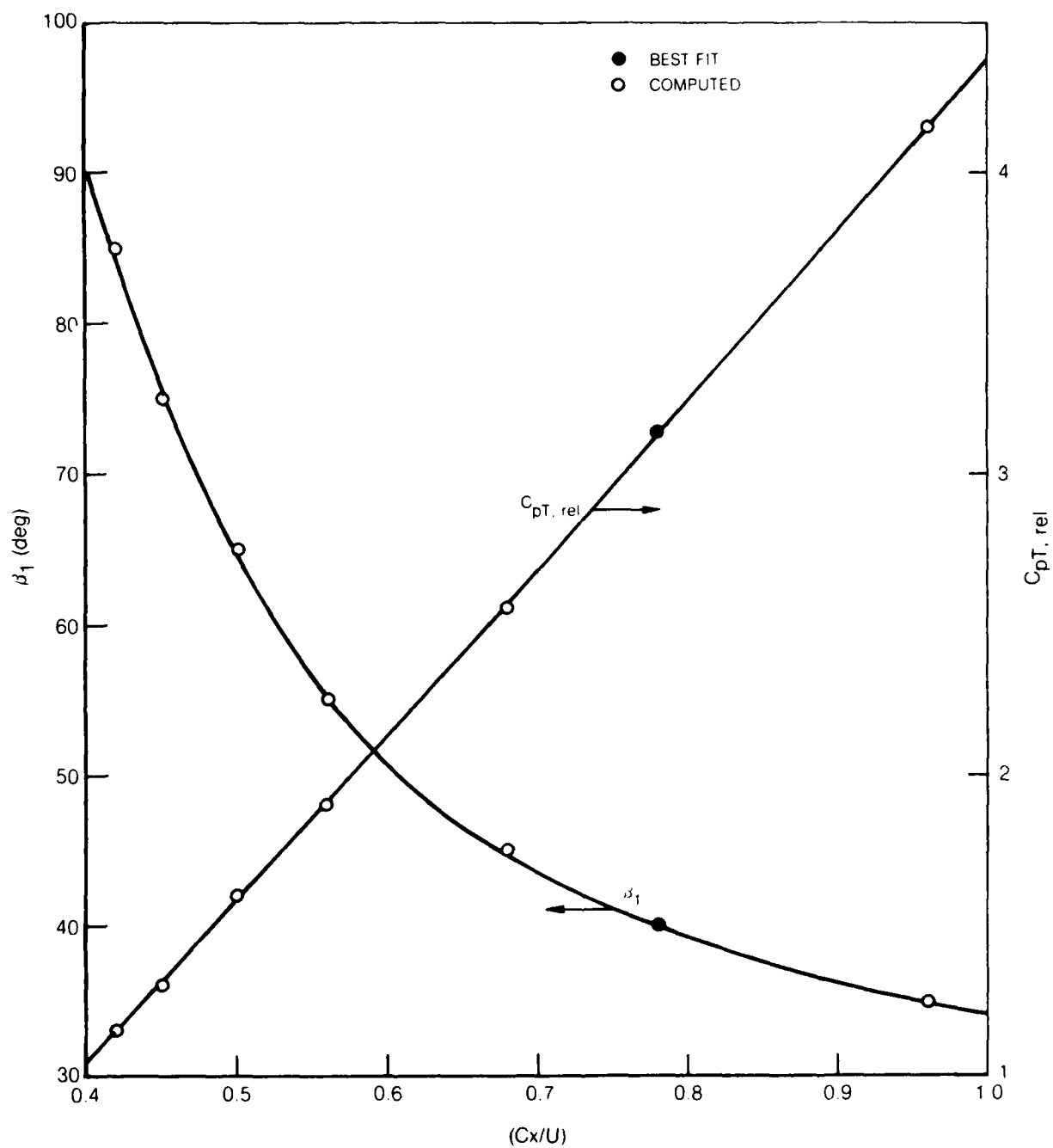
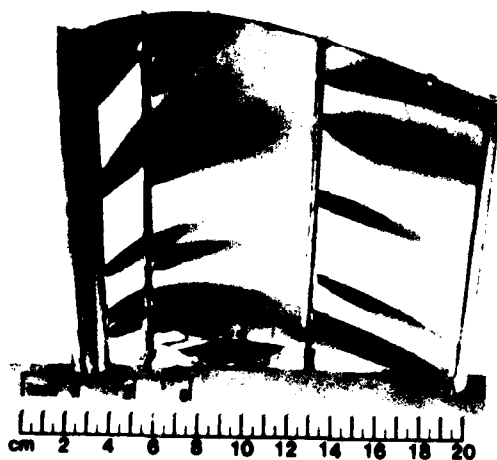
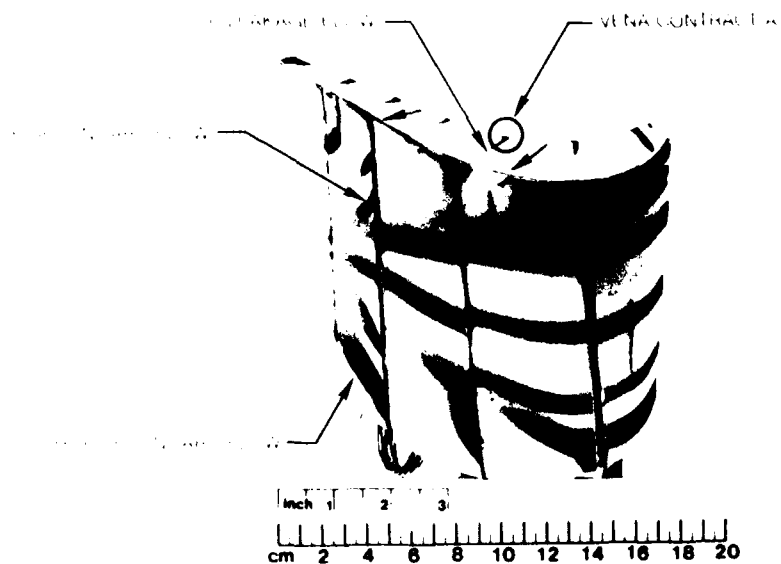


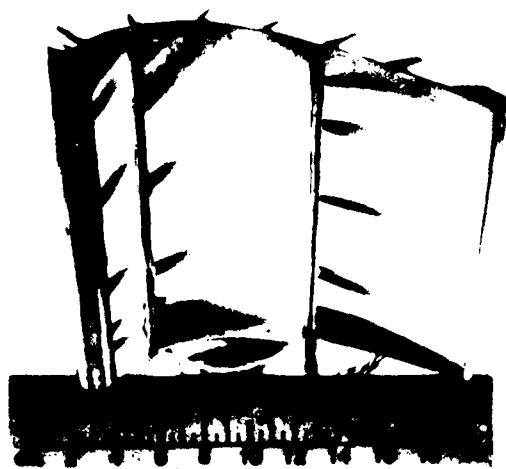
Fig. 27 Rotor Midspan Inlet Flow Angle and Relative Total Pressure Coefficient Variation with (C_x/U)

81-4-88-27



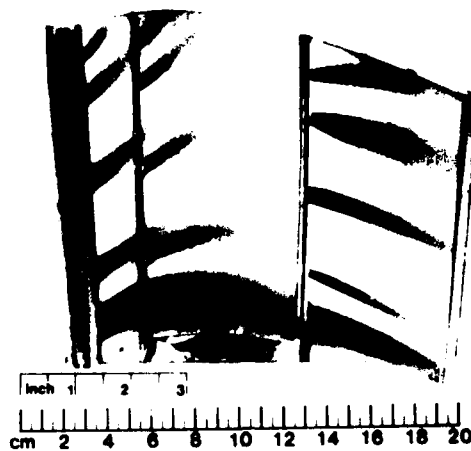


a) SUCTION SURFACE AND TIP



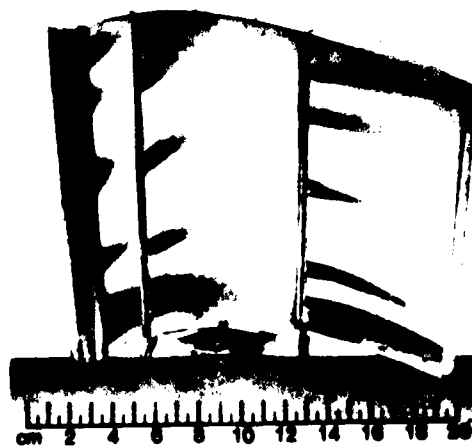
b) Pressure Surface and Root

Fig. 10. Velocity, pressure, and suction surfaces. Flow VI = 1.1 m/s, $\alpha = 0^\circ$, $Re = 0.78 \times 10^5$, $z = 40^\circ$



After Prevertebral Artery is ligated, the following is observed:

β = 100%



After Prevertebral Artery is ligated, the following is observed:

β = 100%

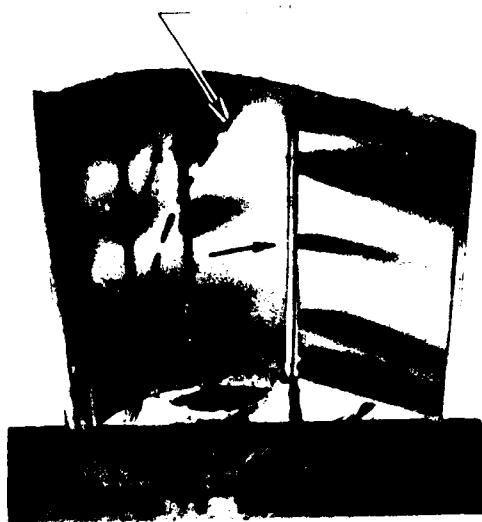


Fig. 1. The object of the experiment. The object is a curved, segmented object, possibly a book cover or a piece of machinery. The object is divided into several vertical segments. A small, dark, rectangular object is visible on the left side. A thin, light-colored line or wire runs vertically through the center of the object. The background is dark and indistinct.

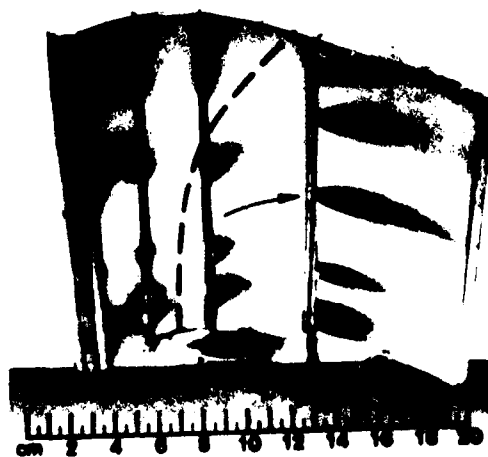


Fig. 2. The object of the experiment. The object is a curved, segmented object, possibly a book cover or a piece of machinery. The object is divided into several vertical segments. A small, dark, rectangular object is visible on the left side. A thin, light-colored line or wire runs vertically through the center of the object. The background is dark and indistinct.

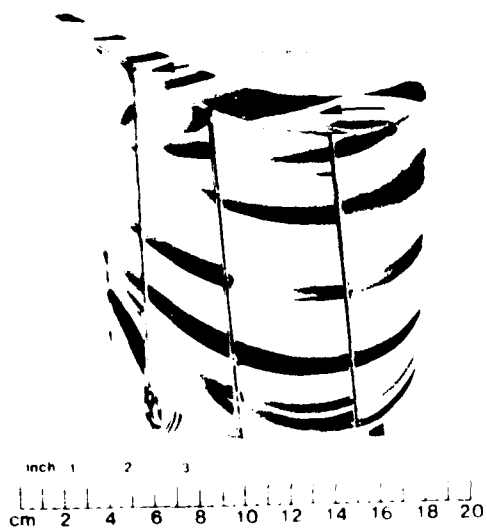


FIGURE 1. SURFACE AREA

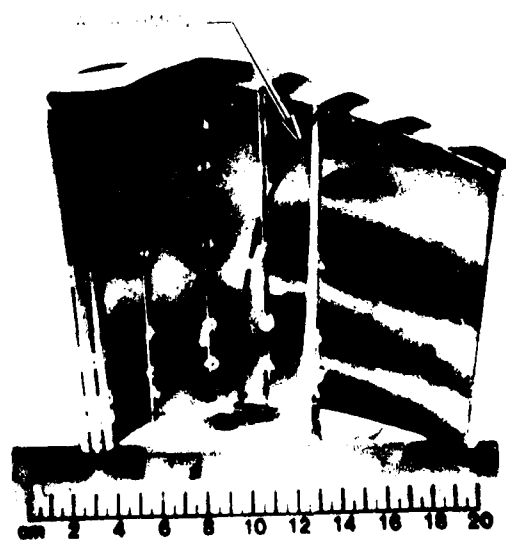


FIGURE 2. SURFACE AREA

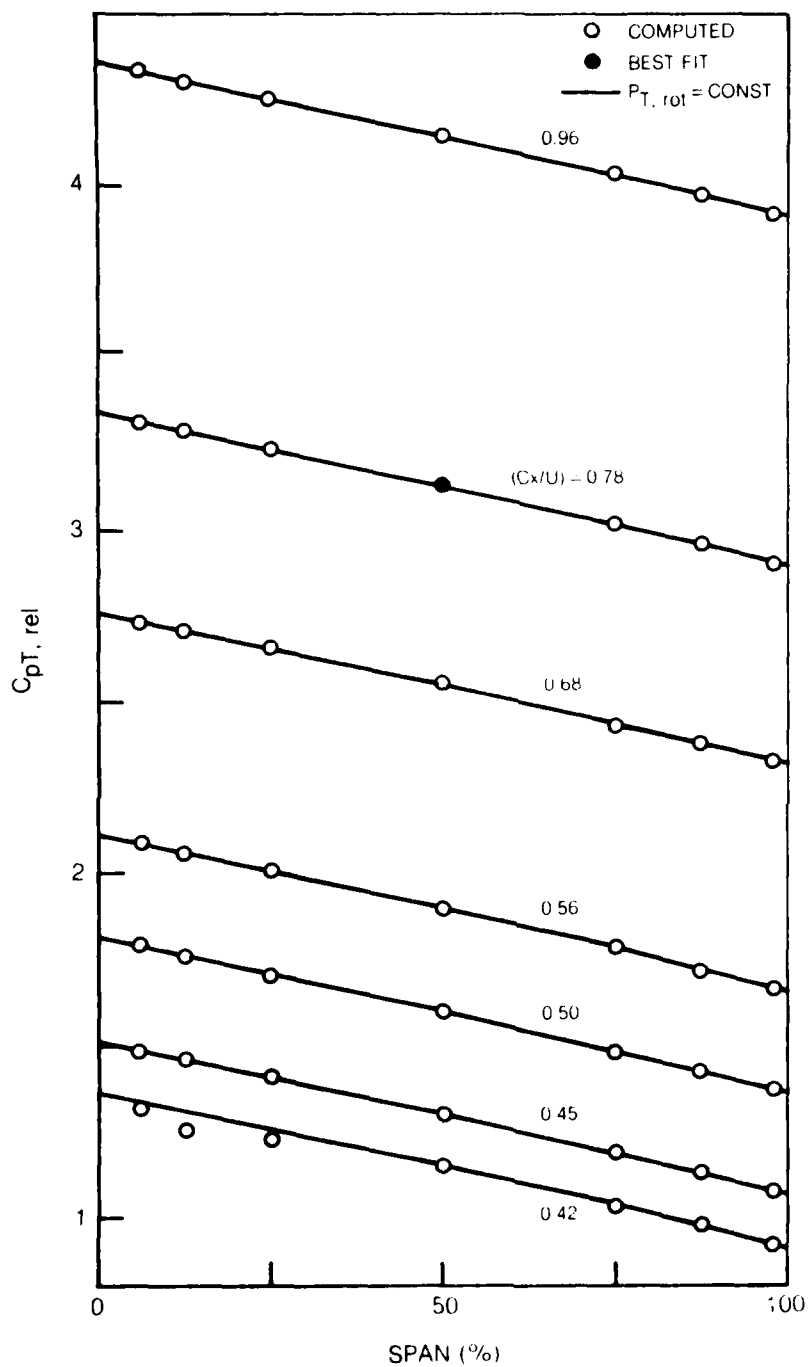


Fig. 35 Rotor Spanwise Variation of Relative Total Pressure

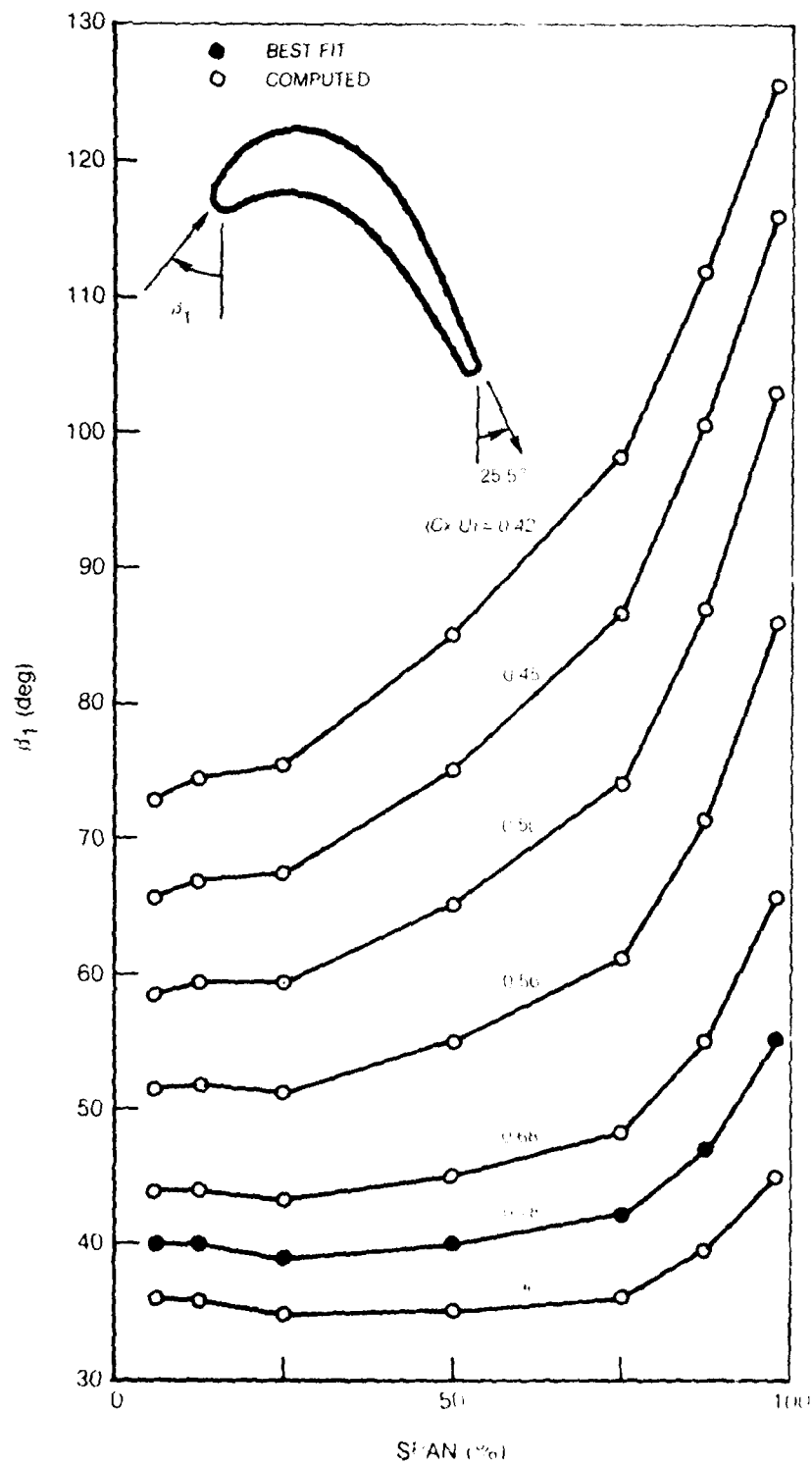


Fig. 30 Rotor Spanwise Variation of Relative Inlet Flow Angle

81 4 88 34

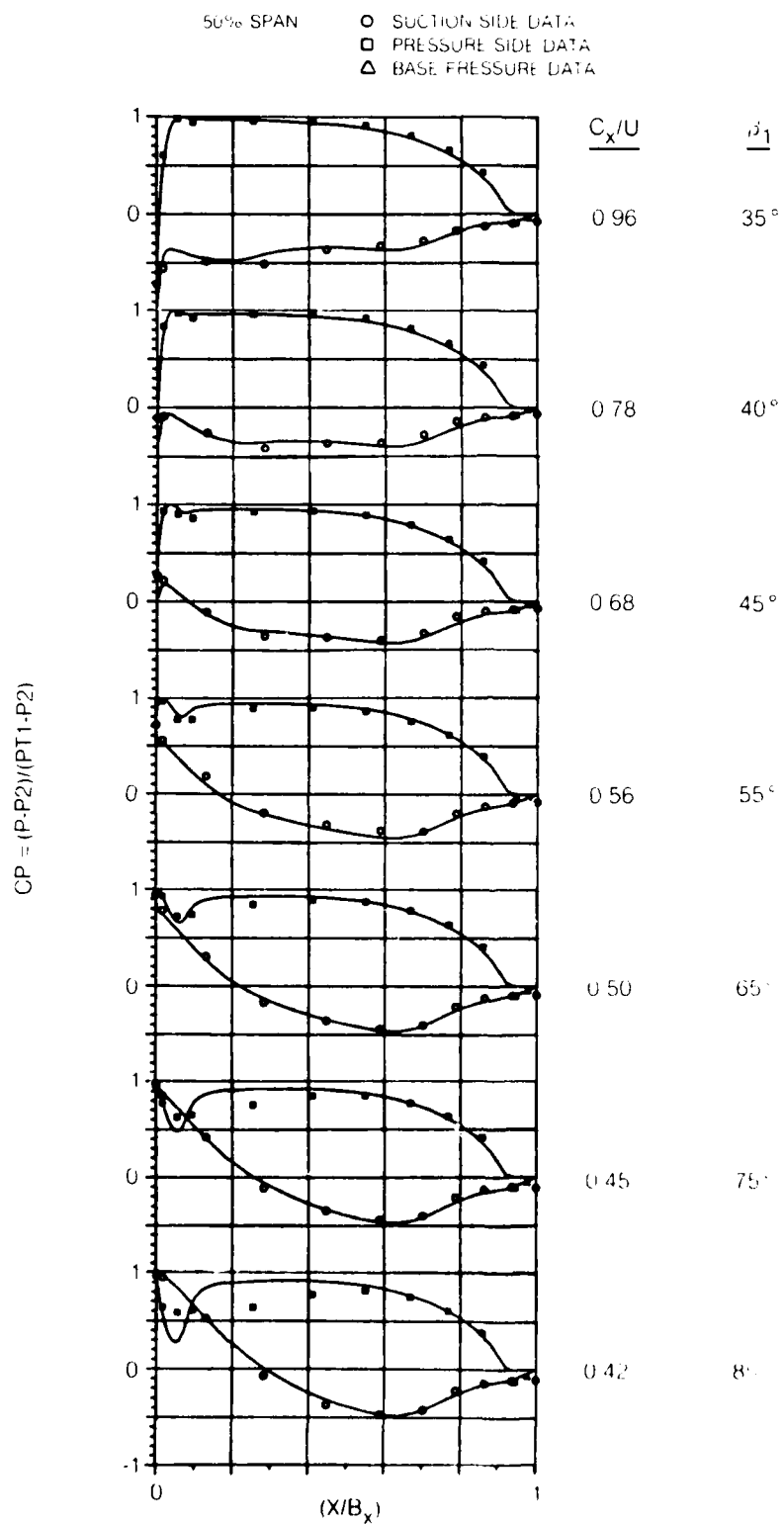


Fig. 7 Rotor Midspan Pressure Distributions, $\beta_1 = 35^\circ$ to 85°

81 3 37 8

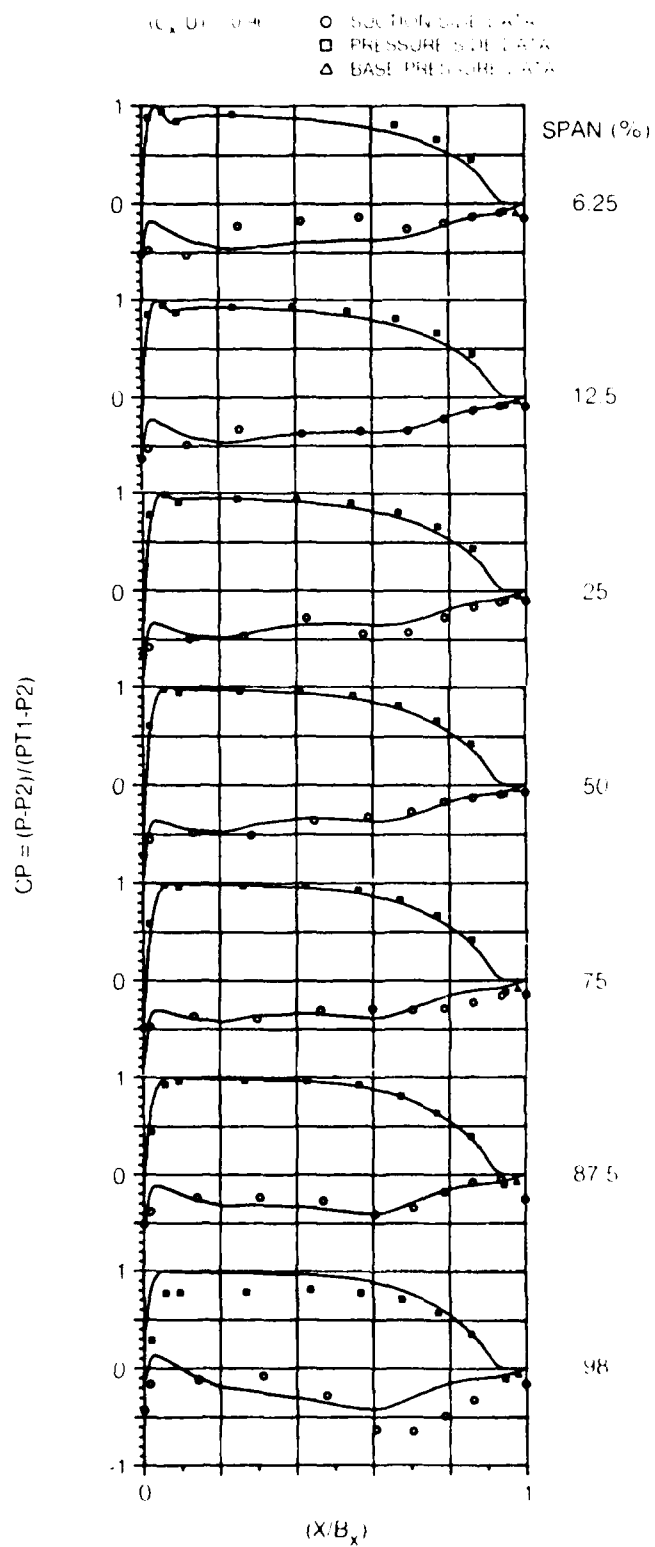


Fig. 38 Rotor Fullspan Pressure Distributions, $(C_x/U) = 0.4$

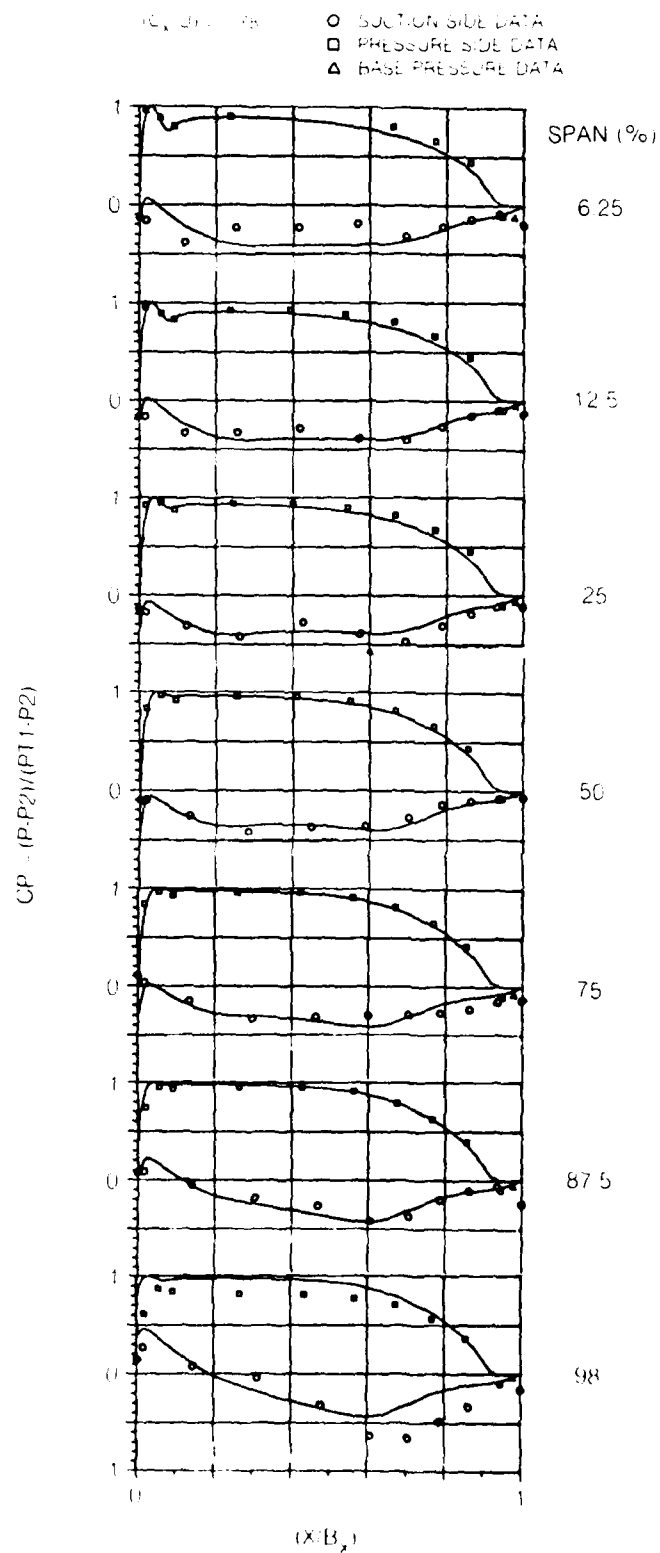


Fig. 59 Rotor Fullspan Pressure Distributions, $(C_x/U) = 0.78$

81 3 22 2

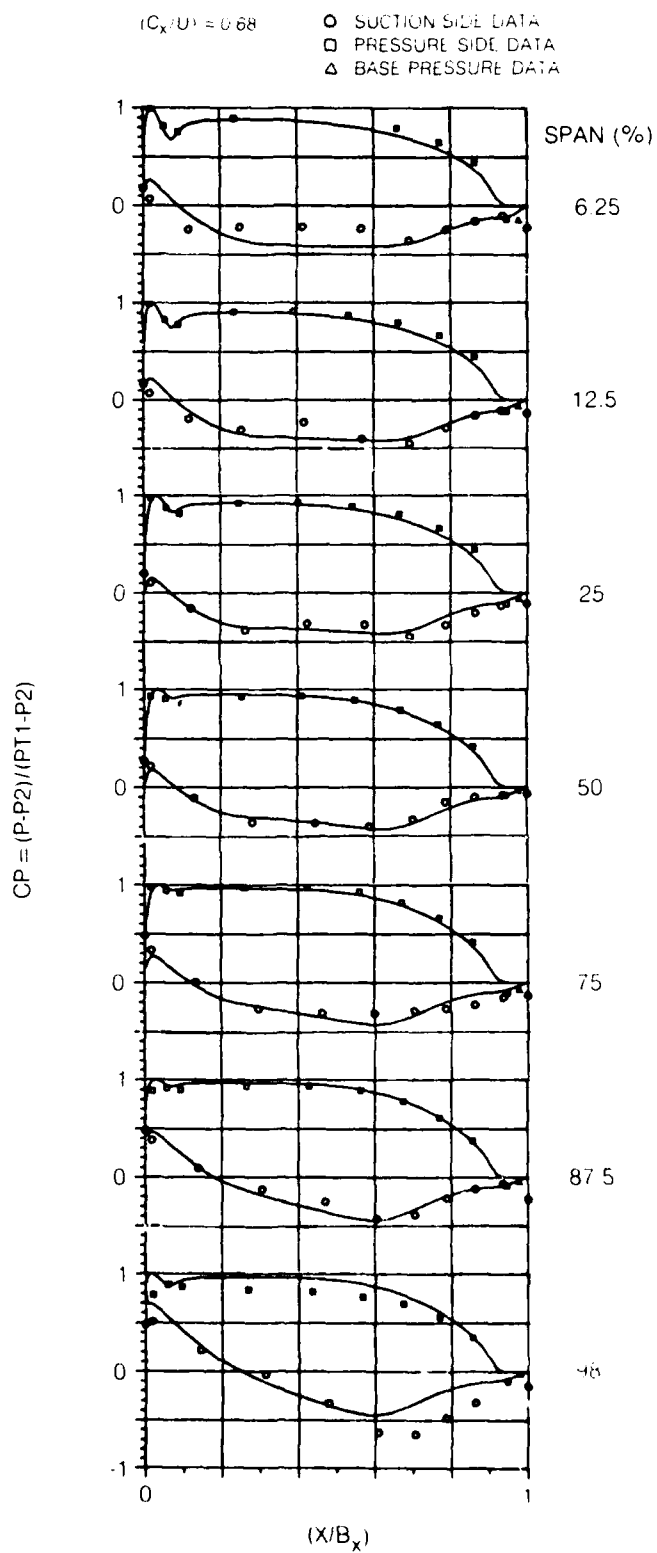


Fig. 40 Rotor Fullspan Pressure Distributions, $(C_x/U) = 0.68$